

University of Kentucky

UKnowledge

Theses and Dissertations--Mechanical
Engineering

Mechanical Engineering


2023

Utilization of Uncrewed Aircraft Systems Towards Investigating the Structure of the Atmospheric Surface Layer

Loiy Al-Ghussain

University of Kentucky, loiy.al-ghussain@uky.edu

Author ORCID Identifier:

 <https://orcid.org/0000-0002-3457-3806>

Digital Object Identifier: <https://doi.org/10.13023/etd.2023.048>

[Right click to open a feedback form in a new tab to let us know how this document benefits you.](#)

Recommended Citation

Al-Ghussain, Loiy, "Utilization of Uncrewed Aircraft Systems Towards Investigating the Structure of the Atmospheric Surface Layer" (2023). *Theses and Dissertations--Mechanical Engineering*. 209.
https://uknowledge.uky.edu/me_etds/209

This Doctoral Dissertation is brought to you for free and open access by the Mechanical Engineering at UKnowledge. It has been accepted for inclusion in Theses and Dissertations--Mechanical Engineering by an authorized administrator of UKnowledge. For more information, please contact UKnowledge@lsv.uky.edu.

STUDENT AGREEMENT:

I represent that my thesis or dissertation and abstract are my original work. Proper attribution has been given to all outside sources. I understand that I am solely responsible for obtaining any needed copyright permissions. I have obtained needed written permission statement(s) from the owner(s) of each third-party copyrighted matter to be included in my work, allowing electronic distribution (if such use is not permitted by the fair use doctrine) which will be submitted to UKnowledge as Additional File.

I hereby grant to The University of Kentucky and its agents the irrevocable, non-exclusive, and royalty-free license to archive and make accessible my work in whole or in part in all forms of media, now or hereafter known. I agree that the document mentioned above may be made available immediately for worldwide access unless an embargo applies.

I retain all other ownership rights to the copyright of my work. I also retain the right to use in future works (such as articles or books) all or part of my work. I understand that I am free to register the copyright to my work.

REVIEW, APPROVAL AND ACCEPTANCE

The document mentioned above has been reviewed and accepted by the student's advisor, on behalf of the advisory committee, and by the Director of Graduate Studies (DGS), on behalf of the program; we verify that this is the final, approved version of the student's thesis including all changes required by the advisory committee. The undersigned agree to abide by the statements above.

Loiy Al-Ghussain, Student

Sean C.C. Bailey, Major Professor

Jesse B. Hoagg, Director of Graduate Studies

Utilization of Uncrewed Aircraft Systems Towards Investigating the Structure of the
Atmospheric Surface Layer

DISSERTATION

A dissertation submitted in partial
fulfillment of the requirements for
the degree of Doctor of Philosophy
in the College of Engineering at the

University of Kentucky

By

Loiy Al-Ghussain

Lexington, Kentucky

Director: Dr. Sean C.C. Bailey, Professor of Mechanical and Aerospace Engineering

Lexington, Kentucky

2023

Copyright© Loiy Al-Ghussain 2023

ABSTRACT OF DISSERTATION

Utilization of Uncrewed Aircraft Systems Towards Investigating the Structure of the Atmospheric Surface Layer

This study presents two approaches to investigate the surface-layer structure during the morning transition using uncrewed aircraft systems. The first approach employs three uncrewed aircraft systems- each equipped with a single multi-hole probe- simultaneously measuring horizontal transects were partnered with a fourth measuring vertical profiles during two consecutive mornings as part of the 2017 Collaboration Leading Operational Unmanned Aerial System Development for Meteorology and Atmospheric Physics (CLOUDMAP) measurement campaign near Stillwater, Oklahoma, U.S.A. Data were analyzed to extract time-dependent single-point statistics of kinematic and thermodynamic variables from the uncrewed aircraft systems. In addition, an approach is presented by which multi-point spatial statistics in the form of auto- and cross-correlations could be calculated from the measurements.

The second approach employs two fixed-wing uncrewed aircraft systems simultaneously flying horizontal transects with a third rotorcraft uncrewed aircraft system for vertical profiling during a limited deployment at the University of Kentucky North Research Farm (UKNRF), Lexington, U.S.A. The first fixed-wing aircraft is equipped with a custom-built multi-hole-probe-based vorticity probe. The configuration of the vorticity probe allows the estimation of the velocity and small-scale velocity gradients. These gradients are employed to estimate the dissipation rate and vorticity fields which can be used for identifying and characterizing the atmospheric boundary layer structure. The second fixed-wing aircraft is equipped with a single multi-hole probe used to resolve the advection velocity of coherent structures which can be used to approximate the streamwise spatial flow field using frozen Taylor's hypothesis.

The results from the first approach during CLOUDMAP campaign reflect differences in the evolution of spatial statistics with altitude for each of the two days at scales smaller than 500 m, despite very similar synoptic conditions. Conditional averaging was also applied to identify the structure of sweep and ejection motions and results revealed similarities to observations from canonical wall-bounded flow. Whereas, the results from the UKNRF campaign reveal the ability of the vorticity

probe to estimate the dissipation rate flow field even though the spatial separation between the probes is much larger than Kolmogorov length scale. The mean dissipation rate estimated from the vorticity probe showed good agreement with the dissipation rate estimated based on Kolmogorov theory from the streamwise power spectrum. Additionally, the instantaneous dissipation rate flow field had signatures, represented by intermittent intense regions, associated with coherent structures which align with similar signatures in the flow fields of the vorticity and virtual temperature fluctuations. The observed structures have spatial length scales in the order of 200 m. Additionally, the spatial extent of the detected coherent structures, as well as the results from the conditional averaging of sweep and ejection events, imply that these regions could correspond to either low-momentum streaks, that evolve to form the legs of hairpin vortices, or the hairpin vortices legs. Finally, the observed average flow structure of different atmospheric quantities during the three flights has characteristics associated with coherent structures similar to what was observed previously in the atmospheric surface layer and in canonical wall-bounded flows.

KEYWORDS: Coherent structures; Planetary Boundary Layer; Uncrewed Aircraft Systems; Atmosphere; Turbulence; Atmospheric Stability

Loiy Al-Ghussain

April 4, 2023

Utilization of Uncrewed Aircraft Systems Towards Investigating the Structure of the
Atmospheric Surface Layer

By

Loiy Al-Ghussain

Dr. Sean C.C. Bailey

Director of Dissertation

Dr. Jesse B. Hoagg

Director of Graduate Studies

April 4, 2023

Date

I dedicate this Ph.D. dissertation to my wife, who has been my constant source of support and encouragement throughout this journey. Your unwavering faith in me has given me the strength to persevere and overcome the obstacles that I have encountered. Thank you for always being there for me and for being my rock.

I also dedicate this work to my mother, who has always been there for me with her love, guidance, and prayers. Your support has been invaluable and has played a crucial role in my success.

Finally, I dedicate this dissertation to my father, who passed away before he could see me reach this milestone. I know he would have been proud of me and I will always cherish the memories of the time we spent together. His love and spirit live on through me and I hope that I have made him proud.

ACKNOWLEDGMENTS

I would like to take this opportunity to extend my sincerest gratitude to those who have supported me throughout my Ph.D. journey. To begin with, as a Muslim and a strong believer, I thank Allah who has guided me, facilitated this journey, taught me from his endless knowledge, and answered my prayers to achieve this milestone. I am deeply thankful to my wife for her unwavering support and encouragement during this journey. I also extend my gratitude to my mother and mother-in-law for their continuous prayers and support. I would like also to extend my deepest gratitude to my mosque companion, Ahmed Alhudhud, who has never forgotten me in his prayers despite my absence.

Special thanks go to my friends Adnan Dawrish Ahmed, Hammoudeh Alfar, Ahmed AbuBaker, Mohammed Khalil, and Neng Huang, who have been with me through thick and thin and have provided me with their unwavering support and encouragement.

I am also eternally grateful to my supervisor and mentor, Prof. Sean Bailey, who has been an immense source of guidance and support throughout my Ph.D. journey. Prof. Bailey has been incredibly patient, helpful, and insightful in his approach, guiding me through each step of the way. His wisdom, guidance, and unwavering support have been invaluable to me and have greatly contributed to the successful completion of this dissertation. Additionally, I would like to thank the UAV lab members, especially Ryan Nolin, Christina Vezzi, and Alex Hodge, for their support and operation of the flight campaigns. Finally, I would also like to gratefully acknowledge the US National Science Foundation for their support for this work through Award No. CNS-1932105.

TABLE OF CONTENTS

Acknowledgments	iii
List of Tables	vii
List of Figures	viii
Chapter 1 Introduction	1
Chapter 2 Background and Literature Review	7
2.1 Atmospheric Stability	7
2.2 Atmospheric Surface-Layer Structure	8
2.3 Uncrewed Aircraft Systems in Atmospheric Research	12
2.4 Atmospheric Wind Measurements	15
2.5 Dissipation Rate Measurements in the Atmospheric Boundary Layer	18
2.6 Vorticity Measurement in the Atmospheric Boundary Layer	22
Chapter 3 Motivation and Objectives	26
Chapter 4 The Multi-hole Probe Measurement Approach	28
Chapter 5 Approach for Minimizing Aircraft Motion Bias in Multi-Hole Probe Wind Measurements	32
5.1 Correction Procedure	32
5.1.1 Correction Procedure: Version 1	32

5.2	Multi-Hole Probe Measurements Correction	36
5.2.1	Comparison to ground reference	37
5.2.2	Implementation in profiling measurements: Version 1	42
5.3	Correction Procedure: Version 2	47
5.3.1	Implementation and validation Version 2	48
5.4	Summary	51
Chapter 6	Coherent Structures Observation From Single Multi-Hole Probe Measurements	53
6.1	CLOUDMAP Campaign	53
6.2	Stability Conditions	57
6.3	Mean Properties of the Surface Layer	59
6.4	Visualization of Flow Structure	63
6.5	Temperature and Velocity Correlations	68
6.6	Coherent Structure Associated with Sweep and Ejection Events	78
6.7	Summary	87
Chapter 7	Coherent Structure Characterization using an Uncrewed Aircraft System Equipped with a Vorticity Probe	89
7.1	Overview of Vorticity Probe	89
7.2	Overview Calibration Setup	94
7.3	UKNRF Flight Campaign	96
7.4	Mean Background Properties of the Boundary Layer	100
7.5	Spatial Observations of Flow Structure	103

7.6 Average Flow Structure Visualization	107
Chapter 8 Conclusions and Future Work	116
8.1 Future Work	120
Bibliography	122
Vita	145

LIST OF TABLES

1.1	Strengths and weaknesses of different measurement approaches utilized in atmospheric research (Bonin et al., 2012; de Boer et al., 2022).	3
5.1	Components of $\Delta\epsilon$ determined by optimization for each UAS for both flights.	46
5.2	Components of $\Delta\epsilon$ and the corrections coefficients of the flow angles determined by optimization.	51

LIST OF FIGURES

5.1	Comparison between uncorrected (a) horizontal wind speed and (b) wind direction measured by UASs to the reference signal measured by MURC. Gray lines indicate full signal from UASs, whereas black lines indicate same signal downsampled to same data rate as that of the MURC by plotting every 200 th data point. From (Al-Ghussain and Bailey, 2021) and used under the Creative Commons Attribution 4.0 License.	38
5.2	Small uncrewed aerial system-based wind measurements from Fig. 5.1 following correction compared to the reference signal measured by MURC: (a) horizontal wind speed and (b) wind direction. Gray lines indicate full signal from UASs, whereas black lines indicate same signal downsampled to same data rate as that of the MURC by plotting every 200 th data point. From (Al-Ghussain and Bailey, 2021) and used under the Creative Commons Attribution 4.0 License.	39
5.3	Power spectrum of horizontal wind magnitude calculated from uncorrected and corrected time series. From (Al-Ghussain and Bailey, 2021) and used under the Creative Commons Attribution 4.0 License.	40
5.4	Direct comparison between (a) uncorrected and (c) corrected horizontal wind speed measured simultaneously by UASs and MURC. Similar comparison shown for (b) uncorrected and (d) corrected wind direction. Solid red line indicates line where both measurements are identical and dashed lines indicate 2 standard deviations of the difference between the UASs and MURC measured values. From (Al-Ghussain and Bailey, 2021) and used under the Creative Commons Attribution 4.0 License.	41
5.5	Comparison between measured wind direction and aircraft yaw direction for (a) uncorrected and (b) corrected signals as a function of time for a single flight. From (Al-Ghussain and Bailey, 2021) and used under the Creative Commons Attribution 4.0 License.	43
5.6	Comparison of mean (a) horizontal wind magnitude and (b) wind direction profiles measured by UAS 1 at 8:30 MDT with and without correction applied. Horizontal mean magnitude and direction profiles measured at 9:30 MDT shown in (c) and (d) respectively. From (Al-Ghussain and Bailey, 2021) and used under the Creative Commons Attribution 4.0 License.	45
5.7	Comparison of mean (a) horizontal wind speed and (b) direction profiles measured by UAS 2 at 9:10 MDT with and without correction applied. Horizontal wind speed and direction profiles measured at 10:10 MDT shown in (c) and (d) respectively. From (Al-Ghussain and Bailey, 2021) and used under the Creative Commons Attribution 4.0 License.	45
5.8	Comparison of (a) horizontal wind magnitude and (b) wind direction profiles with and without correction versions applied.	50
5.9	Comparison of wind direction and aircraft yaw direction (a) uncorrected, (b) corrected using V1, and (c) corrected using V2.	50

6.1	(a) Topographic map showing terrain surrounding measurement with (b) detailed satellite photograph of area highlighted by red box in (a). (c) shows the fixed-wing and rotorcraft UAS used, along with an additional illustration of the different flight path altitudes. Approximate location of flight trajectories and of fixed-wing UAS and measurement location of the rotorcraft indicated by red line and green dot respectively in (b). Contour lines in (a) correspond to 3.048 m elevation separation. From (Al-Ghussain and Bailey, 2022) and used with permission, license number 5513720396324.	56
6.2	(a) R_i and (b) L calculated from the 7-m tower data for the duration of Case 1 and Case 2 observation periods. From (Al-Ghussain and Bailey, 2022) and used with permission, license number 5513720396324.	58
6.3	Time-dependence of: (a) $\langle \theta_v \rangle$ for Case 1; (b) $\langle \theta_v \rangle$ for Case 2; (c) $\langle u \rangle$ and $\langle v \rangle$ for Case 1; (d) $\langle u \rangle$ and $\langle v \rangle$ for Case 2; (e) $\langle k \rangle$ for Case 1; (f) $\langle k \rangle$ for Case 2; (g) $\langle \theta_v^2 \rangle$ for Case 1; (h) $\langle \theta_v^2 \rangle$ for Case 2; (i) $\langle P \rangle / \langle \varepsilon \rangle$ for Case 1; and (j) $\langle P \rangle / \langle \varepsilon \rangle$ for Case 2. Blue symbols indicate measurements made at $z = 25$ m, red symbols indicate measurements made at $z = 50$ m, green symbols indicate measurements made at $z = 75$ m, and orange symbols indicate measurements made at $z = 300$ m. From (Al-Ghussain and Bailey, 2022) and used with permission, license number 5513720396324.	60
6.4	Isocontours of $\theta'_v(t, z)$ measured by rotorcraft UAS for: (a) 0600 LT to 0900 LT and (b) 0900 LT to 1200 LT for Case 1 and (c) 0600 LT to 0900 LT and (d) 0900 LT to 1200 LT for Case 2. From (Al-Ghussain and Bailey, 2022) and used with permission, license number 5513720396324.	65
6.5	Isocontours of $U'(t, z)$ measured by rotorcraft UAS for: (a) 0600 LT to 0900 LT and (b) 0900 LT to 1200 LT for Case 1 and (c) 0600 LT to 0900 LT and (d) 0900 LT to 1200 LT for Case 2. From (Al-Ghussain and Bailey, 2022) and used with permission, license number 5513720396324.	66
6.6	Isocontours of (a) $\theta'_v(t, y)$ measured by fixed-wing UAS flying at $z = 50$ m for Case 1 with corresponding isocontours of $U'(t, y)$ shown in (b). Case 2 isocontours of $\theta'_v(t, y)$ and $U'(t, y)$ at $z = 50$ m shown in (c) and (d), respectively. The black line on the figures indicates the zero-level contour line for same data after low-pass filtering at $y \sim 200$ m in space and $t \sim 180$ s in time. From (Al-Ghussain and Bailey, 2022) and used with permission, license number 5513720396324.	67
6.7	Autocorrelations $\langle \langle R_{UU}(\Delta y, 0) \rangle \rangle$ measured at $z = 50$ m for (a) Case 1 and (b) Case 2 at different times. $\langle \langle R_{UU}(\Delta y, 0) \rangle \rangle$ measured between 0600 LT to 0700 LT at different altitudes for shown in (c) for Case 1 and (d) for Case 2. $\langle \langle R_{UU}(\Delta y, 0) \rangle \rangle$ measured from 1100 LT to 1200 LT at different altitudes shown in (e) for Case 1 and (f) for Case 2. From (Al-Ghussain and Bailey, 2022) and used with permission, license number 5513720396324.	72

6.8	Contours indicating magnitude of $\langle\langle R_{UU}(\Delta y, \Delta t)\rangle\rangle$ using observations made during Case 1 at $z = 50$ m from (a) 0600 LT to 0700 LT; (b) 0800 LT to 0845 LT; (c) 0945 LT to 10300 LT; and (d) 1100 LT to 1200 LT. Solid lines indicate where $\langle\langle R_{UU}\rangle\rangle = 0$. From (Al-Ghussain and Bailey, 2022) and used with permission, license number 5513720396324.	73
6.9	Contours indicating magnitude of $\langle\langle R_{\theta_v\theta_v}(\Delta y, \Delta t)\rangle\rangle$ using observations made during Case 1 at $z = 50$ m from (a) 0600 LT to 0700 LT; (b) 0800 LT to 0845 LT; (c) 0945 LT to 1030 LT; and (d) 1100 LT to 1200 LT. Solid lines indicate where $\langle\langle R_{\theta_v\theta_v}\rangle\rangle=0$. From (Al-Ghussain and Bailey, 2022) and used with permission, license number 5513720396324.	76
6.10	Contours indicating magnitude of (a) $\langle\langle R_{u^*w}(\Delta y, \Delta t)\rangle\rangle$ and (b) $\langle\langle R_{w\theta_v}(\Delta y, \Delta t)\rangle\rangle$ measured between 0945 LT and 1030 LT using observations made at $z = 50$ m during Case 1. $\langle\langle R_{u^*w}(\Delta y, \Delta t)\rangle\rangle$ and $\langle\langle R_{w\theta_v}(\Delta y, \Delta t)\rangle\rangle$ measured between 1100 LT and 1200 LT shown in (c) and (d), respectively. From (Al-Ghussain and Bailey, 2022) and used with permission, license number 5513720396324.	77
6.11	Contours of low-pass filtered u^*w'/u_τ^2 from observations made at $z = 50$ m (a) measured between 0800 LT and 0845 LT during Case 1 and (b) measured between 1100 LT and 1200 LT during Case 1. Solid lines indicate identified sweep events, dashed lines indicate identified ejection events. From (Al-Ghussain and Bailey, 2022) and used with permission, license number 5513720396324.	79
6.12	Contribution towards total (a) turbulence kinetic energy; (b) momentum flux; and (c) sensible heat flux by ejection and sweep events. Black dots indicate Case 1 and red dots indicate Case 2. From (Al-Ghussain and Bailey, 2022) and used with permission, license number 5513720396324.	81
6.13	Comparison of approximate scale of observed sweep and ejection events to estimated magnitude of momentum flux contribution. From (Al-Ghussain and Bailey, 2022) and used with permission, license number 5513720396324.	83
6.14	Conditionally averaged velocity vectors of ejection events from observations (a) measured between 0800 LT and 0845 LT during Case 1 and (b) measured between 1100 LT and 1200 LT during Case 1. Contours in (a) and (b) are of $w'/(u^*w' _{min})^{0.5}$. Contours of $\tilde{\omega}$ corresponding to the results shown in (a) and (b) are shown in (c) and (d) respectively. From (Al-Ghussain and Bailey, 2022) and used with permission, license number 5513720396324.	85
6.15	Conditionally averaged velocity vectors of sweep events from observations (a) measured between 0800 LT and 0845 LT during Case 1 and (b) measured between 1100 LT and 1200 LT during Case 1. Contours in (a) and (b) are of $w'/(u^*w' _{min})^{0.5}$. Contours of $\tilde{\omega}$ corresponding to the results shown in (a) and (b) are shown in (c) and (d) respectively. From (Al-Ghussain and Bailey, 2022) and used with permission, license number 5513720396324.	86

7.1	Overview of the developed vorticity probe. The superscripted p indicates that these coordinates are in the probe frame of reference.	92
7.2	Multi-hole probe automated calibration setup.	97
7.3	(a) Topographic map showing terrain surrounding measurement with (b) detailed satellite photograph of the area highlighted by the blue box in (a). (c) shows the fixed-wing and rotorcraft UAS used, along with an additional illustration of the different flight path altitudes. The red trajectories indicate the flight path of BC6B, which carried the vorticity probe whereas the orange trajectories indicate the flight path of BC6E which carried the standard five-hole probe.	101
7.4	Evolution of flow field background statistics with time: (a) $\langle u \rangle$ and $\langle v \rangle$; (b) $\langle k \rangle$; (c) $\langle \theta_v \rangle$ and (d) $\langle P \rangle / \langle \varepsilon \rangle$	102
7.5	Evaluation of the average dissipation rate measured by the vorticity probe throughout the three flights during the UKNRF campaign on August 17, 2022. (a) represents Flight 1 started at 0839 LT; (b) Flight 2 started at 1009 LT and (c) Flight 3 started at 1140 LT.	105
7.6	Spatial isocontours of dissipation rate measured by the vorticity probe during UKNRF campaign on August 17, 2022. (a) represents Flight 1 started at 0839 LT; (b) Flight 2 started at 1009 LT and (c) Flight 3 started at 1140 LT.	106
7.7	Spatial isocontours of virtual potential temperature fluctuations measured during UKNRF campaign on August 17, 2022. (a) represents Flight 1, which started at 0839 LT; (b) Flight 2 which started at 1009 LT; and (c) Flight 3 which started at 1140 LT.	108
7.8	Spatial isocontours of spanwise vorticity component measured by the vorticity probe during UKNRF campaign on August 17, 2022. (a) represents Flight 1 started at 0839 LT; (b) Flight 2 started at 1009 LT and (c) Flight 3 started at 1140 LT.	109
7.9	Momentum flux sorted by sweep and ejection events during UKNRF campaign on August 17, 2022. (a) Isocontours of Flight 1 which started at 0839 LT; (b) Isocontours of Flight 2 which started at 1009 LT; (c) Isocontours of Flight 3 which started at 1140 LT and (d) mean profile of the conditionally averaged momentum flux during the three flights.	111
7.10	Average structure of the streamwise (in a & b) and vertical velocity fluctuations (in c & d) sorted by sweep (denoted by sw) and ejection (denoted by ej) events during UKNRF campaign on August 17, 2022.	112
7.11	Heat flux sorted by sweep and ejection events during UKNRF campaign on August 17, 2022. (a) Isocontours of Flight 1, which started at 0839 LT; (b) Isocontours of Flight 2, which started at 1009 LT; (c) Isocontours of Flight 3, which started at 1140 LT and (d) mean profile of the conditionally averaged heat flux during the three flights.	113

7.12 Streamwise vorticity fluctuations sorted by sweep and ejection events during UKNRF campaign on August 17, 2022. (a) Isocontours of Flight 1, which started at 0839 LT; (b) Isocontours of Flight 2, which started at 1009 LT; (c) Isocontours of Flight 3, which started at 1140 LT and (d) mean profile of the conditionally averaged streamwise vorticity fluctuations during the three flights. 115

Chapter 1 Introduction

The atmospheric boundary layer (ABL) is an important component of earth that influences the living-beings by its dynamics in various imperceptible and perceptible ways. The planetary boundary layer (also known as the atmospheric surface layer) represents the lowest 10% of the ABL with direct interface with the earth's surface (Garratt, 1994; Bailey et al., 2019; Chu et al., 2019). Hence, this portion of the ABL significantly affects the dynamics of the atmosphere given that the exchange of mass, heat and momentum as well as the transport of anthropogenic and natural chemical constituents occurs in this layer (Monin and Obukhov, 1959; Garratt, 1994; Liu and Liang, 2010; Su et al., 2020; de Boer et al., 2022). This rapid exchange between the earth's surface and the troposphere through the surface boundary layer takes place due to the turbulent transport within it (Brown and Roshko, 1974; Huang et al., 2009; Marusic et al., 2010; Park et al., 2016; Bailey et al., 2019).

Furthermore, a significant contribution to this turbulent transport is carried out through large-scale turbulent motions referred to as coherent structures (e.g., Brown and Roshko, 1974; Gao et al., 1989; Robinson, 1991; Lu and Fitzjarrald, 1994; Huang et al., 2009; Marusic et al., 2010; Park et al., 2016). Coherent structures are defined as organized regions in the flow field with distinct characterizations that last for observable periods (Barthlott et al., 2007). As noted by Wyngaard (2010), coherent structures play an important role in the inertial cascade process. Large anisotropic structures act as an intermediary in the extraction of kinetic energy from the mean

flow, which is then transferred to smaller scales in the form of increasingly isotropic motions. In flows bounded by a surface, coherent structures have been identified from ramps in the temporal measurements, and early studies categorized them as either sweeps or ejections (Gao et al., 1989, 1992). Sweeps are so called because they are characterized by downward advection of high-speed fluid, whereas ejections are the upward advection of low-speed fluid. Coherent structures of many forms have been observed in various turbulent environments including experiments at laboratory scale (Hunt and Morrison, 2000; Hutchins and Marusic, 2007; Hutchins et al., 2009), and in atmospheric observations (Träumner et al., 2015; Lotfy and Harun, 2018; Lotfy et al., 2019; Alcayaga et al., 2020) as well as in flow simulations like Large Eddy simulation (LES) (Kim and Park, 2003; Kanda, 2006; Inagaki et al., 2012; Salesky and Anderson, 2018; Jayaraman and Brasseur, 2021).

With that being said, it is critical to study the ABL elements (including coherent structures) in detail to help better understand the physical and chemical processes which impact the ABL. Due to the importance of this region in exchange processes, such understanding will help in increasing the accuracy of weather and climate prediction models, particularly at micro-meteorological scales. Hence, numerous efforts have been invested toward understanding the physical and chemical processes in the atmosphere through atmospheric observations of various parameters with key variables being the atmospheric pressure, temperature, moisture content, wind speeds (Egger et al., 2002; Hobbs et al., 2002; Balsley et al., 2013; Witte et al., 2017; Bärffuss et al., 2018; Rautenberg et al., 2018; Jacob et al., 2018; Barbieri et al., 2019; Bailey et al., 2019; Boer et al., 2020), as well as suspended aerosol particle concentration

(Kumar et al., 2008; Petzold et al., 2008; Larouche and Boyer-Villemaire, 2010), and gas concentration (Wilson et al., 2010). These observations have been made using numerous measurement techniques including in-situ measurement systems deployed at the surface (Li et al., 2010; Wolfe and Lataitis, 2018), ground- or space-based remote sensing systems such as light detection and ranging (lidar) and radar systems (Wilczak et al., 1996; Engelbart et al., 2007; Shupe et al., 2008), and mobile measurement platforms such as aircraft, tethered balloons, and unscrewed aerial systems (UASs) (Bailey et al., 2020; de Boer et al., 2022). Each approach has strengths and weaknesses that govern the suitability of the acquired measurements for studying certain aspects of the dynamics of the atmosphere. Table 1.1 shows a summary of these weaknesses and strengths.

Table 1.1 Strengths and weaknesses of different measurement approaches utilized in atmospheric research (Bonin et al., 2012; de Boer et al., 2022).

Approach	Strengths	Weaknesses
Remote sensing	<ul style="list-style-type: none"> • Continuous operation • Provide volumetric information • Operation requires limited labor intervention (maintenance and data gathering) 	<ul style="list-style-type: none"> • Uncertainties associated with the measurement principle • Radar: challenging to collect data under clear air conditions • Lidar: measurements affected by the cloud cover • Expensive
Fixed In-situ (Tower measurements)	<ul style="list-style-type: none"> • Operation requires limited labor intervention (maintenance and data gathering) • Continuous operation 	<ul style="list-style-type: none"> • Measurements heights are usually limited to several meters above the ground

Mobile in-situ (Radiosondes ad dropsondes)	<ul style="list-style-type: none"> • Operation requires limited labor intervention (maintenance and data gathering) • Can be used for profiling the atmosphere 	<ul style="list-style-type: none"> • Fails to provide spatiotemporal information on the atmospheric properties
Crewed aircraft	<ul style="list-style-type: none"> • Provides spatiotemporal information on the atmospheric properties 	<ul style="list-style-type: none"> • Limited measurement periods • Labor intensive • Expensive to deploy • Cannot operate in hazardous environments; including severe weather conditions and at low altitudes
Tethered balloons	<ul style="list-style-type: none"> • Measure the profile of atmospheric properties through the lower part of the atmosphere (1-2km) 	<ul style="list-style-type: none"> • Labor intensive • Limited measurement periods • Incapable of capturing location-dependent gradients • Cannot operate in severe weather events
UASs	<ul style="list-style-type: none"> • Provide data at high spatiotemporal resolution • Relatively low-cost • flexibility in measurement location • Can operate close to the surface and in remote areas 	<ul style="list-style-type: none"> • Labor intensive • Limited measurements periods • Except in special cases, cannot operate severe weather conditions • Subject to regulatory restrictions

The advantages of UASs over traditional measurement systems has led to the rapid increase in their commercial development and increased the interest in finding new uses for them in diverse areas of atmospheric research. Important for the present

study, a UAS can traverse spatially through the flow over time scales faster than atmospheric time scales, allowing it to obtain a snap-shot of the turbulence structure along the flight path. In addition, due to their lower cruising speed (between 10 m s^{-1} and 30 m s^{-1}) compared with crewed aircraft (between 50 m s^{-1} and 200 m s^{-1}), UASs have the ability to acquire measurements with higher spatial resolution with the same sampling rate (Bärfuss et al., 2018; Zhou et al., 2018; Barbieri et al., 2019). Hence, UASs have been increasingly explored for research sampling thermodynamic and kinematic variables associated with atmospheric turbulence (Egger et al., 2002; Hobbs et al., 2002; Balsley et al., 2013; Witte et al., 2017; Rautenberg et al., 2018; Bärfuss et al., 2018; Jacob et al., 2018; Barbieri et al., 2019; Bailey et al., 2019). Here, we show the ability of UASs to be used for the characterization of ABL structure and the identification of coherent structures. For this purpose, we present two approaches; the first approach compiles single- and multi-point statistics using data from multiple UASs, each equipped with a single multi-hole probe flying simultaneously whereas the second approach employs a single UAS equipped with a custom multi-hole-probe-based vorticity probe that is capable of measuring velocity gradients over small scales.

The remainder of the dissertation is organized as follows: Chapter 2 acts as a literature review addressing different topics relevant to the current study; Chapter 3 highlights the literature gap and the contribution of this dissertation toward bridging that gap. Chapter 4 presents a description of the procedures used to extract wind velocity from multi-hole probe measurements from a UAS; Chapter 5 presents an approach that was developed and used to minimize the biases in the multi-hole probe-based wind measurements which was extracted from work published in Al-Ghussain

and Bailey (2021); Chapter 6, extracted from our published work in (Al-Ghussain and Bailey, 2022), demonstrates the ability of UASs to characterize coherent structures in the ABL using multiple UASs flying simultaneously; Chapter 7 describes the development of a novel vorticity probe and discusses measurements conducted using the probe and their relevance to coherent structure investigations; and finally in Chapter 8 we summarize the main findings and conclusions. Since major parts of this dissertation are extracted from published work, readers may encounter different nomenclature. To ease the understanding of the dissertation, we define nomenclature the first time they appear.

Chapter 2 Background and Literature Review

2.1 Atmospheric Stability

The characteristics of the atmospheric boundary layer (ABL) are closely linked to atmospheric stability, which is strongly influenced by solar radiation. Throughout a typical day, the stability of the ABL is affected by the diurnal cycle which produces either stable, convective, or neutral conditions within the ABL. At night, and with the absence of solar radiation, the ABL is characterized by stable conditions due to surface temperatures cooling through radiation and thereby becoming lower than the temperature of the atmosphere. The result is more dense air being located near the surface, with less dense air above it. As a result, the main source of turbulent production during the night becomes mechanical production (i.e. production due to wind shear), with the stable density gradients acting as a sink to turbulent energy (Hogan et al., 2009; Wood, 2012). During the day the solar radiation heats up the surface and creates a positive buoyancy production due to the air becoming less dense near the surface, with a result that unstable conditions form which enhance turbulent mixing (Oke, 2002). Finally, an ABL with high wind speeds or during the transition between stable and convective conditions can act as a neutral ABL. During neutral conditions, the air density near the surface is in equilibrium with the density above it, and the only source of turbulent production is that of mechanical production (Banta et al., 2006; Angevine, 2008; Tuononen et al., 2017; Manninen et al., 2018; Tian et al.,

2020).

Different parameters have been developed to assess the stability degree of the flow, such as bulk Richardson number and Monin—Obukhov length scale (Mohan and Siddiqui, 1998). Richardson number is defined as a dimensionless ratio between buoyant turbulence production and mechanical turbulence production. A critical Richardson number (often identified as being near 0.25) is considered as the stability threshold. For example Richardson numbers below 0.25 are considered unstable, and those above 0.25 are considered stable (Galperin et al., 2007). The Monin—Obukhov length scale is a ratio between the buoyant turbulence production and mechanical turbulence production which produces a dimension of length, and is usually employed to scale the depth of the boundary layer. Typically, positive Monin-Obukhov length scales reflect stable conditions, while negative values reflect unstable conditions, and infinite length scales reflect neutral conditions (Foken, 2006).

2.2 Atmospheric Surface-Layer Structure

Laboratory investigations of coherent structures that populate in canonical smooth-walled, neutrally stable, zero-pressure-gradient turbulent boundary layers have connected them to correlated vertical and horizontal velocity perturbations referred to as “sweeps” and “ejections”, previously identified as the key drivers of turbulence production and transport (Willmarth and Lu, 1972; Blackwelder and Kaplan, 1976; Robinson, 1991). Recent studies have also outlined that a hierarchy of coherent structures exists (Adrian, 2007; Jiménez, 2011) in canonical wall-bounded flow: sub-layer streaks (Kline et al., 1967); hairpin vortices (Head and Bandyopadhyay, 1981);

large-scale motions (LSMs) (Kim and Adrian, 1999; Guala et al., 2006; Balakumar and Adrian, 2007) attributed to self-organization of hairpin vortices into packets (Adrian et al., 2000; Ganapathisubramani et al., 2003; Tomkins and Adrian, 2003; Hutchins et al., 2005) and very-large-scale motions (VLSMs) or superstructures (Kim and Adrian, 1999; Tomkins and Adrian, 2005; Guala et al., 2006; Balakumar and Adrian, 2007; Hutchins and Marusic, 2007; Monty et al., 2007, 2009). Spectral analysis of LSMs and VLSMs indicates that they make a non-negligible contribution to turbulence kinetic energy and Reynolds stress production (Guala et al., 2006; Balakumar and Adrian, 2007), which distinguishes them from the inactive motions proposed by Townsend (1976).

The ABL is a non-canonical wall-bounded flow due to its non-stationarity as transitions between stable and unstable convective behavior caused by the diurnal changes in surface surface temperature and resulting heat flux between the surface and the air. Even in the ABL, coherent structures in the form of near-surface organized eddies with anisotropic turbulence characteristics are frequently observed (Drobinski et al., 2004) and verified as characteristic of the large-scale turbulence (Paw et al., 1992; Boppe et al., 1999; Krusche and De Oliveira, 2004). Specifically, signs of hairpin vortices have been observed in the ABL at low altitudes in a consistent way (Hommema and Adrian, 2003; Li and Bou-Zeid, 2011; Oncley et al., 2016; Heisel et al., 2018). These coherent structures, despite being poorly defined, have been cited as being responsible for up to 75% of the turbulent fluxes in the atmospheric surface layer (Gao et al., 1989) although a wide range of values have also been cited including, 40% (Lu and Fitzjarrald, 1994), 60% (Drobinski et al., 2004), 30% (Feigenwinter and Vogt,

2005) and 30–70% (Barthlott et al., 2007).

There has been evidence suggesting that the hierarchy of structures in the ABL could contain some of the same elements as that of canonical wall flows, including low-speed streaks and super-structures (e.g., Träumner et al., 2015; Lotfy et al., 2019) and persistent flow features in humidity patterns consistent with LSMs (Froidevaux et al., 2012). Low-speed streaks have also been found to form under neutral, slightly stable, and unstable conditions (e.g., Etling and Brown, 1993; Moeng and Sullivan, 1994; Kim and Park, 2003). In the ABL, the streaks are described as organized regions of low momentum stretched in the streamwise direction with streamwise length of 500 m to 2000 m and spanwise width of 100 m to 200 m (e.g., Moeng and Sullivan, 1994; Kim and Park, 2003; Newsom et al., 2008; Iwai et al., 2008; Alcayaga et al., 2020). The formation of these streaks is still under debate where some scholars (e.g., Dennis and Nickels, 2011; Lee et al., 2011; Baltzer et al., 2013) are in favor of mechanical origin (generating from the distortion of the Reynolds stresses by the mean wind shear near the surface) whereas others (e.g., Bailey et al., 2008; Bailey and Smits, 2010) are advocates of their formation through dynamic instability. These low-momentum regions have been connected to LSMs and VLMSs (Thomas and Foken, 2007; Horiguchi et al., 2012; Eder et al., 2013; Dias Júnior et al., 2013) with LSMs having time scales on the order of 15 s to 40 s whereas VLMSs have time scales between 60 s and 140 s. These streaks play a significant role in the transport of low-momentum fluid away from the surface (i.e. ejection events). They have also been found to cause an inflection in the velocity fluctuations profile in the streamwise direction which creates a localized region of intense vorticity that is then stretched by

the streamwise mean wind speed and lifted by the vertical velocity to form hairpin vortices. As a consequence of mass conservation the ejection event is followed by a sweep event that transfers the high-speed fluid toward the surface (Harun and Reda Lotfy, 2019).

There is also evidence that the boundary-layer stability can alter the organization of coherent structures. For example, their inclination angle (in the streamwise-wall-normal plane) is typically related to the vertical velocity gradient (Liu et al., 2017; Lotfy and Harun, 2018; Liu et al., 2019). Under neutral conditions in the laboratory, the inclination angle of these structures (typically determined through multi-point correlations) has been measured to be 12° . When measured under different stability conditions, this angle has been observed to be 15° under stable conditions and between 10° to 56° under unstable (convective) conditions (Chauhan et al., 2013; Lotfy and Harun, 2018; Salesky and Anderson, 2018; Lotfy et al., 2019). Additionally, it has been found that the stability of the ABL affects the signature of coherent structures within time series measured at a point in space (Krusche and De Oliveira, 2004; Barthlott et al., 2007). Under stable conditions, the time series of velocity contain either a gradual decrease followed by a sudden increase or a fast increase followed by a gradual decrease (Krusche and De Oliveira, 2004; Barthlott et al., 2007). Conversely, under unstable conditions, coherent structures appear in the velocity time series as a ramp of slow and almost constant increase with a quick return to baseline level (Chen Michael D.; Black, T. Andrew; Lee, Xuhui, 1997).

In addition, the ABL has also been found to contain additional large coherent motions in the form of convective rolls on the order of several kilometres (e.g., Kelly,

1982; Etling and Brown, 1993; Weckwerth et al., 1997; Drobinski et al., 1998; Weckwerth et al., 1999; Salesky et al., 2017; Chow et al., 2019). These structures are developed in the presence of both buoyant and mechanical production under moderate convective conditions and high Reynolds numbers (Sikma et al., 2018) where the formation of these rolls have also been described as being analogous to the formation of the smaller-scale low-speed streaks (LeMone, 1973; Etling and Brown, 1993; Weckwerth et al., 1997, 1999; Jayaraman and Brasseur, 2021).

2.3 Uncrewed Aircraft Systems in Atmospheric Research

The need for dense spatio-temporal observations within the ABL has been highlighted by several researchers and national reports (e.g., National Research Council, 2007, 2009; National Academies of Sciences; Engineering and Medicine, 2018; Greene, 2022; Abraham and Hong, 2022) with dense observations required for investigating and characterizing coherent structures (Abraham and Hong, 2022). To address this need, UASs have been identified due to their potential for acquisition of high-resolution spatio-temporal observations (Chilson et al., 2019; McFarquhar et al., 2020; Pinto et al., 2021). Uncrewed aircraft systems can also bridge the data-gap which exists between the upper bound of ground-based measurements and lower bound of crewed-aircraft, provide longer and more controlled observations than tethered balloons and radiosondes, and can cover larger spatial domain (Adkins et al., 2020).

Uncrewed aircraft systems can be divided into two categories: fixed-wing and multirotor aircraft. Although not limited to these roles, fixed-wing aircraft are typically better suited to horizontal profiling (or ‘transects’) whereas multirotor aircraft are

usually employed vertical profiling. This is due to the multirotor aircraft’s ability to operate in confined places, and ability to be programmed to acquire measurements by hovering at a certain location or fly continuously along a trajectory at a speed selected to provide a specified spatial resolution. Such characteristics enable measurements in challenging locations such as within urban environments (Adkins et al., 2020) or complex topography. Additionally, multirotor aircraft are often better able to maintain position in gusty conditions than fixed-wing aircraft making operation of multirotor aircraft in these conditions easier (Loxton et al., 2008; Watkins et al., 2010). However, multirotor aircraft have lower endurance than fixed-wing aircraft (which can operate for up to several hours) (Adkins et al., 2020; González-Rocha et al., 2020; Bailey et al., 2020; Al-Ghussain and Bailey, 2022) and can carry less payload, which often limits their sensing ability (Greene, 2022). Fixed-wing aircraft tend to be more flexible in capabilities, being used to acquire observation at a high temporal and spatial resolution over both vertical or horizontal trajectories and at both high (Curry et al., 2004; Cassano et al., 2010; Knuth and Cassano, 2014; Kral et al., 2018) and low altitudes (Ramanathan et al., 2007; van den Kroonenberg et al., 2008; Houston et al., 2012). When employed together, fixed-wing UASs can characterize a region more broadly, allowing multirotor UASs to focus on specific areas of interest for vertical profiling if needed (Barbieri et al., 2019; Adkins et al., 2020; Al-Ghussain and Bailey, 2022). Such hybrid operation increases the value of the collected observations by providing superior spatio-temporal resolution (Adkins et al., 2020).

As a result, UASs have been employed extensively in various applications in at-

mospheric research over the last decade. To do so, UASs have been equipped with many different sensors to measure pressure (Barbieri et al., 2019), temperature (Broisy et al., 2017; Higgins et al., 2018; Barbieri et al., 2019), relative humidity (Broisy et al., 2017; Barbieri et al., 2019), atmospheric composition (Corrigan et al., 2008; Schuyler et al., 2019), and wind speed and direction (Barbieri et al., 2019; Al-Ghussain and Bailey, 2021, 2022) sensors. For instance, UASs have been used for investigating the evolution and structure of the ABL (e.g., van den Kroonenberg et al., 2007, 2008; Cassano et al., 2010; Bonin et al., 2013; Lothon et al., 2014; Wildmann et al., 2015; Bärffuss et al., 2018; de Boer et al., 2018; Kral et al., 2018; Bailey et al., 2019). Furthermore, UASs have been utilized to investigate turbulence (Mansour et al., 2011; Balsley et al., 2013; Båserud et al., 2016; Witte et al., 2017; Calmer et al., 2018; Bailey et al., 2019) and cloud microphysics (Ramanathan et al., 2007; Roberts et al., 2008). Both horizontal (Al-Ghussain and Bailey, 2022) and vertical measurements have been conducted (Bonin et al., 2013; Wainwright et al., 2015; Al-Ghussain and Bailey, 2022) in different environments such as the ABL over forests and other vegetation (Daida et al., 1994; Reuder et al., 2016; Broisy et al., 2017; Prior et al., 2020; Li et al., 2021), near wind turbines (Adkins and Sescu, 2017, 2018; Prudden et al., 2018), within the marine (Jonassen et al., 2012; Cook et al., 2013; Jonassen et al., 2015) and urban boundary layers (Adkins et al., 2020; Guimarães et al., 2020). Additionally, UASs have been used to study the meteorology of remote areas in the Arctic and Antarctic (Loxton et al., 2008; Mayer et al., 2012; Knuth et al., 2013; Cassano, 2014), analyze different surface fluxes (Reineman et al., 2016; Lee, 2017; Wang et al., 2019), study extreme weather events like hurricanes and tropical cyclones (Cione

et al., 2016, 2020) and near supercell thunderstorms (Elston et al., 2011). UASs have also been employed to monitor aerosol, and gas traces (Mayer et al., 2012; Schuyler and Guzman, 2017; Schuyler et al., 2019; Chiba et al., 2019; Inoue and Sato, 2022; Vinković et al., 2022) including near hazardous events like volcanic eruptions (Pieri et al., 2017) or gas leaks (Nathan et al., 2015) and investigate the ABL during natural events such as a solar eclipse (Bailey et al., 2019). Moreover, UASs have been used to enhance the performance of weather prediction models by feeding them with real time or near-real time observations (Ramanathan et al., 2007; van den Kroonenberg et al., 2008; Glasheen et al., 2019; Leuenberger et al., 2020). This increasing interest in UASs for atmospheric research has been motivated by a rapid increase in commercial airframe development and a corresponding decrease in sensor weight and cost.

2.4 Atmospheric Wind Measurements

The most common atmospheric properties acquired by UASs are pressure, temperature, relative humidity, and wind (Egger et al., 2002; Hobbs et al., 2002; Balsley et al., 2013; Witte et al., 2017; Bärffuss et al., 2018; Rautenberg et al., 2018; Jacob et al., 2018; Lotfy and Harun, 2018; Lotfy et al., 2019; Barbieri et al., 2019; Bailey et al., 2019; Boer et al., 2020; Alcayaga et al., 2020). Although the scalar quantities are relatively straightforward to acquire, obtaining all three components of the wind velocity vector is complicated by the presence of the continual translation and rotation of the measurement platform. This has resulted in different approaches being developed to determine the wind vector (Shevchenko et al., 2016; Rautenberg et al., 2018; Suomi and Vihma, 2018; Laurence and Argrow, 2018; Hemingway et al., 2020;

Thielicke et al., 2021): direct measurement using on-board wind-measuring instrumentation and subtraction of the aircraft kinematics (Cassano et al., 2016; Suomi and Vihma, 2018); indirect measurement using the attitude and position data recorded by the inertial measurement unit (IMU) and GPS, respectively (Suomi and Vihma, 2018); using both techniques in a complementary approach (Rautenberg et al., 2018); or through calibration of the aircraft’s kinematic and dynamic response to the wind (González-Rocha et al., 2020).

Various types of wind-measuring instruments have been employed on multirotor aircraft including hot-wire anemometers (Wolf et al., 2017; Cuxart et al., 2019; Molter and Cheng, 2020; Thielicke et al., 2021), sonic anemometers (de Boisblanc et al., 2014; Palomaki et al., 2017; Nolan et al., 2018; Shimura et al., 2018; Barbieri et al., 2019; Thielicke et al., 2021; Reuter et al., 2021), multi-hole probes (Prudden et al., 2018), vane anemometers (de Boisblanc et al., 2014), solid-state anemometers (Bruschi et al., 2009, 2016), microelectromechanical systems (MEMS) (Simon et al., 2022) and lidar systems (Vasiljević et al., 2020). Fixed-wing aircraft are usually equipped with either hot-wire anemometers (Canter, 2019) or multi-hole probes (Barbieri et al., 2019; Al-Ghussain and Bailey, 2021, 2022). Broadly speaking, wind measurements taken by sensors like sonic anemometers, single- and multi-hole pressure probes, and hot-wires tend to have higher temporal (and hence spatial) response (Suomi and Vihma, 2018) with multi-hole pressure probes frequently used (van den Kroonenberg et al., 2008; Spiess et al., 2007; Thomas et al., 2012; Elston et al., 2015) due to their high sampling frequency, lightweight, simplicity, accuracy and almost linear relation between pressure and velocity at large flow velocities (Suomi and Vihma, 2018). More impor-

tantly, multi-hole probes are able to resolve all three wind velocity components. The simplest multi-hole probe capable of resolving all three velocity components is the five-hole probe, composed of five holes arranged symmetrically on a semi-spherical or conical tip. When the wind velocity is oriented in different directions relative to the probe axis, each hole converts a different proportion of the dynamic pressure to stagnation pressure, allowing the dynamic pressure and direction to be determined using laboratory calibration of the probe's directional response.

The use of five-hole probes in UASs measurements has evolved from their employment in crewed aircraft measurements (Lenschow, 1970, 1972). As with crewed aircraft, UASs fly at velocities up to an order of magnitude greater than the wind velocity, hence their usage can be very sensitive to small errors in calibration and probe alignment (Suomi and Vihma, 2018; Laurence and Argrow, 2018). Furthermore, accurate position and orientation determination usually require very accurate orientation information (e.g. obtained through the use of dual-antenna combination GPS/IMU units) and accurate time-stamping of the data is critical to align sensor and flight data. Hence, it is vital to minimize the impact of unidentified and unquantified biases introduced during wind velocity measurement which result in contamination of the wind signal by the aircraft velocity.

2.5 Dissipation Rate Measurements in the Atmospheric Boundary Layer

The turbulent kinetic energy is a measure of the intensity of the turbulence and is defined as

$$k = \frac{1}{2} \langle u_i u_i \rangle \quad (2.1)$$

where summation index notation is employed, $\langle \rangle$ indicates an averaging process, and u_i are the Cartesian components of velocity fluctuations which themselves are defined using a process referred to as Reynolds averaging

$$u_i = U_i - \langle U_i \rangle. \quad (2.2)$$

Here U_i are the components of the time-dependent Cartesian wind velocity vector.

The turbulent kinetic energy (k) balance (also referred to as the turbulent kinetic energy budget) for the ABL is commonly described as

$$\frac{\partial k}{\partial t} = A + P + B + Tr - \varepsilon \quad (2.3)$$

where A is advection of k by the mean wind, P is mechanical (i.e. shear-driven) production of k , B is buoyant production of k and Tr is transport of k by turbulent motion. The final term is the viscous dissipation rate, which can be found from

$$\varepsilon = \nu \left\langle \left(\frac{\partial u_i}{\partial x_j} \right) \left(\frac{\partial u_i}{\partial x_j} + \frac{\partial u_j}{\partial x_i} \right) \right\rangle \quad (2.4)$$

with x_j the Cartesian components of the spatial direction vector. This equation shows that the viscous dissipation rate is the interaction of small-scale velocity gradients with kinematic viscosity, ν . This term reflects the rate of conversion of the turbulence's kinetic energy into heat. Thus ε , characterizes the rate of energy transfer is

important for meteorology (Banakh et al., 1999). Kolmogorov (1941) showed that at intermediate (referred to as inertial) scales the energy transfer from large-to-small scale eddies is also described by ε resulting in the relationship

$$E(\kappa) = \alpha\varepsilon^{2/3}\kappa^{-5/3} \quad (2.5)$$

with the eddy size described by the wavenumber, $\kappa = 2\pi/\lambda$, kinetic energy content at κ given by E and α a constant. The eddy wavelength is given by λ and Equation 2.5 is valid when $1/L \ll 1/\lambda \ll 1/\eta$, where L describes the wavelengths of the most energetic turbulent eddies and η describes the wavelengths at which dissipation occurs due to the process described by Equation 2.4.

In atmospheric turbulence, the Reynolds number is very high, resulting in a large separation between L and η making Equation 2.5 valid over most turbulent scales of interest in micrometeorology. Hence, the quantity ε is often used as a measure of turbulence intensity, particularly measurements of k are difficult to obtain in the non-stationary atmosphere due to the length of time required to obtain statistical convergence at the time scales corresponding to L .

There are established methods for estimating ε , which can be categorized into direct and indirect approaches. In the direct approach, the turbulent dissipation rate can be estimated from equation 2.4, however, this is challenging as it requires measuring all the velocity gradients in the three directions at very small separations. To overcome this challenge, several approaches have been proposed to simplify the estimation of the dissipation rate using the velocity gradients. For instance, assuming the small-scale turbulence is homogeneous and isotropic, the dissipation rate can be

estimated using one velocity gradient component (usually the streamwise component) such that

$$\varepsilon \approx 15\nu \left\langle \left(\frac{\partial u_1}{\partial x_1} \right)^2 \right\rangle. \quad (2.6)$$

The aforementioned approach is often used in laboratory studies employing measuring devices (e.g. hot-wire probes) which can often only measure a single component of velocity at a single location, but at high frequency. To obtain an approximation of the velocity gradients from the time rate of change, Taylor’s frozen hypothesis is used to transform the temporal gradient into a spatial one, specifically assuming $x_1 \approx \langle U_1 \rangle t$.

In the atmosphere, directional unsteadiness, precipitation and particulates make measuring with hot-wire probes challenging and it is difficult to obtain the velocity gradients at scales corresponding to η (approximately 1 mm). Therefore, the standard approach to determine ε is usually indirectly, through assuming Equation 2.5 is valid and obtaining by measuring $E(\kappa)$ over a measurable range of scales. Furthermore, as $E(\kappa)$ is the three-dimensional wavenumber spectrum which cannot be measured directly, it is usually evaluated in a single direction, $E_{11}(\kappa_1)$, often from the frequency spectrum of the streamwise component of velocity, $F_{11}(f)$, with the streamwise component of the wavenumber vector, κ_1 , approximated using Taylor’s hypothesis such that $\kappa_1 \approx 2\pi f / \langle U_1 \rangle$. Using this estimated streamwise velocity spectrum, ε can be estimated by identifying the range of κ_1 which follows a $-5/3$ slope and fitting equation 2.5 to that portion of the spectrum (O’Connor et al., 2010; Wang et al., 2021). For the one-dimensional spectrum $\alpha = 0.49$ is often used, although other values have also been employed. Note that this approach implicitly assumes Equation 2.5 is valid,

which may not be true in many situations.

Different measurement techniques have been deployed to estimate ε . Frequently these are measurements from sonic anemometers (Champagne, 1978; O'Connor et al., 2010; Muñoz-Esparza et al., 2018; Bodini et al., 2019; Wildmann Nicola; Lundquist, Julie K.; Bariteau, Ludovic; Wagner, Johannes, 2019) which have frequency response on the order of 100 Hz. Hot-wire anemometers which have frequency response on the order of 10 kHz are also used either on weather towers (Luce et al., 2019), on tethered balloons (Frehlich et al., 2006; Lundquist and Bariteau, 2015; Lonardi et al., 2022), on aircraft (Fairall et al., 1980) or on UASs (Lawrence and Balsley, 2013), but the fragility of these sensors limit their use. Various remote sensing instruments like wind profiling radars (Kantha and Hocking, 2011; McCaffrey et al., 2017) and lidars (Banakh et al., 1999; O'Connor et al., 2010; Bodini et al., 2018; Wildmann Nicola; Lundquist, Julie K.; Bariteau, Ludovic; Wagner, Johannes, 2019; Jiang et al., 2022) have also been employed. Typically all these approaches use some variation of Equation 2.5 to determine ε but, to a lesser extent, arrays of horizontal and vertical in-situ measurements have also been deployed to measure the atmospheric velocity gradients and are usually in the form of sonic anemometer (Carper and Porte-Agel, 2004) or hot-wire anemometer arrays (Freytag, 1978; Balint James M.; Vukoslavcevic, Petar, 1991; Klewicki et al., 1995; Folz and Wallace, 2010). Recently, it has also become increasingly viable to estimate ε from Equation 2.5 using observations from multi-hole probes on UASs (Bailey et al., 2019).

2.6 Vorticity Measurement in the Atmospheric Boundary Layer

As previously noted, coherent structures have been clearly identified in the ABL, particularly through the use of arrays of sonic and cup anemometers (Segalini and Alfredsson, 2012), sonic detection and ranging (sodar) (Drobinski et al., 1998; Pertenko and Bezverkhii, 1999), lidar (Froidevaux et al., 2012), and particle image velocimetry (PIV) in controlled situations (Takimoto et al., 2011). Within the ABL, turbulence structure is typically inferred from stationary (in-situ) measurement systems where coherent structures are associated with organized regions over time and space observed in the wind and temperature measurement (Wilczak, 1984). However, this usually requires the spatial distribution of wind to be inferred using Taylor’s frozen-flow hypothesis, which is poorly realized at large scales, particularly within non-stationary flow and subject to the diurnal stability cycle (Metzger and Holmes, 2008). This shortcoming can be overcome by using multiple synchronous measurement systems at different locations (Ingenhorst et al., 2021). For instance, studies examining coherent structures have employed multiple sonic anemometers (Sadani and Kulkarni, 2001; Barthlott et al., 2007; Inagaki and Kanda, 2010; Liu et al., 2019; Gu et al., 2019; Lotfy et al., 2019), single Doppler-lidar systems (Drobinski et al., 2004; Träumner et al., 2015; Valdecabres et al., 2016; Alcayaga et al., 2020), dual Doppler-lidar (Iwai et al., 2008; Newsom et al., 2008; Träumner et al., 2015; Alcayaga et al., 2022) and hot-wire probes (Lotfy and Harun, 2018). Large-eddy simulation (LES) has also been increasingly applied to the study of atmospheric-boundary-layer turbulence (Inagaki et al., 2012), but due to the high Reynolds numbers of the ABL,

LES cannot resolve the near-wall eddies and frequently relies on wall models. As noted by (Senocak et al., 2007), such models can alter the arrangement of large-scale coherent structures.

In general, coherent structures are organized large-scale regions of similar values of vorticity which advect with the flow and evolve as a system (Hussain, 1983, 1986). Vorticity, is a vector quantity used as a measure of angular velocity of the fluid at a point in space and often defined as the curl of the local velocity vector. Hussain (1983) implied that the coherence of turbulent structures is caused by the phase organization within the vorticity fields. In sweep and ejection events, vorticity is generated by the shear between the fast-moving fluid in the center of the event and the slower-moving fluid on its edges. This shear creates the vorticity characteristic to coherent structures (e.g. hairpin vortices Adrian, 2007; Hutchins and Marusic, 2007). Similarly, studies like Carper and Porte-Agel (2004) suggest that a central core of vorticity, surrounded by sweep and ejection events and a regional rise in shear stress and scalar flux, are the signatures of hairpin vortices in the ABL.

The velocity components acquired at two or more spaced points are required to derive different components of the vorticity vector, ω_i following

$$\omega_1 = \left(\frac{\partial U_3}{\partial x_2} - \frac{\partial U_2}{\partial x_3} \right) \quad (2.7)$$

$$\omega_2 = \left(\frac{\partial U_1}{\partial x_3} - \frac{\partial U_3}{\partial x_1} \right) \quad (2.8)$$

$$\omega_3 = \left(\frac{\partial U_2}{\partial x_1} - \frac{\partial U_1}{\partial x_2} \right) \quad (2.9)$$

The spacing between the measurement points used to find the gradient defines the spatial resolution of the derived vorticity field. Some literature, such as He et al.

(2002), state that the spacing should be close to η also referred to as the Kolmogorov microscale, formally defined as

$$\eta = \left(\frac{\nu^3}{\varepsilon} \right)^{1/4}, \quad (2.10)$$

and indicating the approximate size of the smallest eddies of dynamical importance in a turbulent flow. In contrast, other studies report the possibility of obtaining accurate vorticity values from measurement points separated by as much as 6η (Vukoslavčević et al., 1991). Whereas, Freestone (1988) suggested that the spacing between probes should be 5-10 mm for their vorticity measurements in wind tunnels (which typically can have values of η on the order of microns).

Most vorticity probes in laboratory flows use multiple hot-wire probes separated by small distances from each other, with as many as 12 individual hot-wires located on a single probe (Wallace John F., 1995); such configuration can be utilized for vorticity measurements and hence often referred to as a 12-sensor vorticity probe even though they are also able to measure velocity and velocity gradients. Notably, following equation 2.4, the estimated velocity gradients acquired by a vorticity probe can be used for dissipation rate estimation (Wyngaard, 1969; Andreopoulos and Honkan, 1996).

Kovaszny (1954) was the first to propose the use of vorticity probes for velocity and vorticity measurements utilizing a 4-sensor hot-wire configuration and several researchers have used this design for vorticity measurements in isotropic turbulent flows (Kistler, 1952; Kastrinakis Helmut; Willmarth, William W., 1979; Kim and Fiedler, 1989). Additionally, studies presented different modifications able to mea-

sure one, two, or all three vorticity components. For instance, four (Vukoslavčević James M., 1981; Park and Wallace, 1993; Antonia Yonggang; Shafi, H. S., 1996), five (Eckelmann Stavros G.; Brodkey, Robert S.; Wallace, James M., 1977), six (Kim and Fiedler, 1989; He et al., 2002), nine (Balint James M.; Vukoslavcevic, Petar, 1991; Vukoslavčević et al., 1991; Marasli P.; Wallace, James M., 1993; Vukoslavcevic James M., 1996) and twelve sensors (Tsinober Eliezer; Dracos, T., 1992; Folz and Wallace, 2010) have all been developed. Even though hot-wire probes have the ability to acquire wind speeds at a high temporal frequency they are fragile and difficult to handle (Thielicke et al., 2021), making them difficult to use for atmospheric flows. On the other hand, pressure probes are attractive alternatives that can be used for vorticity measurements and Freestone (1988) presented the use of four Conrad yawmeters with one pitot tube to measure the yaw vorticity in unsteady flow. However, many probe configurations still require the spatial direction along the probe axis to be interfered using Taylor's hypothesis.

Chapter 3 Motivation and Objectives

Studying the characteristics of the ABL during the early morning transition from stable, to neutral, to convective conditions provides an opportunity to examine its structure throughout all phases of stability. In addition, in the early morning the ABL frequently lacks complex boundary conditions such as clouds (Bange et al., 2007) and shear-driven turbulence is dominant during this period (Lapworth, 2006; Angevine et al., 2001; Beare, 2008) which makes it easier to study and describe the turbulence characteristics during. There have been relatively few concerted UAS deployments investigating the morning transition process (Bange et al., 2007; Bennett et al., 2010; Wildmann et al., 2015; Higgins et al., 2018) and none of these studies (to the best of our knowledge) have investigated the characteristics of the coherent structures in the surface boundary layer during the morning transition.

In this work, we use different UAS configurations to investigate the organized structure in the ABL. By conducting measurements during the morning transition, we are able to examine changes to the structure associated with different stability conditions. The first set of measurements were conducted using velocity measurements conducted using a mutli-hole-probe and it was found that it was possible to produced improved accuracy in these measurements through use of an a posteriori correction. To obtain more detailed statistics about the structure of the turbulence, a vorticity probe was developed which was able to resolve vorticity and dissipation rate distributions. A second set of measurements was conducted which examined the

structure of turbulence during morning transition using this new probe.

This thesis thus seeks to:

- Present the approach which was developed to minimize the impact of unidentified and unquantified biases introduced during wind velocity measurements, resulting in contamination of the wind signal by the aircraft velocity;
- Present results from the use of UASs to resolve the structure and evolution of coherent structures which form during the morning transition;
- Describe the development and procedures for use of the new vorticity probe;
- Demonstrate the use of the vorticity probe on UASs for the detection and characterization of coherent structures in ABL.

Chapter 4 The Multi-hole Probe Measurement Approach

This chapter and Chapter 5 are adapted from work published in Al-Ghussain and Bailey (2021) which addresses improvements to multi-hole probe measurements made with UAS by developing an optimization approach that minimizes the effect of aircraft motion on the measurements of wind in the inertial frame.

Multi-hole probes are an adaptation of the common Pitot-static probe to allow the determination of relative wind direction as well as magnitude. Widely used in laboratory wind-tunnel studies of three-dimensional flow fields, they found use in crewed-aircraft studies of atmospheric wind (Axford, 1968; Lenschow, 1972; Treaster and Yocum, 1978) before being adopted for UAS use. Although configurations employing up to 17-holes have been developed the five-hole probe, being the simplest and lightest multi-hole probe capable of resolving all velocity components, is most commonly used on UASs. The arrangement of the normal vector of each plane of the holes on the probe tip typically consists of a central hole with normal vector in line with the probe axis, measuring pressure p_1 , and with the normal vector of the remaining holes at an angle to the probe axis. Two holes measure the pressure at opposing directions on the horizontal plane e.g. p_2 and p_3 , with the remaining two on opposite directions on the vertical plane, e.g. p_4 and p_5 . Static pressure, p_s is also measured, either through a ring of holes oriented perpendicular to the probe axis, or through an alternate pressure port. Wind tunnel calibrations are used to determine

calibration coefficients, for example

$$C_{P_{yaw}} = (p_2 - p_3) / (p_1 - \bar{p}) \quad (4.1)$$

$$C_{P_{pitch}} = (p_4 - p_5) / (p_1 - \bar{p}) \quad (4.2)$$

$$C_{P_{total}} = (p_1 - p_0) / (p_1 - \bar{p}) \quad (4.3)$$

$$\bar{p} = (p_2 + p_3 + p_4 + p_5) / 4, \quad (4.4)$$

where $p_0 = 0.5\rho|\vec{U}_m|^2 + p_s$ is the total pressure, ρ the density of the air and $|\vec{U}_m|$ the magnitude of the relative air velocity vector \vec{U}_m . During calibration p_1, p_2, p_3, p_4, p_5 and p_s are measured at different sideslip, β , and angle of attack, α , angles at known p_0 . Depending on the specifics of the probe geometry, a unique set of coefficients is recovered for each α and β combination up to some limit (referred to as the cone angle) typically between 25° and 45° depending on the specifics of the probe geometry. During measurement $p_1 - p_s, p_2 - p_s, p_3 - p_s, p_4 - p_s$, and $p_5 - p_s$ are simultaneously sampled and $C_{p_{yaw}}, C_{p_{pitch}}$ calculated for each sample. The known dependence of α, β and $C_{p_{total}}$ on $C_{p_{yaw}}, C_{p_{pitch}}$ from the calibration is then applied to determine α, β and p_0 which, when combined with a known ρ , provides the air velocity and direction relative to the probe axis. After estimating α and β , the 3D wind speed measured by the sensor can be found using

$$u = |\vec{U}_m| / D \quad (4.5)$$

$$v = |\vec{U}_m| / (D \times \tan(\beta)) \quad (4.6)$$

$$w = |\vec{U}_m| / (D \times \tan(\alpha)), \quad (4.7)$$

where u is the streamwise wind speed, v is the spanwise wind speed, w is the vertical wind speed and D is calculated as,

$$D = \sqrt{(1 + \tan(\alpha)^2 + \tan(\beta)^2)}. \quad (4.8)$$

When implemented on a moving platform such as an aircraft, \vec{U}_m is no longer the wind velocity but is instead a combination of the aircraft and wind velocity vectors

$$[\vec{U}_m]_B = [\vec{U}]_B - [\vec{U}_s]_B \quad (4.9)$$

where \vec{U}_s is the velocity vector of the sensor and \vec{U} is the desired wind velocity vector. We have also introduced the subscript B to indicate that these velocities are in a body-fixed frame of reference, i.e. a coordinate system attached to the aircraft. Due to the pitch, roll and yaw angles of the aircraft, $\vec{\Omega} = [\theta \ \phi \ \gamma]$, or more specifically their time rate of change $\dot{\vec{\Omega}}$, \vec{U}_s can experience additional velocity relative to the aircraft velocity $\vec{U}_{ac} = [U_{ac} \ V_{ac} \ W_{ac}]$ (Lenschow and Johnson, 1968) such that

$$[\vec{U}_s]_B = [\vec{U}_{ac}]_B + [\dot{\vec{\Omega}} \times \vec{r}]_B \quad (4.10)$$

where \vec{r} is the distance vector between the aircraft center of gravity and the measurement volume on the probe.

Note that the desired quantity is $[\vec{U}]_I = [u \ v \ w]$, the wind velocity vector in the Earth-fixed inertial frame of reference. Furthermore, \vec{U}_{ac} is also typically measured in the Earth-fixed inertial frame (e.g. through global positioning system) and therefore a transformation matrix \vec{L}_{BI} must be determined using the aircraft's pitch (θ), roll (ϕ), and yaw (γ) angles in the inertial frame. The velocity vector $[\vec{U}_{ac}]_I$ along with θ , ϕ , γ and their rates as required to build $\vec{\Omega}$ and \vec{L}_{BI} can be measured by an on-board

inertial measurement unit and GPS, and are commonly provided by most autopilots used for UASs operation. Thus, providing enough information to determine $[\vec{U}]_I$ from $[\vec{U}_m]_B$.

However, as noted earlier, \vec{U}_s is often an order of magnitude larger than the desired \vec{U} , making the process sensitive to an abundance of small biases. For example, the procedure above assumes perfect alignment between the probe's coordinate system and the aircraft's coordinate system. It also assumes that the $\vec{\Omega}$ and \vec{L}_{BI} are measured at the aircraft's center of gravity; that r is precisely known; that there are negligible flow blockage effects in the wind tunnel calibration or from the aircraft fuselage; and that all sensors are free of error. Although every effort can be made to minimize these biases, they are unlikely to be removed completely. The result is that \vec{U} is often contaminated by \vec{U}_s . This is most evident when \vec{L}_{BI} , \vec{U}_{ac} and $\vec{\Omega}$ are changing rapidly. To address the development of the correction approach described in Chapter 5.

Chapter 5 Approach for Minimizing Aircraft Motion Bias in Multi-Hole Probe Wind Measurements

Here, we present an approach that can be implemented *a posteriori* to minimize the impact of unidentified and unquantified biases introduced during wind velocity measurement, resulting in contamination of the wind signal by the aircraft velocity. In the following sections, we present a simple automated optimization that is designed to identify and remove these biases and demonstrate that this approach improves the wind estimate of an existing dataset.

5.1 Correction Procedure

5.1.1 Correction Procedure: Version 1

The net effect of the majority of biases can be summarized as influencing four parameters. Misalignment of probe and aircraft axes, calibration errors, and aerodynamic distortion of the flow around the probe will introduce bias errors into the time-dependent pitch, roll and yaw angles $\theta(t)$, $\phi(t)$ and $\gamma(t)$, which relate the measured velocity vector in body-frame coordinates to the aircraft velocity vector. In addition, calibration errors, transducer errors, and airframe aerodynamic effects (e.g. airframe blockage and streamline deflection due to the generation of lift) can also influence the direction of airflow relative to the probe as well as the magnitude of the measured dynamic pressure $Q(t) = 0.5\rho(t)|\vec{U}_m(t)|^2$ relative to the true dynamic

pressure. Note that the distortion of the flow may also depend on lift production of the aircraft and therefore $Q(t)$ may also include dependence on lift coefficient, which is not considered in the version of the corrections described here. Finally, it is also important for all sensor readings to precisely correspond to orientation readings in time to allow precise removal of aircraft motion from measured relative air velocity. However, implementation of software and differences in sensor time response can cause a delay between when probe measured velocity and aircraft measured velocity occur, e.g. the values of $\vec{U}_m(t)$ and $\vec{U}_s(t)$ may not correspond to the same t . The proposed correction procedure assumes that these values are biased in a way such that

$$\theta(t) = \theta_m(t) + \Delta\theta \quad (5.1)$$

$$\phi(t) = \phi_m(t) + \Delta\phi \quad (5.2)$$

$$\gamma(t) = \gamma_m(t) + \Delta\gamma \quad (5.3)$$

$$Q(t) = \zeta Q_m(t) \quad (5.4)$$

$$\vec{U}_m(t) = \vec{U}_m(t_m + \Delta t) \quad (5.5)$$

where the subscripted m indicates the measured value. The objective is then to find $\Delta\epsilon = \{\Delta\theta, \Delta\phi, \Delta\gamma, \zeta, \Delta t\}$. Using assumptions about how these biases will impact $\vec{U}(t)$ allows the determination of optimal values for $\Delta\epsilon$ which minimize this negative behavior. With $\Delta\epsilon$ known, we are able to remove its influence on the final time-series of $\vec{U}(t)$.

The assumptions used here are relatively straightforward. The first being that any biasing of $\vec{U}(t)$ by \vec{U}_s will result in $\vec{U}(t)$ having dependence on the direction of

travel of the aircraft. The second assumption we make is that the vertical component of $\vec{U}(t)$ will be approximately zero in the mean. This assumption may not hold in flight over sloped terrain or/and for relatively short flight domains (both spatial and temporal), in which case an alternative assumption may be needed. Moreover, we assume that the sensors have adequate response and the greatest error due to the specific configuration which logs IMU/GPS, pressure transducers, and PTU on three separate systems.

The correction procedure, as implemented, follows a multistage approach used to optimize $\Delta\epsilon$. This multistage approach was implemented to allow different objective functions to be used for different components of $\Delta\epsilon$. However, in practice, it is likely that a well-implemented single-stage optimization will achieve the same results.

The first step is to identify a portion of the flight that will be used to determine $\Delta\epsilon$. This portion should not include any significant acceleration or deceleration of the aircraft's horizontal ground speed (e.g. as experienced during takeoff or landing) and should include multiple changes of direction of the aircraft. In addition, the portion should be long enough to ensure that unsteadiness in the mean winds, e.g. as introduced by thermals, are averaged out. Ideally, devoting a portion of the flight after takeoff to conduct calibration orbits for later use in this process would be desired. With this portion of flight identified, the determination of $\Delta\epsilon$ is found by an optimization process seeking to minimize an objective function, δ , through iterative calculation of $[\vec{U}]_I$ (as described in Chapter 4).

Through perturbing $\Delta\epsilon$ and examining its influence on $\vec{U}(t)$ it was found that the standard deviation of the horizontal components of $[\vec{U}(t)]_I$, specifically $u(t)$ and

$v(t)$, were most sensitive to Δt (due to the aircraft flight being predominantly in the horizontal plane) with values of Δt as low as tenths or hundredths of a second contributing to large biases of the horizontal components of $[\vec{U}(t)]_I$. We thus first use a Nelder-Mead multidimensional unconstrained nonlinear minimization approach, implemented using the Matlab *fminsearch* command, to identify the value of Δt which minimizes the objective function δ , defined as

$$\delta_U = \langle u \rangle|_{U_{ac}>0} - \langle u \rangle|_{U_{ac}<0} \quad (5.6)$$

$$\delta_V = \langle v \rangle|_{U_{ac}>0} - \langle v \rangle|_{U_{ac}<0} \quad (5.7)$$

$$\delta = \delta_U^2 + \delta_V^2. \quad (5.8)$$

Note that $\langle \rangle|_{U_{ac}>0}$ indicates an average conditioned on when the aircraft is flying with positive inertial velocity component U_{ac} . Likewise $\langle \rangle|_{U_{ac}<0}$ indicates an average of all values obtained when the aircraft inertial U_{ac} velocity component is negative. The selection of U_{ac} vs V_{ac} for conditioning is arbitrary, and should be selected based on the actual flight trajectory flown. For flight trajectories without many trajectory changes, it was also found that the objective function

$$\delta = \langle (u - \langle u \rangle)^2 \rangle + \langle (v - \langle v \rangle)^2 \rangle \quad (5.9)$$

was equally effective, but relies on the assumption that the biases will act only to increase the fluctuations of the velocity signal at the probe. Here $\langle \rangle$ indicates an average over the entire portion of the flight used to find $\Delta\epsilon$. The resulting value of Δt which minimizes δ is then implemented in the remaining optimization stages.

The second stage follows a similar approach. Noting that the mean value of the vertical component of $[\vec{U}(t)]_I$, i.e. $w(t)$, is most sensitive to $\Delta\theta$, we then find the

value of $\Delta\theta$ that minimizes

$$\delta = \langle w \rangle \tag{5.10}$$

using $\vec{U}_m(t) = \vec{U}_m(t_m + \Delta t)$ as found above.

The remaining elements of $\Delta\epsilon$, specifically ζ , $\Delta\phi$ and $\Delta\gamma$, are then found by minimizing δ as defined in Eq. 5.8 using $\vec{U}_m(t) = \vec{U}_m(t_m + \Delta t)$ and $\theta = \theta_m + \Delta\theta$ as found in the preceding two stages.

Finally, to ensure that the values of $\Delta\epsilon$ determined using the latter optimization stages do not influence the values found during the earlier stages, $\Delta\epsilon$ is further refined by repeating the above three stages once again. In practice, this last step only influenced $\Delta\epsilon$ by one percent or less and likely can be omitted without loss of confidence in the final values of $\Delta\epsilon$.

5.2 Multi-Hole Probe Measurements Correction

With $\Delta\epsilon$ known, the biases described by $\Delta\epsilon$ can be removed following Eq.s 5.1 to 5.5 prior to a final determination of $[\vec{U}(t)]_I$. To validate this correction procedure, we applied it to measurement data acquired during the LAPSE-RATE campaign described in de Boer et al. (2018). The data was acquired using two different five-hole-probe-equipped fixed-wing aircraft, with the aircraft, probe, and data reduction procedures described in Bailey et al. (2020) with additional details available in Witte et al. (2017). We first demonstrate the correction procedure in flights compared to a ground reference, followed by a demonstration of the improvements made to vertical profiles of the wind velocity and direction.

5.2.1 Comparison to ground reference

A key part of the LAPSE-RATE campaign was an intercomparison study between numerous UASs measuring pressure, temperature, humidity, wind speed and wind direction. As detailed in Barbieri et al. (2019), the intercomparison was conducted by flying the UASs near the Mobile UAS Research Collaboratory (MURC) vehicle, which was equipped with a 15 m mast supporting reference instruments, including a sonic anemometer. For the fixed-wing aircraft used here, this comparison was performed by having the aircraft orbit the mast at 20 m above ground level with an orbit radius of 80 m. This orbit was performed for approximately 5 minutes before the aircraft ascended to 120 m to perform similar orbits for 2 minutes, then descending back to 20 m to resume the orbits around the tower for another 2 minutes before starting its landing pattern.

This circular flight pattern introduced a periodic variation in θ , γ and ϕ , with the period corresponding to the time to complete an orbit (approximately 25 s). Although convenient for the measurement of atmospheric parameters at a single geographic location, these types of orbits consist of the worst-case scenario for the contamination of the measured wind direction by the biases discussed in Chapter 4.

The periodicity is clearly evident in the estimated horizontal wind speed, $V_h = (u^2 + v^2)^{1/2}$, and direction, ψ , prior to implementing the corrections, as shown in Fig. 5.1a and 5.1b respectively. Although the general trends of the measured wind velocity and direction time series follow that of the reference velocity and direction, the magnitude of the fluctuations are clearly contaminated by the aircraft velocity

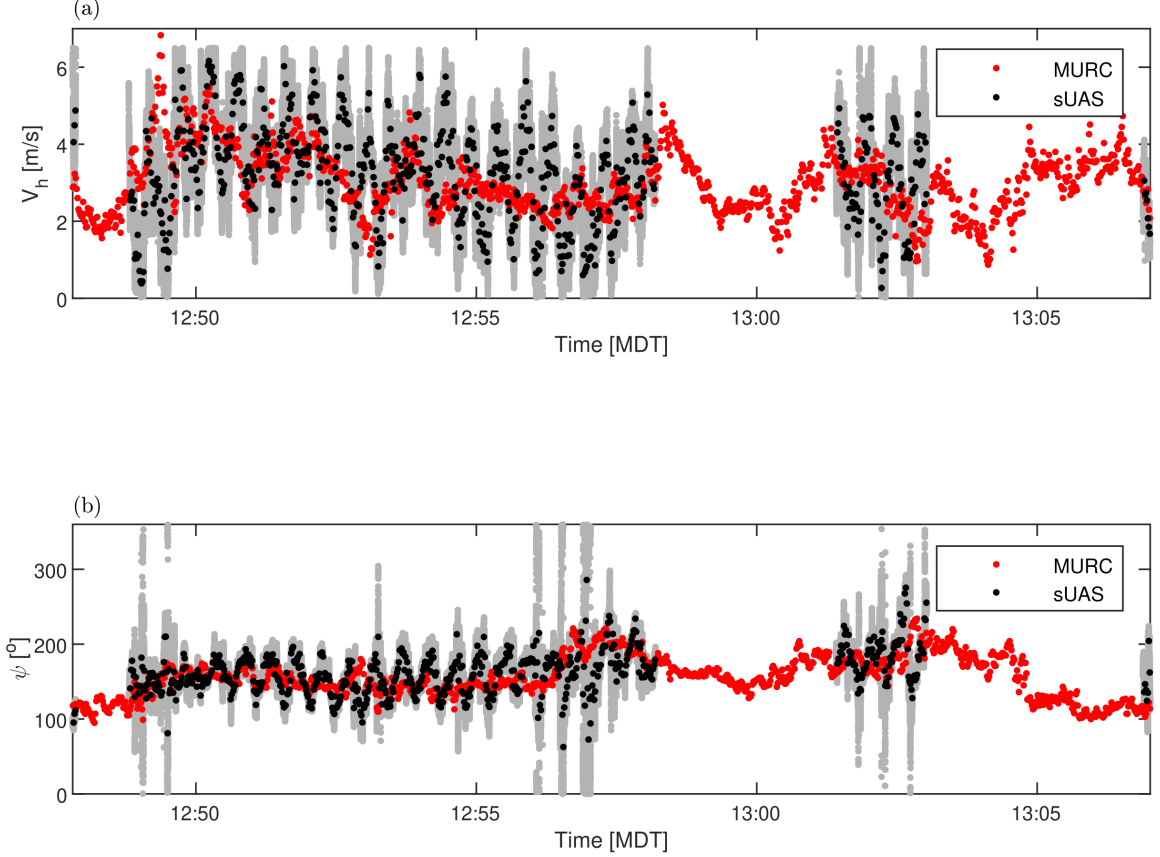


Figure 5.1 Comparison between uncorrected (a) horizontal wind speed and (b) wind direction measured by UASs to the reference signal measured by MURC. Gray lines indicate full signal from UASs, whereas black lines indicate same signal downsampled to same data rate as that of the MURC by plotting every 200th data point. From (Al-Ghussain and Bailey, 2021) and used under the Creative Commons Attribution 4.0 License.

and direction. The period in the wind signal is consistent with the time required to orbit the fixed mast at 25 s. Note that in Fig. 5.1 only the two portions of the flight where the UASs is at the same altitude as the reference sensors are presented.

The same time series are shown in Figs. 5.2a and 5.2b corrected following the procedure described in Section 5.1.1. The ten minutes of flight between 12:49 MDT and 12:58 MDT were selected to conduct the optimization of $\Delta\epsilon$. The the result of optimization was $\Delta\epsilon = \{\Delta\theta = -6.4^\circ, \Delta\phi = 0.9^\circ, \Delta\gamma = 2.1^\circ, \zeta = 1.07, \Delta t = -0.045\text{s}\}$ which highlights the sensitivity of the estimated wind velocity and direction to even

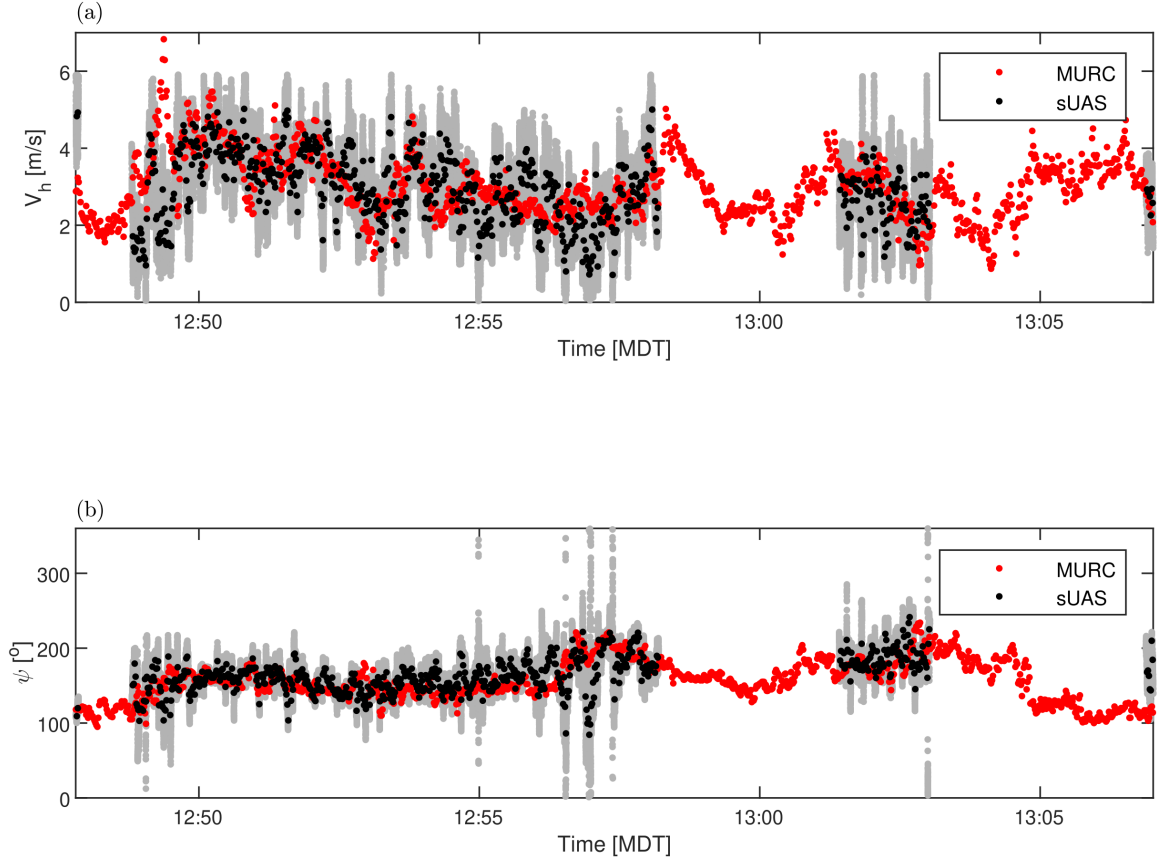


Figure 5.2 Small uncrewed aerial system-based wind measurements from Fig. 5.1 following correction compared to the reference signal measured by MURC: (a) horizontal wind speed and (b) wind direction. Gray lines indicate full signal from UASs, whereas black lines indicate same signal downsampled to same data rate as that of the MURC by plotting every 200th data point. From (Al-Ghussain and Bailey, 2021) and used under the Creative Commons Attribution 4.0 License.

small deviations from ideal orientations. As shown in Fig. 5.2. The corrected signals are now largely free of the 25 s periodicity, although there is some evidence of contamination between 12:56 MDT and 12:58 MDT. When the aircraft returns to 18 m altitude for the second set of orbits (which were not included in the optimization) there is little evidence of aircraft velocity contamination in the wind estimates.

The periodicity described above is more clearly evident in the difference between the power spectrum of horizontal wind speed calculated for both the corrected and uncorrected cases. These spectra are presented in Fig.5.3. The influence of the

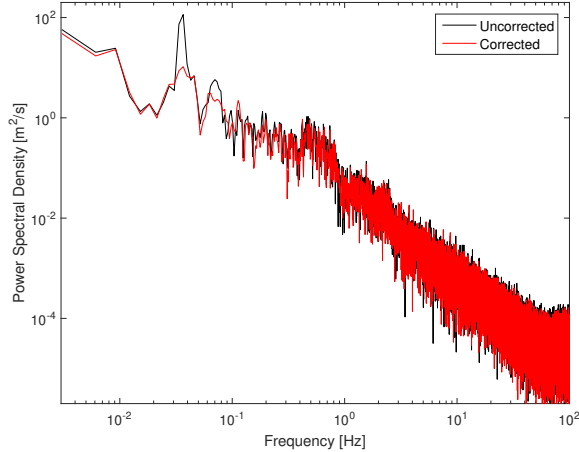


Figure 5.3 Power spectrum of horizontal wind magnitude calculated from uncorrected and corrected time series. From (Al-Ghussain and Bailey, 2021) and used under the Creative Commons Attribution 4.0 License.

periodic orbits of the aircraft is apparent in the uncorrected measurements as a spike at 0.035 Hz (consistent with an orbital period of 28 s). This spike is greatly reduced by the correction. Importantly, besides what appears to be a harmonic peak at 0.07 Hz which is also reduced, the remainder of the spectrum appears largely unaffected by the correction.

To provide a more quantitative comparison between the UASs and reference measurement, we directly compare the velocity magnitude and direction measured at each instant a sample was made by the ground reference. This comparison is presented in Fig. 5.4 in which a perfect comparison would result in the straight line as indicated on these figures. Note that, a perfect correlation should not be expected as the UASs and reference sensor were not collocated. Also shown as a dashed line on these figures are the bounds described by 2 standard deviations of the difference between the UASs and MURC measured values.

For the uncorrected velocity magnitude and direction, the comparison shown in

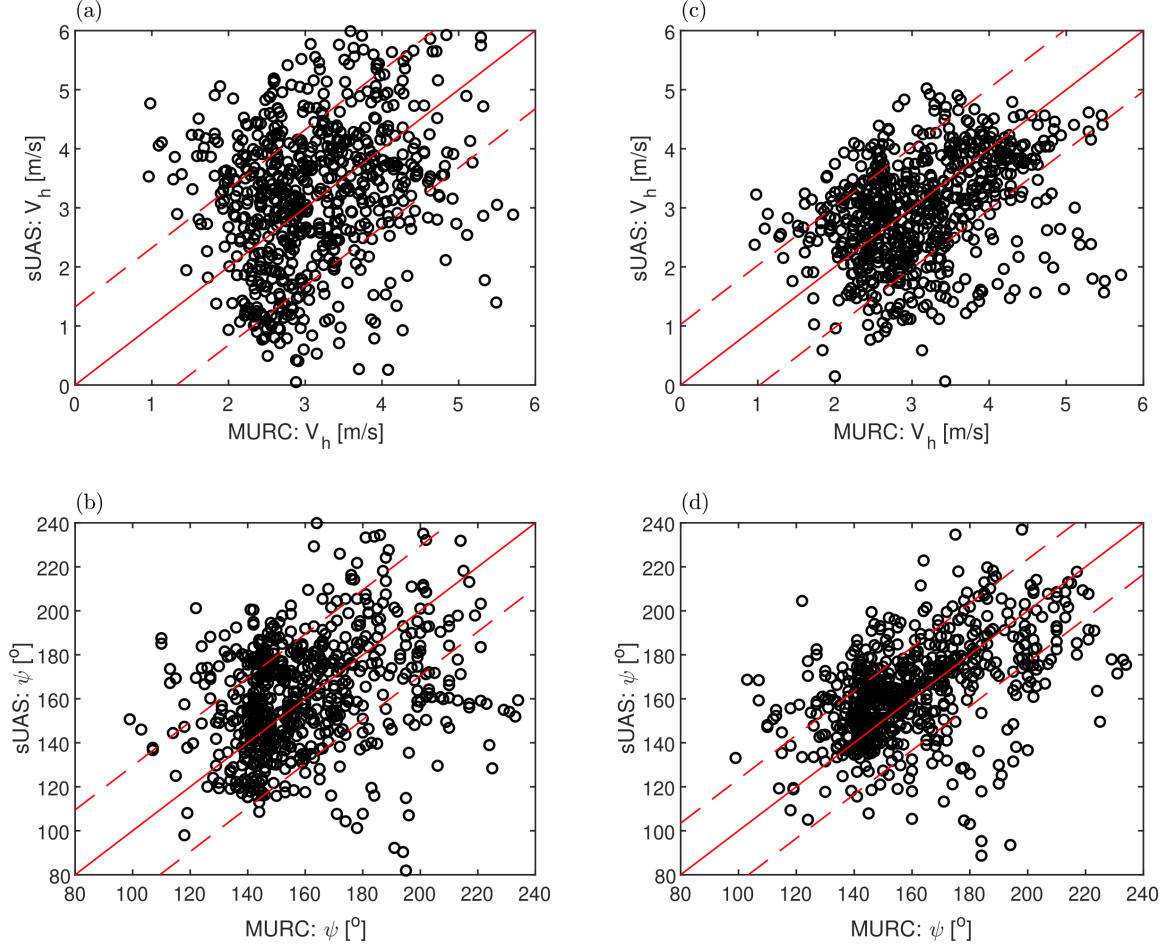


Figure 5.4 Direct comparison between (a) uncorrected and (c) corrected horizontal wind speed measured simultaneously by UASs and MURC. Similar comparison shown for (b) uncorrected and (d) corrected wind direction. Solid red line indicates line where both measurements are identical and dashed lines indicate 2 standard deviations of the difference between the UASs and MURC measured values. From (Al-Ghussain and Bailey, 2021) and used under the Creative Commons Attribution 4.0 License.

Figs. 5.4a and 5.4b reveals a broad spread about the reference line. This spread decreases significantly when the corrections are applied, as shown by comparison to Figs. 5.4c and 5.4d. The mean difference between the two measurements decreases by approximately 35% in magnitude and direction with correction, corresponding to an increase in the correlation coefficient from 0.13 to 0.19 in magnitude and 0.22 to 0.32 in direction. This increased correlation is reflected in the statistics. The

correction brings the standard deviation of the UASs measured velocity much closer to the reference signal. The standard deviation in magnitude measured by the UASs decreases from 1.2 m/s to 0.90 m/s, very close to the value of 0.86 m/s measured by the reference. For direction the standard deviation decreases with correction from 27° to 22° whereas it is 24° for the reference.

5.2.2 Implementation in profiling measurements: Version 1

The results of the comparison to the ground reference provide confidence in the success of the correction. To demonstrate the improvement offered by application of these corrections on vertical profiling by fixed-wing aircraft, we now examine their impact on profiles of wind speed and direction measured by two separate aircraft at different locations. These two fixed-wing aircraft were essentially identical in configuration to that described in Witte et al. (2017) and were flown at measurement sites separated by 16 km. Each aircraft measured an atmospheric profile every hour, with the two aircraft staggered in time by 30 minutes.

Each profile consisted of a 20 minute flight, with the aircraft performing a spiralling ascent to 900 m followed by a spiralling descent, with this pattern repeated until the 10Ah battery was expended. In the following discussion the times are those corresponding to when the profile measuring flight initiates with the X, Y, Z coordinate system's origin at the takeoff location. These particular profiles were selected for discussion as they were measured during the boundary layer transition, and represent different behaviors, including the presence of turbulence and variability in the wind direction. The wind speeds during these profiles were also low, producing a large ra-

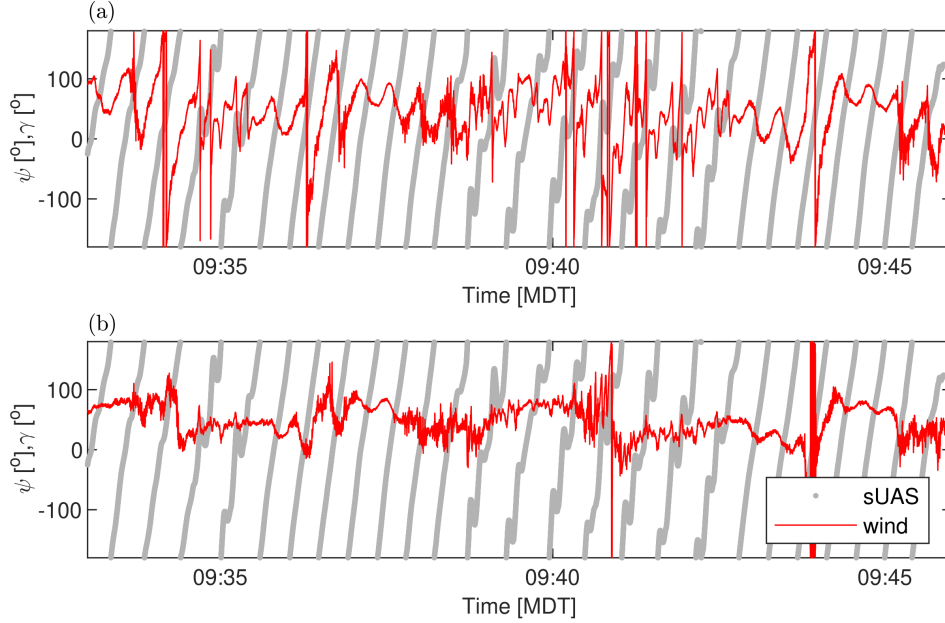


Figure 5.5 Comparison between measured wind direction and aircraft yaw direction for (a) uncorrected and (b) corrected signals as a function of time for a single flight. From (Al-Ghussain and Bailey, 2021) and used under the Creative Commons Attribution 4.0 License.

tio of aircraft velocity to wind velocity and therefore a challenging case to accurately extract the wind components from the five-hole-probe signal.

As previously mentioned, the orbital flight patterns also represented a challenge for extracting the wind data due to the periodic variation in θ , γ and ϕ introducing a corresponding periodic variation in $[\vec{U}(t)]_I$. This bias can be clearly illustrated by comparing γ to ψ , as done for an example flight in Fig. 5.5a. For this flight, the aircraft completed a full 360° turn in approximately 30 s, introducing a corresponding period in both the wind speed and direction before correction. Once the corrections have been applied, as shown in Fig. 5.5b, there is a distinct reduction of periodicity in the direction of the wind measured by the UASs.

The mean of the corresponding wind speed and direction profiles are presented in Fig. 5.6 for UAS 1 and Fig. 5.7 for UAS 2. In these figures both the uncorrected

and corrected mean profiles are displayed in order to show the relative improvement offered by application of the bias correction. For all profiling flights, the correction coefficients were determined by optimizing the entire flight once the aircraft was in its flight pattern. Before correction, the bias introduced by the aircraft trajectory is apparent as large coherent deviations from the general trend, mostly evident in the velocity magnitude, but also present in the direction. When the corrections were applied, these large deviations were greatly reduced, better representing the structure of the boundary layer throughout the profiles. In the wind velocity profiles presented in Fig. 5.6 for UAS 1 there were still high velocity deviations, even in the corrected profiles near the surface corresponding to when the aircraft was being manually controlled and experiencing strong accelerations. It has been found that the corrections presented here cannot completely remove the bias due to aircraft acceleration, suggesting a potential time response lag between the five-hole probe and the inertial measurement unit which agrees with what was reported in (Båserud et al., 2016) .

The corrected profiles show very different wind behaviors existed for the different sites and times. At the site measured by UAS 1, the profiles measured at 8:30 MDT and shown in Figs. 5.6a,b reflect the correspondence between the stable thermodynamic conditions throughout the boundary layer and the horizontal wind magnitude, with winds increasing from 2 m/s near the ground to 4 m/s at $Z = 900$ m and consistently between $\psi = 0^\circ$ and 100° . There was noticeably stronger velocity and direction fluctuations measured for $Z < 200$ m, indicating the presence of turbulence near the surface. This turbulence appears to have been still present at 9:30 MDT, as shown in

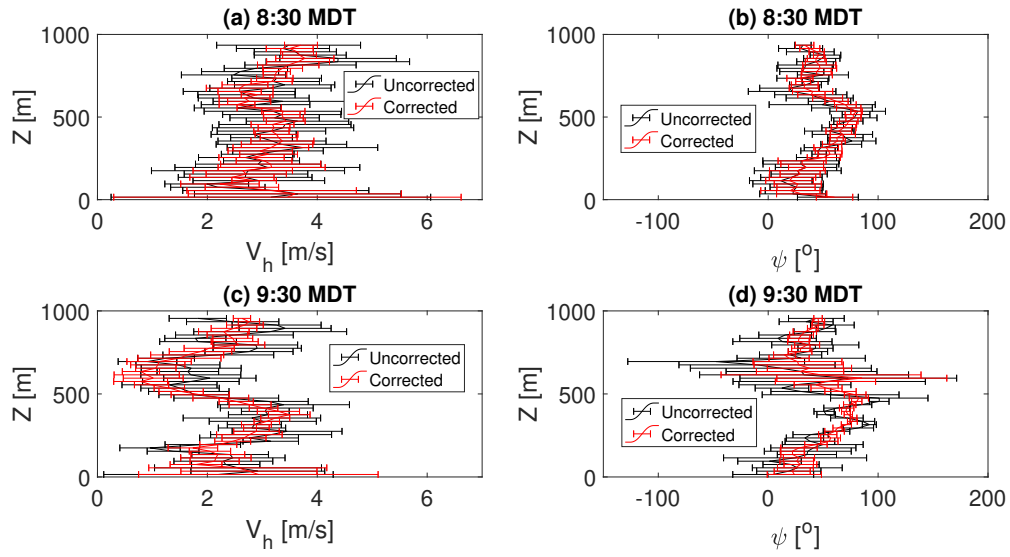


Figure 5.6 Comparison of mean (a) horizontal wind magnitude and (b) wind direction profiles measured by UAS 1 at 8:30 MDT with and without correction applied. Horizontal mean magnitude and direction profiles measured at 9:30 MDT shown in (c) and (d) respectively. From (Al-Ghussain and Bailey, 2021) and used under the Creative Commons Attribution 4.0 License.

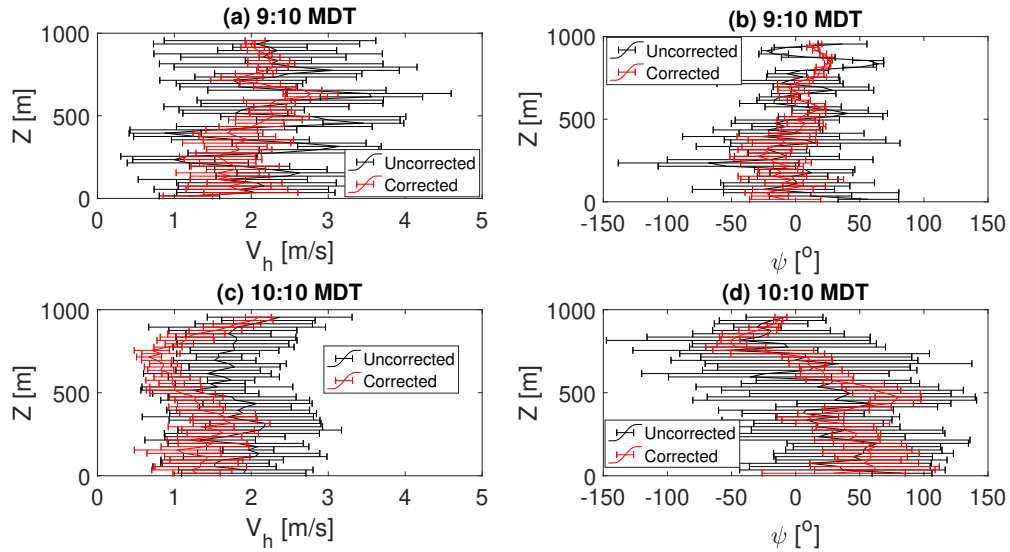


Figure 5.7 Comparison of mean (a) horizontal wind speed and (b) direction profiles measured by UAS 2 at 9:10 MDT with and without correction applied. Horizontal wind speed and direction profiles measured at 10:10 MDT shown in (c) and (d) respectively. From (Al-Ghussain and Bailey, 2021) and used under the Creative Commons Attribution 4.0 License.

Table 5.1 Components of $\Delta\epsilon$ determined by optimization for each UAS for both flights.

UAS	Flight	$\Delta\theta$	$\Delta\phi$	$\Delta\gamma$	ζ	Δt
1	8:30 MDT	-4.9°	0.17°	2.6°	1.1	0.98 s
1	9:30 MDT	-5.8°	2.7°	2.1°	1.1	0.01 s
2	9:10 MDT	-3.9°	0.85°	1.4°	1.15	2.9 s
2	10:10 MDT	-3.9°	0.78°	1.3°	1.15	2.6 s

Figs. 5.6c,d, but at this time there was a region of calm air centered at $Z = 600$ m, coinciding to a significant deviation in measured wind direction. For $Z > 200$ m, the corrected profile of wind direction was consistent with the one measured at 8:30 MDT, excepting the region of calm air at $Z = 600$ m.

At the site measured by UAS 2, the corrected mean wind speed and direction profiles measured at 9:10 MDT and shown in Figs. 5.7a,b reflect a boundary layer undergoing transition, with evidence of turbulence for $Z < 500$ m. At 10:10 MDT, as shown in Figs. 5.7c,d, a multi-layer structure was also evident in the wind profiles in the form of significant changes in the wind direction throughout the profile. The horizontal wind speed was relatively consistent between 1 to 2 m/s for $Z < 800$ m, but there was evidence of stronger turbulence for $Z < 500$ m and moderate wind shear for $Z > 700$ m. As noted, the wind direction exhibited significant variation in the range $400 \text{ m} < Z < 500 \text{ m}$, with continual backing within $500 \text{ m} < Z < 900 \text{ m}$, and veering for $Z < 900 \text{ m}$. These different altitudes of behavior were consistent with the measured potential temperature changes (not included for conciseness), and became much easier to identify in the corrected profiles than they were before correction.

It is clear through comparison of the corrected and uncorrected profiles in Figs. 5.6 and 5.7 that the corrections reduce fluctuations about the mean profile under different

conditions and for different aircraft. Similar improvements have been observed for other profiles measured with these and other UASs. The coefficients determined by the optimization routine for these profiles are presented in Table 5.1. Comparing each flight by the same UAS demonstrates that the automated optimization converged on nearly identical coefficients for the same UAS with only one coefficient changing by more than 1° between each flight. Indeed, the correction coefficients were found to be remarkably similar for each UAS used throughout the LAPSE-RATE campaign. This similarity between the coefficients reinforces the assumption that the biases are caused by physical misalignment between the coordinate systems of the aircraft and five-hole probe. Note that bias corrected by Δt should not be expected to be consistent for the systems used here, as the time series of \vec{U}_m , \vec{U}_{ac} and $\vec{\Omega}$ are measured by separate acquisition systems at different rates and aligned using post-processing software. Thus the Δt bias is most likely introduced by errors in this alignment process and can be expected to be random.

5.3 Correction Procedure: Version 2

In addition to the error sources mentioned in Section 5.1.1, Drüe and Heinemann (2013) and Kalogiros and Wang (2002) suggested that additional bias could be introduced by the flow deformation caused by aircraft body, especially at high values of α and β . Usually, the in-lab calibration is carried out without the body of the UAS. Hence the calibration does not account for this bias. The first version of the correction procedure accounted for the effect of flow field deformation on the magnitude of the dynamic pressure but did not account for biases caused by the deformation on the

flow angles. Hence, we introduce a second version of the correction approach which includes these additional potential error sources in the correction approach where it is assumed that the α and β recovered from in-flight data are biased relative to the conditions in the laboratory such that

$$\alpha_{corr} = C_\alpha \alpha + \alpha_0 \quad (5.11)$$

$$\beta_{corr} = C_\beta \beta + \beta_0 \quad (5.12)$$

where α_{corr} and β_{corr} are the flow angles of the multi-hole probe relative to the free-stream when mounted on the UAS while α and β are the flow angles of the multi-hole probe assuming identical flow blockage conditions in flight and during laboratory calibration. On the other hand, C_α , α_0 , C_β and β_0 are correction coefficients found via an optimization procedure similar to that employed in Section 5.1.1. This is conducted following determination of $\Delta\epsilon$, followed by optimization to determine C_α and α_0 , then C_β and β_0 , which minimize the same cost functions described in Section 5.1.1.

5.3.1 Implementation and validation Version 2

With $\Delta\epsilon$, α_{corr} and β_{corr} known, the biases described by $\Delta\epsilon$ and the difference between the local and actual flow angles (α and β) can be removed. This is done by first using C_α , C_β , α_0 and β_0 to determine $\alpha_{corr}(t)$ and $\beta_{corr}(t)$ following Eqs. 5.11 and 5.12, then using these values in Eqs. 4.7. The rest of the correction procedure follows that described in Section 5.1.1 by which Eqs. 5.1 to 5.5 are applied to produce a final estimate of $[\vec{U}(t)]_I$.

This correction procedure was validated on data from a flight conducted in 2020 with a rectangular flight pattern to demonstrate the ability of the correction approaches to minimize the biases during significant changes in roll angle. The data was acquired using one five-hole probe on the same type of fixed-wing aircraft used for the validations presented above.

The different correction approaches are compared using the time series of recovered wind velocity and magnitude in Figure 5.8 which shows the uncorrected measurements, the measurements corrected using Version 1 of the correction, and the same measurements corrected using Version 2 of the correction. Similar to the discussion above, the correction coefficients were determined by applying the optimization routine to only the portion of the flight when the aircraft was established in the rectangular flight pattern.

It is clear through comparison of the corrected and uncorrected time series in Figure 5.8 that the additional correction of α and β , performs better than the first version in terms of reducing the sudden spikes in the velocity around the turns which can be seen when looking at the wind direction and the UAS direction (yaw angle) shown in Fig. 5.9. The V2 correction approach further reduces the bias caused by the change in the aircraft direction; for instance, see between 14:45 MDT and 14:52 MDT. The coefficients determined by the optimization routine for these profiles are presented in Table 5.2.

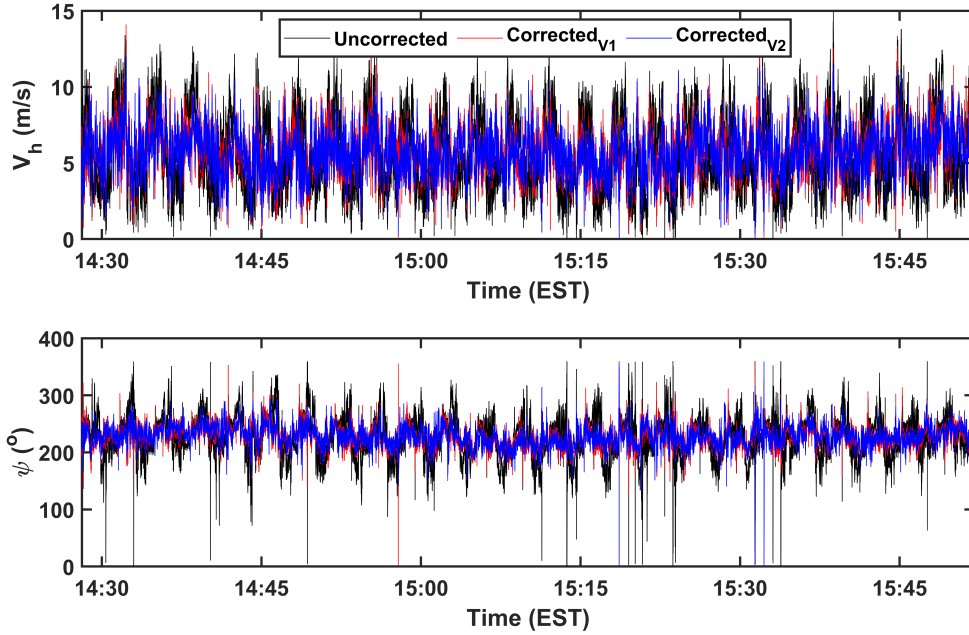


Figure 5.8 Comparison of (a) horizontal wind magnitude and (b) wind direction profiles with and without correction versions applied.

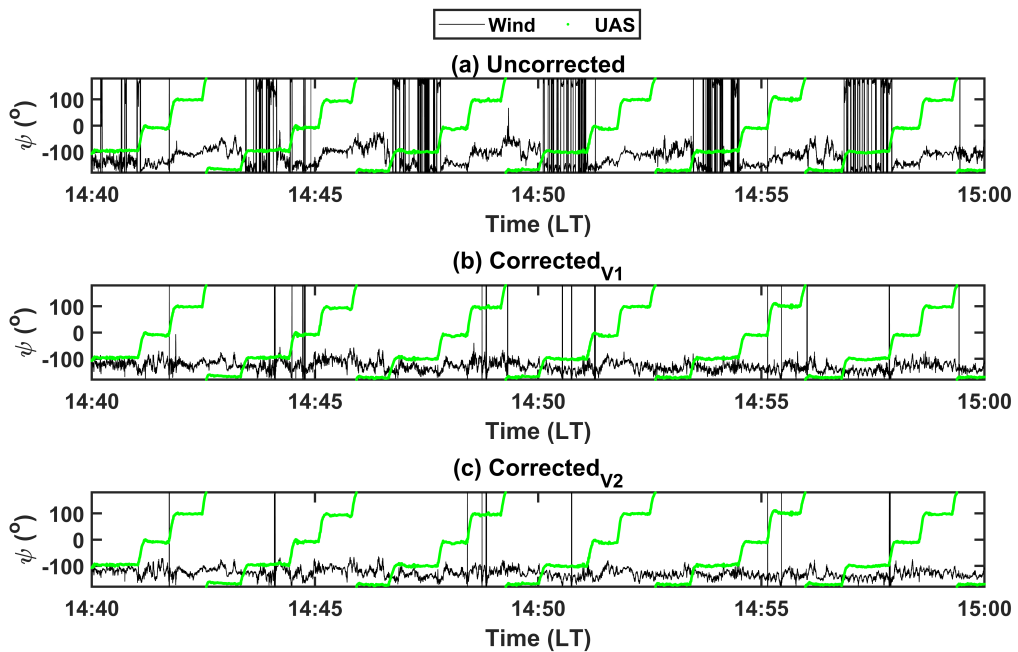


Figure 5.9 Comparison of wind direction and aircraft yaw direction (a) uncorrected, (b) corrected using V1, and (c) corrected using V2.

Table 5.2 Components of $\Delta\epsilon$ and the corrections coefficients of the flow angles determined by optimization.

Parameter	Value
$\Delta\theta$	-0.74°
$\Delta\phi$	-10.36°
$\Delta\gamma$	0.1°
ζ	1.35
Δt	1.21 s
C_α	-0.06
α_0	0.0011°
C_β	0.126
β_0	0.0032°

5.4 Summary

Multi-hole probe measurements are among the more common and reliable techniques used for the acquisition of wind velocity vector. However, when implemented on UAS there is significant potential to introduce bias due to the large ratio of aircraft velocity to wind velocity. Therefore, the measured wind velocities are very sensitive to these small biases. Furthermore, when conducting vertical profiles at a fixed location, these profiles typically require circular flight patterns which increase the probability of small misalignment between the probe and the aircraft axes introducing a time-dependent, periodic error in the wind velocity measurement that can propagate into post-flight analysis such as the calculation of energy spectra and Reynolds stresses.

An approach was presented that can be applied in post-processing of the flight data to automatically estimate the biases in axis misalignment, as well as errors in their alignment in time. Once estimated, these biases can be removed, improving the quality of the wind estimate.

These corrections were validated using data acquired as part of the LAPSE-RATE

field campaign. Measurements flown near a ground-based reference system revealed a significant reduction in measured oscillations of both wind magnitude and direction, which corresponded to the aircraft flight pattern. Additional verification was conducted by comparing profiles of wind speed and direction measured by two different aircraft at two different times. The estimated biases were within $\pm 1^\circ$ for each aircraft, and successful minimization of aircraft-induced oscillations in the measured profiles was observed for both aircraft. These results confirm that the biases are most likely due to physical misalignment of the aircraft and probe axes, as well as demonstrating that the same correction procedures can be applied to multiple aircraft.

Chapter 6 Coherent Structures Observation From Single Multi-Hole Probe Measurements

The experiments presented in this chapter employ the measurement approach presented in Chapters 4 and 5 to demonstrate the capability of UASs to resolve the surface-layer structure during the morning transition. For that purpose we simultaneously employ multiple fixed-wing UASs each equipped with single multi-hole probe for 3D wind measurements. The contents of this chapter are adapted from Al-Ghussain and Bailey (2022).

6.1 CLOUDMAP Campaign

These observations were conducted as part of the Collaboration Leading Operational Uncrewed Aerial System Development for Meteorology and Atmospheric Physics (CLOUDMAP) 2017 field campaign (Jacob et al., 2018) performed at the Oklahoma State University’s uncrewed aircraft flight station (UAFS) near Stillwater, Oklahoma (located at 36.162785° latitude, -96.8366762° longitude, and 288 m above sea level). The measurements presented here were collected on 27 and 28 June 2017, referred to as Case 1 and Case 2, respectively. Here, we will use local time (LT) when referencing the time of day, which was central daylight time (CDT) or UTC-5. For the cases being considered, sunrise was at 0613 LT with nautical twilight beginning at 0505 LT and civil twilight at 0543 LT.

The primary measurement systems used for this study consisted of three fixed-

wing UASs, used to conduct horizontal transects, with a fourth rotorcraft used to conduct vertical profiling. A sonic anemometer mounted on a 7-m tower along with three cup-and-vane anemometers and pressure, temperature, and humidity sensors were collocated with the vertical profiling site. The heights of the sonic anemometer and the three cup-and-vane anemometers were 8.2 m, 5.6 m, 4.5 m, and 3.4 m, respectively.

The three fixed-wing UASs were BLUECAT5 aircraft (for details see Witte et al., 2017; Bailey et al., 2019; Al-Ghussain and Bailey, 2021) flown simultaneously at three different heights, as illustrated in Fig. 6.1c. Each flight consisted of repeatedly traversing the same 1000 m long straight line transect at true air speed of 18 m s^{-1} and at constant altitude above sea level, resulting in approximately 15 m variability in aircraft above ground level (a.g.l.) as indicated in Fig. 6.1. Typically 40 to 50 transects were made per flight in alternating directions with each transect taking around 75 s. Measurements typically consisted of all three aircraft being flown for approximately 40 min of flight time, after which the aircraft were recovered, data downloaded, and batteries changed. Five flights were conducted for both Case 1 and Case 2, with Case 1 initiating measurements just after nautical sunrise at 0600 LT and measuring nearly continuously to 1130 LT with a fifth flight conducted at 1330 LT. Case 2 initiated measurements at 0600 LT with all five flights conducted before 1200 LT. For Case 1, the three aircraft were flown at nominal altitudes of 25 m, 50 m, and 75 m a.g.l. relative to takeoff ground level, whereas for Case 2, intermittent aircraft problems resulted in only the 50 m a.g.l. height being measured continuously, with additional measurements conducted at 25 m, 75 m, and 300 m depending on aircraft

availability.

The rotorcraft used was a 3DR SOLO aircraft (for details see Bailey et al., 2019) illustrated in Fig. 6.1c. The aircraft was flown simultaneously with the fixed wing aircraft and consisted of vertical ascents and descents at 2 m s^{-1} between 10 m and 100 m. Up to 10 ascent/descent combinations were flown in a single flight before the aircraft’s batteries required changing. Once the batteries were changed, the aircraft was returned to flight. Due to a shorter endurance, approximately four flights of the rotorcraft were conducted for each fixed-wing flight with times between flights depending on battery availability and charge rates. However, most flights were separated by less than 5 min.

Each aircraft was equipped with an iMet-XQ (InterMET Inc., Grand Rapids, Michigan, U.S.A.) capable of logging temperature (T), pressure (p), and relative humidity (RH) at a rate of 1 Hz. The fixed-wing aircraft measured three components of wind using a custom-built five-hole-probe logged at 200 Hz, but, due to viscous damping within the sensor tubing, was only capable of measuring frequency content lower than 60 Hz. To measure the winds, the rotorcraft was equipped with a Trisonica Mini 3D sonic anemometer (Anemoment LLC, Longmont, Colorado, U.S.A.) mounted on a 0.38 m mast to prevent distortion of the measured wind by the aircraft’s rotor wash. Although nominally it is a three-component anemometer, when operated in the configuration used here, only the horizontal components of wind are considered reliable. Additional details about the aircraft, sensing systems and data reduction procedures can be found in Witte et al. (2017) and Bailey et al. (2019) with an intercomparison and evaluation of system accuracy provided in Barbieri et al. (2019).

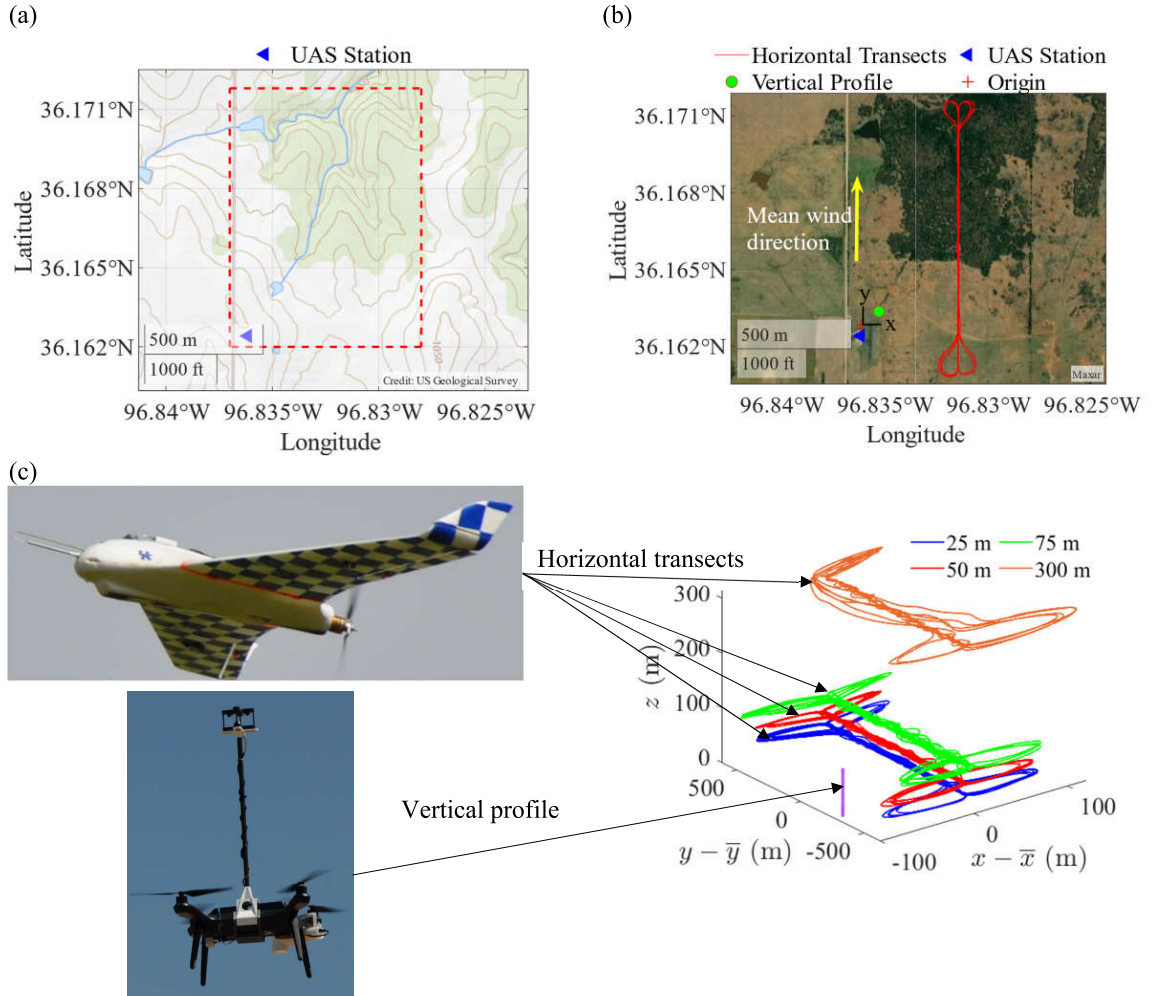


Figure 6.1 (a) Topographic map showing terrain surrounding measurement with (b) detailed satellite photograph of area highlighted by red box in (a). (c) shows the fixed-wing and rotorcraft UAS used, along with an additional illustration of the different flight path altitudes. Approximate location of flight trajectories and of fixed-wing UAS and measurement location of the rotorcraft indicated by red line and green dot respectively in (b). Contour lines in (a) correspond to 3.048 m elevation separation. From (Al-Ghussain and Bailey, 2022) and used with permission, license number 5513720396324.

The measured quantities are presented in an (x, y, z) coordinate system with the x -axis directed towards the east, the y -axis directed towards the north, and the z -axis directed up, and with the origin of the coordinate system located at the aircraft launch point (Fig. 6.1b). The wind velocity components (u, v, w) are aligned with the (x, y, z) axes, respectively.

6.2 Stability Conditions

To assess the surface-layer stability during the period of observation, the flux Richardson number

$$Ri = \frac{\frac{g}{T_v} \overline{w'\theta'_v}}{-u_\tau^3 \frac{\partial \bar{U}}{\partial z}} \quad (6.1)$$

was calculated from the sonic anemometer tower measurements. Here we use Reynolds averaging, e.g., $u(t) = \bar{u} + u'(t)$ where the overline indicates a 5 minute moving time average. Furthermore, virtual temperature is approximated as $T_v = T(1 + 0.61r_v)$ where r_v is the vapour mixing ratio and the virtual potential temperature is calculated from $\theta_v = T_v(100 \times 10^3/\bar{p})^{0.286}$. Moreover, the friction velocity was approximated using $u_\tau = (\overline{u'w'^2} + \overline{v'w'^2})^{1/4}$ and the horizontal wind velocity magnitude from $U = (u^2 + v^2)^{1/2}$. Finally, the velocity gradient was estimated by averaging the gradients measured between the cup and vane anemometers and sonic anemometer located on the tower. To minimize uncertainty caused by precision errors in the instruments propagating via the small separation between vertical measurement points, several approaches were evaluated. It was found that the approach that best minimized the impact of sensor precision error on the gradient calculations was to calculate the linear gradients between the different combinations of measurement heights of the cup and vane anemometers and sonic anemometer and average the result.

The resulting time evolution of Ri is presented in Fig. 6.2a. The figure shows slightly different behaviour for Case 1 than Case 2 with the results indicating more stable conditions existed for Case 1 than Case 2, although neither larger than the suggested critical Richardson number of 0.25 (Grachev et al., 2013). Hence, both

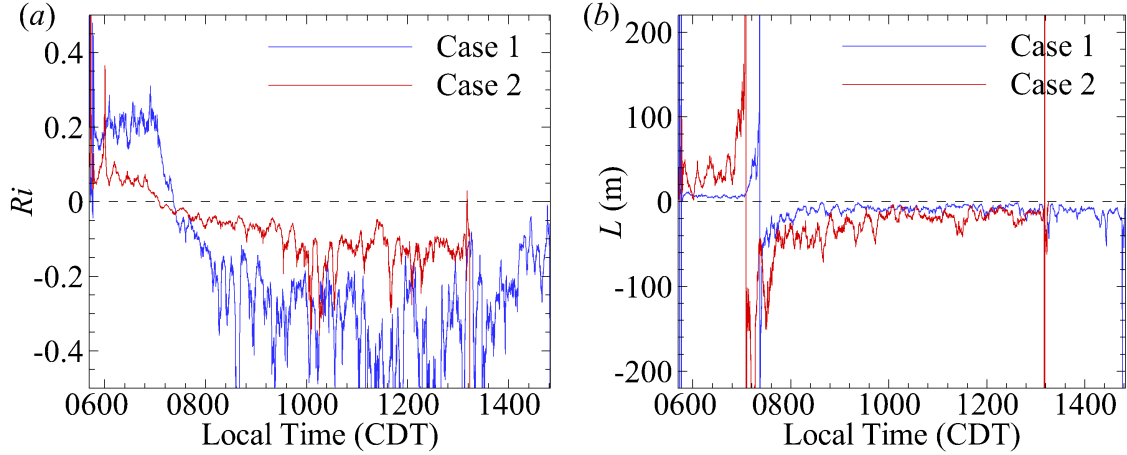


Figure 6.2 (a) Ri and (b) L calculated from the 7-m tower data for the duration of Case 1 and Case 2 observation periods. From (Al-Ghussain and Bailey, 2022) and used with permission, license number 5513720396324.

cases can be considered as dynamically unstable and prone to turbulence production. Figure 6.2a also indicates that the boundary layer transitioned to convective conditions slightly earlier for Case 2 than for Case 1, becoming negative at approximately 0720 LT whereas this transition occurred at 0740 LT for Case 1.

The corresponding Obukhov length scale (e.g., Leelóssy et al., 2014)

$$L = \frac{-u_\tau^3 \overline{T}_v}{\kappa g \overline{w' \theta'_v}} \quad (6.2)$$

is presented in Fig. 6.2b, where κ is the von Kármán constant and g is the gravitational acceleration. The results reflect the difference in Ri , with Case 2 showing a $|L| \sim 35$ m prior to transition, whereas Case 1 indicates $|L| \sim 5$ m for the same period. Following transition, for Case 1 $|L| \sim 10$ m whereas for Case 2 $|L| \sim 50$ m until 1000 LT, approaching $|L| \sim 10$ m for the latter portions of the morning.

6.3 Mean Properties of the Surface Layer

The difference between the values of the stability parameters for each case is reflected in the atmospheric properties measured at the UAS flight altitudes. To calculate statistics from the fixed-wing UAS, we considered only the portion of the flight when the UAS were in their automated flight pattern. As each flight consisted of several straight line transects, we then treated each transect as an individual sample. By assuming each transect occurs under steady state conditions, the averaged quantities are then spatially averaged over a nominal distance of 1000 m and with averages over individual transects indicated by $\langle \rangle$ brackets.

Figure 6.3a–b shows the evolution of $\langle \theta_v \rangle$ measured by the fixed-wing UAS for Case 1 (Fig. 6.3a) and Case 2 (Fig. 6.3b). The corresponding values of wind components $\langle u \rangle$ and $\langle v \rangle$ are shown in Fig. 6.3c–d. These figures show that the winds were generally from the south (positive v) for both cases with an increase in virtual potential air temperature at all measured altitudes after the inversion of Ri occurs. For Case 1 (Fig. 6.3a, c) there are measurable vertical gradients in both wind velocity and $\langle \theta_v \rangle$ prior to 0900 LT, with approximately uniform conditions measured after this time. Conversely, for Case 2, strong gradients are only evident in the mean wind velocity, whereas the $\langle \theta_v \rangle$ remains relatively homogeneous for all heights during the period of measurement.

These differences can be explained by the proportionate differences in stability conditions between the two cases. Figures 6.3e, f show the turbulence kinetic energy

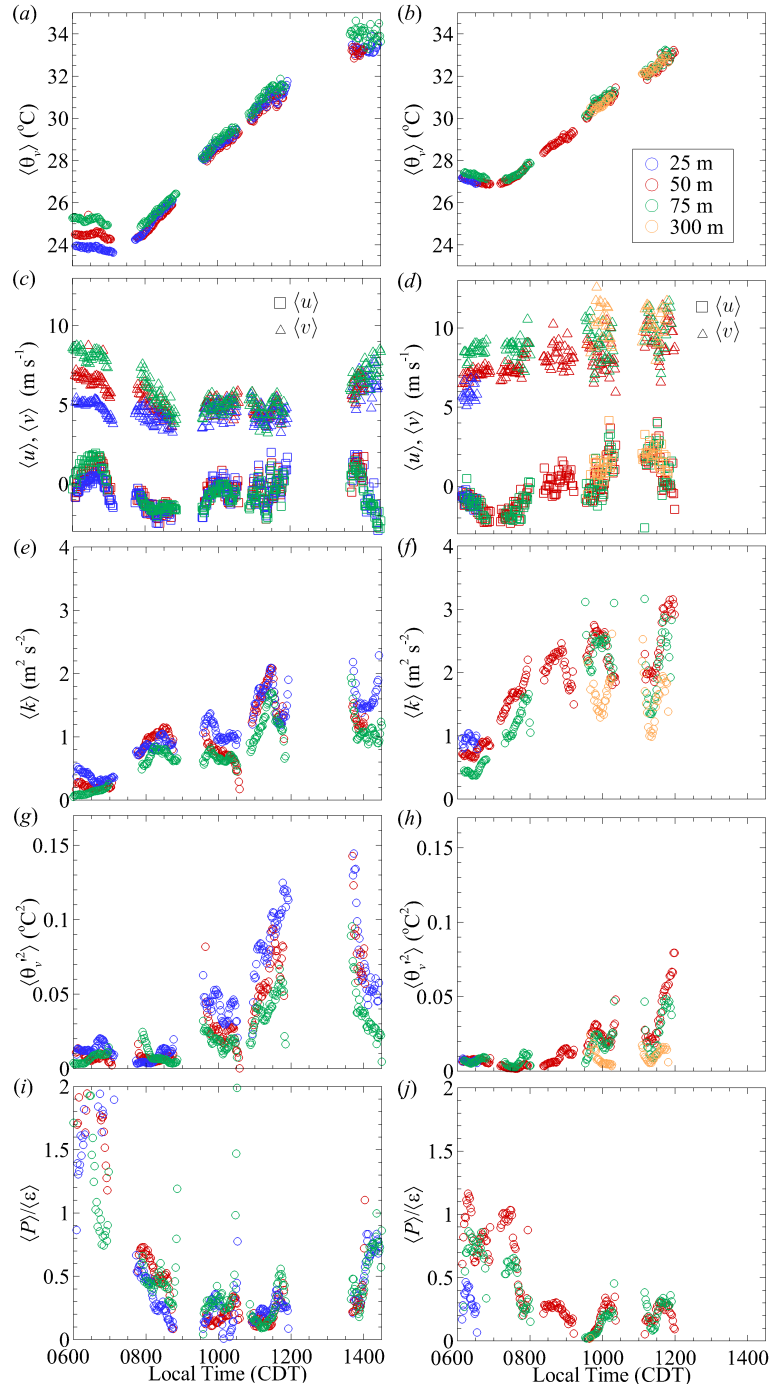


Figure 6.3 Time-dependence of: (a) $\langle \theta_v \rangle$ for Case 1; (b) $\langle \theta_v \rangle$ for Case 2; (c) $\langle u \rangle$ and $\langle v \rangle$ for Case 1; (d) $\langle u \rangle$ and $\langle v \rangle$ for Case 2; (e) $\langle k \rangle$ for Case 1; (f) $\langle k \rangle$ for Case 2; (g) $\langle \theta_v'^2 \rangle$ for Case 1; (h) $\langle \theta_v'^2 \rangle$ for Case 2; (i) $\langle P \rangle / \langle \epsilon \rangle$ for Case 1; and (j) $\langle P \rangle / \langle \epsilon \rangle$ for Case 2. Blue symbols indicate measurements made at $z = 25$ m, red symbols indicate measurements made at $z = 50$ m, green symbols indicate measurements made at $z = 75$ m, and orange symbols indicate measurements made at $z = 300$ m. From (Al-Ghussain and Bailey, 2022) and used with permission, license number 5513720396324.

for Case 1 and Case 2, respectively, calculated using

$$\langle k \rangle = \frac{1}{2} (\langle u'^2 \rangle + \langle v'^2 \rangle + \langle w'^2 \rangle). \quad (6.3)$$

Comparison of the two cases shows higher magnitude of $\langle k \rangle$ for Case 2 during the period of positive Ri , reflecting an increase in mechanical production of turbulence. Notably, both cases show higher values of $\langle k \rangle$ near the surface for this period as well. As the morning progresses, the general trend was for $\langle k \rangle$ to increase, with Case 2 continuing to show higher magnitudes, but with both cases also showing increasing variability in $\langle k \rangle$. The latter behaviour suggests two interpretations: increasing contribution to turbulence kinetic energy from spatial scales larger than 1000 m [e.g., larger than that of a representative thermal which usually has a radius of less than 600 m, (Romps and Charn, 2015; Hernandez-Deckers and Sherwood, 2016)]; or horizontal advection of turbulent air from other locations. Neither of these explanations are mutually exclusive, as large-scale coherent motions would be expected to advect turbulence and other atmospheric properties over commensurate spatial scales (Willmarth and Lu, 1972; Blackwelder and Kaplan, 1976; Robinson, 1991).

Similar behaviour is observed for $\langle \theta_v'^2 \rangle$, which describes the temperature and density fluctuations in the atmospheric surface layer and is shown in Fig. 6.3g, h for Case 1 and Case 2, respectively. These results show an increase in the temperature fluctuations for both cases, but with Case 1 showing an earlier and larger increase. Both cases exhibited unsteadiness in $\langle \theta_v'^2 \rangle$ having the same time scale (nominally one hour) as observed for the unsteadiness in $\langle k \rangle$.

Greater insight into the source of these fluctuations could be found by examination

of the temporal evolution of the turbulence kinetic energy budget terms for both cases. Note that it was found that the sample rate of p , T and RH varied around the 1 Hz nominal rate throughout the flight, and therefore it was not possible to accurately align (u, v, w) and T in time (as they were logged separately and aligned in post-processing). This prohibited the calculation of $\langle w'\theta'_v \rangle$ at length scales smaller than approximately 20 m and, in turn, provide accurate estimation of the buoyant production. However, an estimate of mechanical production can be made using

$$\langle P \rangle = (\langle u'w' \rangle^2 + \langle v'w' \rangle^2)^{1/2} \frac{\partial \bar{U}}{\partial z}, \quad (6.4)$$

by assuming negligible horizontal gradients in \bar{U} . Note that due to the scatter in the $\langle u \rangle$ and $\langle v \rangle$ results, the gradient of \bar{U} was calculated from the rotorcraft measurements during each 10 min. flight. This was done by first averaging the measured value of U over 5-min intervals and then fitting the curve $\bar{U} = A \log(z)^2 + B \log(z) + C$ to the resulting profile, thus producing smooth estimates of $\partial \bar{U} / \partial z$. In addition, an estimate of the dissipation rate, $\langle \varepsilon \rangle$, was made from the wavenumber spectrum, $\Phi(2\pi/\lambda)$, measured for each transect, where λ is wavelength. To do so, the mean dissipation rate for each transect was calculated from the spectrum using

$$\langle \varepsilon \rangle = \left(\frac{\Phi}{0.49(2\pi/\lambda)^{-5/3}} \right)^{3/2}. \quad (6.5)$$

Details of this calculation procedure can be found in Bailey et al. (2019).

The resulting time-dependent ratio $\langle P \rangle / \langle \varepsilon \rangle$ is presented in Fig. 6.3i, j for Case 1 and Case 2. If, for the sake of simplicity, one assumes negligible turbulence advection, that $\partial \langle k \rangle / \partial t \approx 0$ (i.e., the turbulence kinetic energy is quasi-stationary, Nilsson et al., 2016) and that pressure fluctuations can be neglected, it is possible to interpret

Fig. 6.3i, j as an estimate of the relative contribution of mechanical production to total production. Note that these assumptions are not likely to be completely satisfied, however, as reflected in the strong time-dependence of Fig. 6.3e, f. Both cases show mechanical production equating or exceeding dissipation at the start of the observation period, with Case 1 indicating mechanical production exceeding dissipation near the surface due to low measured dissipation rates. For the remainder of the observation period, however, the trend in $\langle P \rangle / \langle \varepsilon \rangle$ is very similar for both cases. Notably, the mechanical production remains the primary means of turbulent production until ~ 0830 LT.

6.4 Visualization of Flow Structure

Having established the background statistical description of the surface-layer properties, in this section we examine the large-scale structure of the turbulence as revealed through the fluctuation fields $\theta'_v(t, x, y, z)$ and $U'(t, x, y, z)$. We first look at the time height plots of $\theta'_v(t, z) = \theta_v(t, z) - \langle \theta_v(t, z) \rangle$ where θ_v is the virtual potential temperature measured by the rotorcraft and $\langle \rangle$ in this context is used to indicate an average in both t and z , with the time averaging being applied over the duration of each 10 min flight.

Isocontours of $\theta'_v(t, z)$ are presented in Fig. 6.4a, b for Case 1 and Fig. 6.4c, d for Case 2. These isocontours reveal strong vertical stratification of θ_v before 0800 LT for Case 1, reflecting the stable conditions observed in Fig. 6.2. As the morning progresses, the stratification decays, with moderate temperature variability observed from 0800 LT to 0900 LT. After 0900 LT, the θ'_v perturbations organize into

intermittent, vertically oriented structures. These structures have varying time scales roughly on the order of 2 min and, assuming advection velocity of 5 m s^{-1} (Fig. 6.3c) are consistent with turbulent thermals having horizontal length scales on the order of 500 m. Similar behaviour is observed for Case 2, shown in Fig. 6.4c, d, except that the stable stratification in the early morning hours is weaker and consequently more unsteadiness can be observed in the temperature field. Once convective conditions develop after 0930 LT, the behaviour is very similar to that of Case 1.

As could be expected, isocontours of $U'(t, z)$, presented in Fig. 6.5a, b for Case 1 and Fig. 6.5c, d for Case 2, demonstrated virtually identical time-dependence as that of $\theta'_v(t, z)$. Although a clear velocity gradient is evident for Case 1 prior to 0830 LT, due to the reduced thermal stratification for Case 2 the velocity perturbations show increased variability in both time and space, reflected in the differences in $\langle k \rangle$ between the two cases as observed in Fig. 6.3e, f. Once the thermals develop, a qualitative observation can be made that the negative velocity perturbations are coincident with positive temperature perturbations and vice versa, providing confidence that the contours in Figs. 6.4 and 6.5 are visualizations of large-scale mixing events.

Similar visualizations can be produced from the fixed-wing UAS measurements. However, for these flights the visualizations are in the form of isocontours of $\theta'_v(t, y)$ and $U'(t, y)$ which are provided in Fig. 6.6 for $z = 50 \text{ m}$ for Case 1. As shown in Fig. 6.6a–b, the fluctuations in θ'_v and U' are initially above the mean value for $y > 500 \text{ m}$ and below the mean value for $y < 500 \text{ m}$ prior to 0700 LT. This behaviour is consistent with topographically induced internal layer formation as it is similar to the observations made from field experiments (Gao et al., 1989; Lu and Fitzjarrald, 1994;

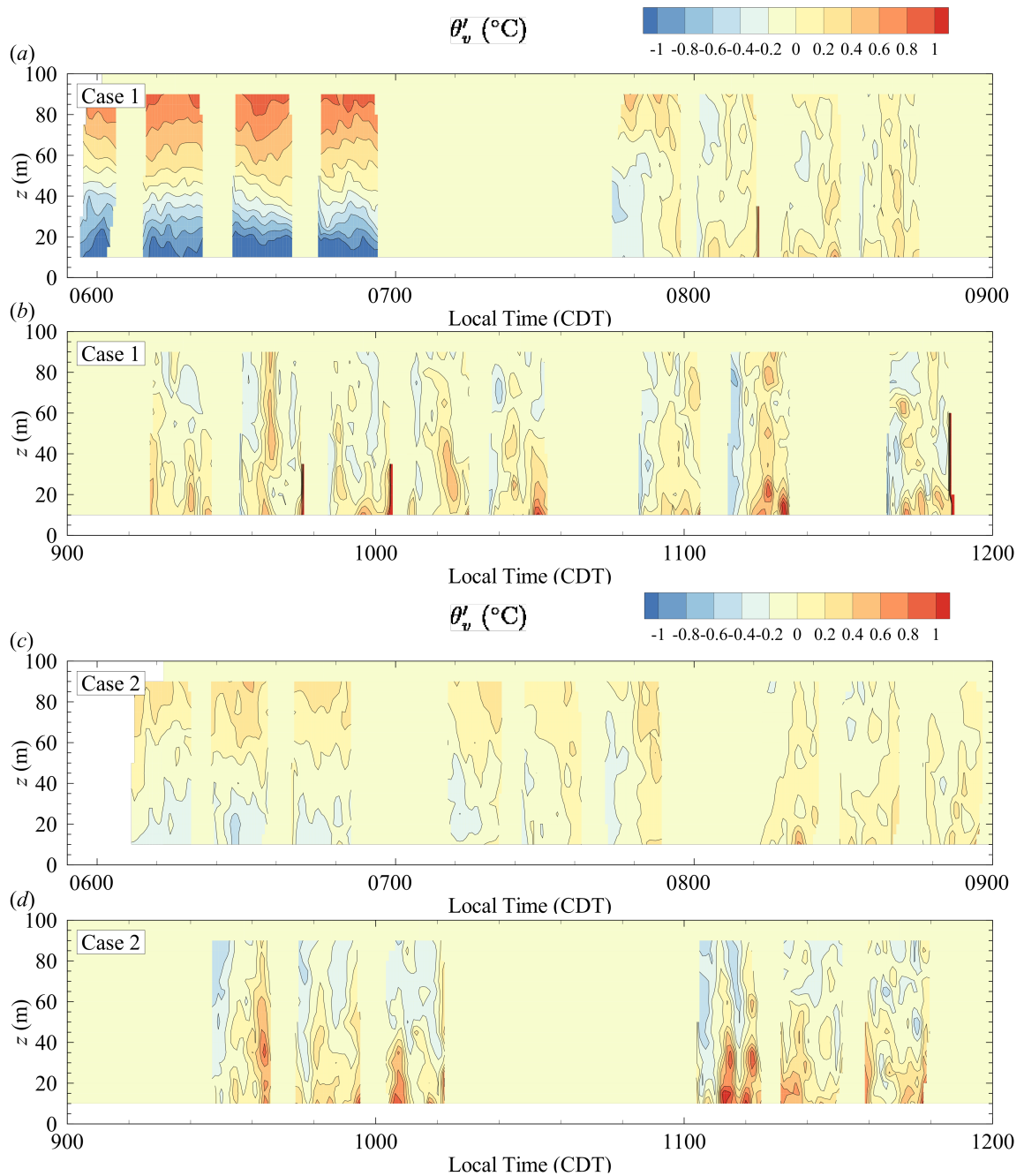


Figure 6.4 Isocontours of $\theta'_v(t, z)$ measured by rotorcraft UAS for: (a) 0600 LT to 0900 LT and (b) 0900 LT to 1200 LT for Case 1 and (c) 0600 LT to 0900 LT and (d) 0900 LT to 1200 LT for Case 2. From (Al-Ghussain and Bailey, 2022) and used with permission, license number 5513720396324.

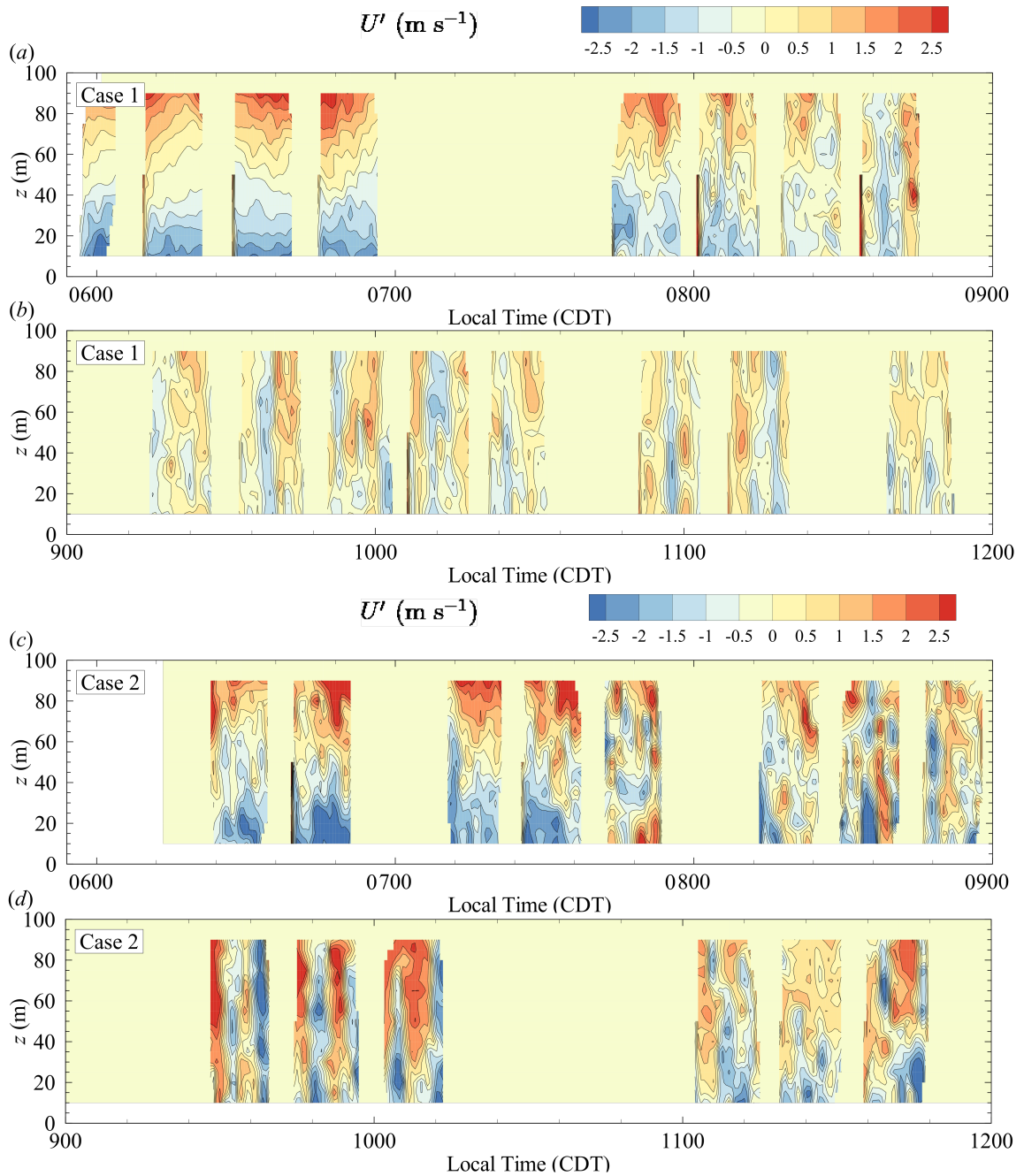


Figure 6.5 Isocontours of $U'(t, z)$ measured by rotorcraft UAS for: (a) 0600 LT to 0900 LT and (b) 0900 LT to 1200 LT for Case 1 and (c) 0600 LT to 0900 LT and (d) 0900 LT to 1200 LT for Case 2. From (Al-Ghussain and Bailey, 2022) and used with permission, license number 5513720396324.

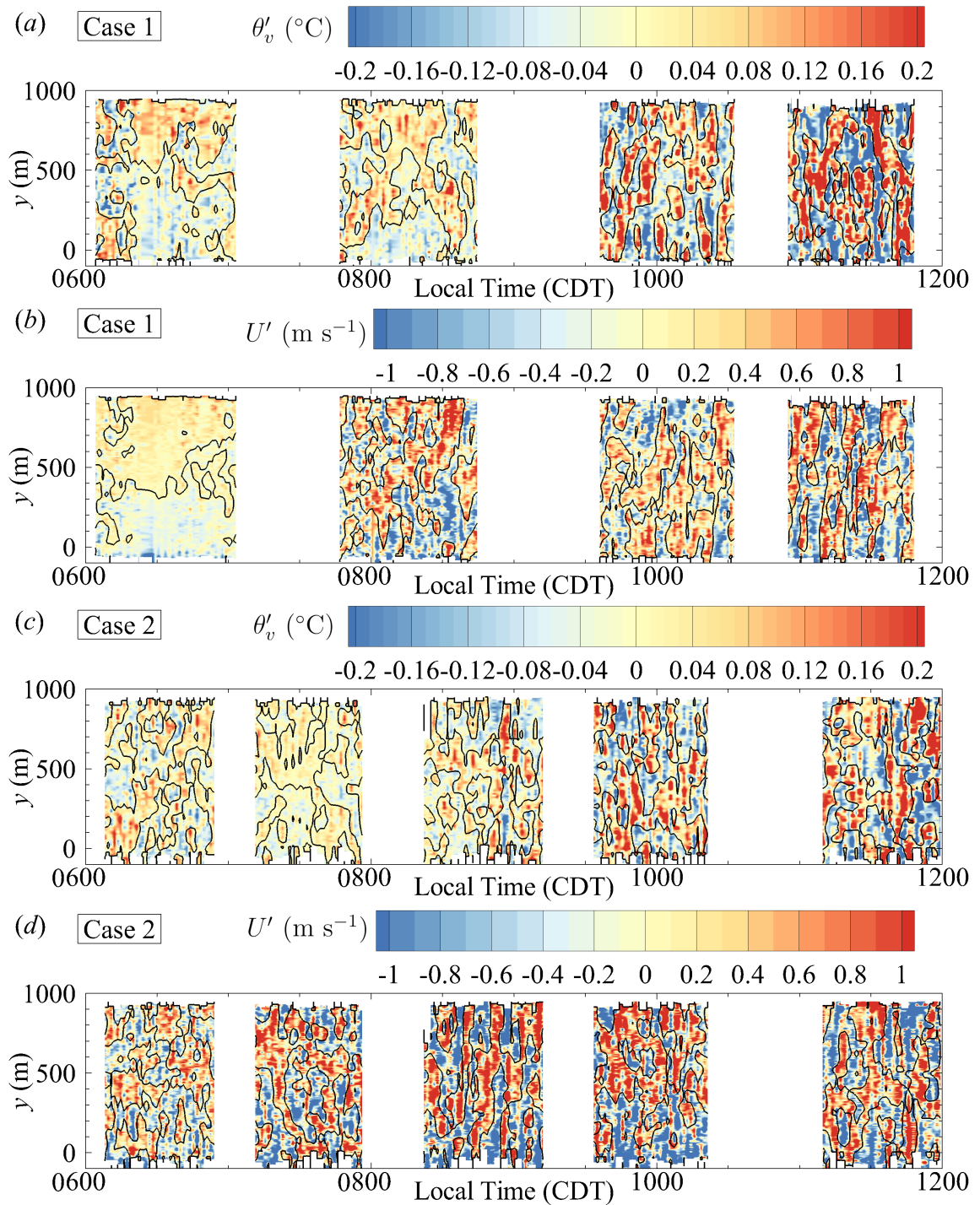


Figure 6.6 Isocontours of (a) $\theta'_v(t, y)$ measured by fixed-wing UAS flying at $z = 50$ m for Case 1 with corresponding isocontours of $U'(t, y)$ shown in (b). Case 2 isocontours of $\theta'_v(t, y)$ and $U'(t, y)$ at $z = 50$ m shown in (c) and (d), respectively. The black line on the figures indicates the zero-level contour line for same data after low-pass filtering at $y \sim 200$ m in space and $t \sim 180$ s in time. From (Al-Ghussain and Bailey, 2022) and used with permission, license number 5513720396324.

Alcayaga et al., 2020) and LES (Perret and Patton, 2021) studies examining the effect of forest and vegetation on the flow field. Note also that the aircraft was flying over a transition from pasture to trees for $y \gtrsim 300$ m (Fig. 6.1b), producing a likely source of local perturbation from the mean flow. After 0800 LT, the fluctuations appear more stochastic, taking the form of increasingly smaller-scale motions with the convective conditions after 1000 LT characterized by motions having length scales on the order of $y \sim 300$ m. The same organization appears in both temperature and velocity perturbations and is consistent with the formation of turbulent thermals observed in Figs. 6.4 and 6.5. For Case 2, which had higher values of $\langle k \rangle$ and lower stability in the early morning, the positive Ri period is characterized by large-scale perturbations, on the order of $y \sim 500$ m, which break into smaller scale thermal-associated events after inversion of Ri .

6.5 Temperature and Velocity Correlations

Of particular interest in Fig. 6.6, is qualitative evidence of organization over long time periods (nominally 20 min), suggesting structural organization at time scales longer than each transect. To educe these motions, velocity and temperature correlations were conducted noting that the existence of non-zero trends in the autocorrelation indicates organized motions, i.e., coherent structures (Harun and Reda Lotfy, 2019). To investigate this larger-scale organization, we treat each transect as an independent realization. We first let i be an integer value indicating transect number. We then consider two variables of interest measured in the direction of the transect, y , e.g.,

$\xi(y, i)$ and $\zeta(y, i)$. The cross-correlation of ξ and ζ then could be found using

$$R_{\xi\zeta}(\Delta y, \Delta i) = \left\langle \frac{\xi'(y, i)}{\langle \xi'(y, i)^2 \rangle^{1/2}} \frac{\zeta'(y + \Delta y, i + \Delta i)}{\langle \zeta'(y + \Delta y, i + \Delta i)^2 \rangle^{1/2}} \right\rangle, \quad (6.6)$$

where the $\langle \rangle$ brackets again indicate an average of values measured along the transect path. Furthermore, $R_{\xi\xi}(\Delta y, \Delta i)$ is an autocorrelation. Each transect i was correlated with neighboring transects in the available range of Δi and ensemble-averaging applied across all i to produce an averaged correlation for the entire flight, $\langle\langle R_{\xi\zeta}(\Delta y, \Delta i) \rangle\rangle$, a process which was implemented to improve the statistical convergence of the correlations. Here, $\langle\langle \rangle\rangle$ indicates an average over the entire flight as opposed to an individual transect. To convert the transect separation Δi into a time displacement, Δt , we multiply by the average temporal duration of each transect for that flight.

As could be expected from Fig. 6.6, the most correlated motions were for scales smaller than the transect length due to turbulent motions smaller than ~ 500 m in spatial scale. To examine temporal and altitude trends of these motions, autocorrelations of U , $\langle\langle R_{UU}(\Delta y, 0) \rangle\rangle$, are presented in Fig. 6.7.

Figure. 6.7a, b compares the time-dependence of $\langle\langle R_{UU}(\Delta y, 0) \rangle\rangle$ measured at $z = 50$ m, for Case 1 and Case 2 respectively. For Case 1 (Fig. 6.7a), which had higher $|Ri|$ due to reduced horizontal wind velocity, there is a noticeable trend in time consisting of a broadening of the correlations in time despite the decorrelation scale (the Δy value where $\langle\langle R_{UU} \rangle\rangle \rightarrow 0$) being nearly constant for all cases where $Ri < 0$. Note that the broadening of $\langle\langle R_{UU} \rangle\rangle$ at low correlation values for the 0600 LT to 0700 LT measurement period is consistent with a weak correlation influenced by

a broad background trend, as could be expected from the topographic influence observed in the visualizations of Fig. 6.6b. The gradual broadening of the correlations between 0700 LT and 1200 LT is also consistent with the decrease in Ri and reflects the development and growth of turbulent thermals observed in Fig. 6.5a, b and Fig. 6.6b, c. Conversely, the lower $|Ri|$ for Case 2 shows a step change in behaviour with stable and transitional Ri conditions having a similar structure with decorrelation scale of $\Delta y \approx 150$ m and unstable conditions having a similar, but slightly broader correlation with decorrelation scale of $\Delta y \approx 250$ m. The increased scales relative to Case 1 reflect the increased importance of mechanical turbulence for this case, with the more rapid transition in correlation similar to the more rapid increase in $\langle k \rangle$ shown in Fig. 6.3f and more rapid change in $\langle P \rangle / \langle \varepsilon \rangle$ shown in Fig. 6.3j.

Figure. 6.7c, d compares $\langle \langle R_{UU}(\Delta y, 0) \rangle \rangle$ measured at different altitudes between 0600 LT and 0700 LT for Case 1 and Case 2, respectively. There is a distinct difference in behaviour for the two cases, with the more stable Case 1 showing an increase in correlation with altitude similar to the behaviour reported in Alcaayaga et al. (2020), with Case 2 being nearly constant with altitude. Although the increase with altitude in Case 1 could be attributed to difference in advection velocity with altitude, similar velocity gradients were present for Case 2 (Fig. 6.3c, d), suggesting that the difference between Fig. 6.7c, d reflects an altitude dependence in turbulent scales for Case 1 that is not present in Case 2. Such altitude dependence in Case 1 is consistent with a z -dependent mixing length. Such z -dependent mixing length has been reported and investigated previously in the literature (Deardorff, 1980; Honnert et al., 2021). However, the reduced altitude dependence observed for Case 2 indicates the presence

of large eddies which span the depth of the surface layer and potentially a boundary-layer-thickness-dependent, large-scale mixing length which coincides with what was reported by Honnert et al. (2021).

A similar comparison of $\langle\langle R_{UU}(\Delta y, 0) \rangle\rangle$ is made for the 1100 LT to 1200 LT time period in Fig. 6.7e, f. These correlations confirm that similar layer-spanning structures exist for both cases once convective conditions set in, consistent with the visualizations shown in Fig. 6.5. Furthermore, Case 2 shows that similar structure persists at least up to $z = 300$ m, the highest altitude measured during these observations.

To better extract the spatio-temporal organization of the velocity and temperature fields, we can examine the presence of correlated wind perturbations in contours of $\langle\langle R_{UU}(\Delta y, \Delta t) \rangle\rangle$ as provided for Case 1 in Fig. 6.8a–d. Note that autocorrelations such as these will be anti-symmetric in time so only the positive time displacements are shown. For the 0600 LT to 0700 LT period (Fig. 6.8a) there is a peak in correlation at $\Delta y = 0$ for all Δt . The persistence of these weakly correlated regions at large Δt suggest the presence of large-scale persistent structure with the Δy extent of these correlations can be considered a representative scale of the motions.

The consistent peak at $\Delta y = 0$ for the 0600 LT to 0700 LT period reflects a condition where the same flow features are being measured across each transect, which here can be attributed to time-independent flow features produced by topographic effects (Fig. 6.6b). This spatially consistent structure is still present in the correlations measured from 0800 LT to 0845 LT (Fig. 6.8b), however now the level of correlation is much weaker, reflecting a breakup of the topographically induced motions.

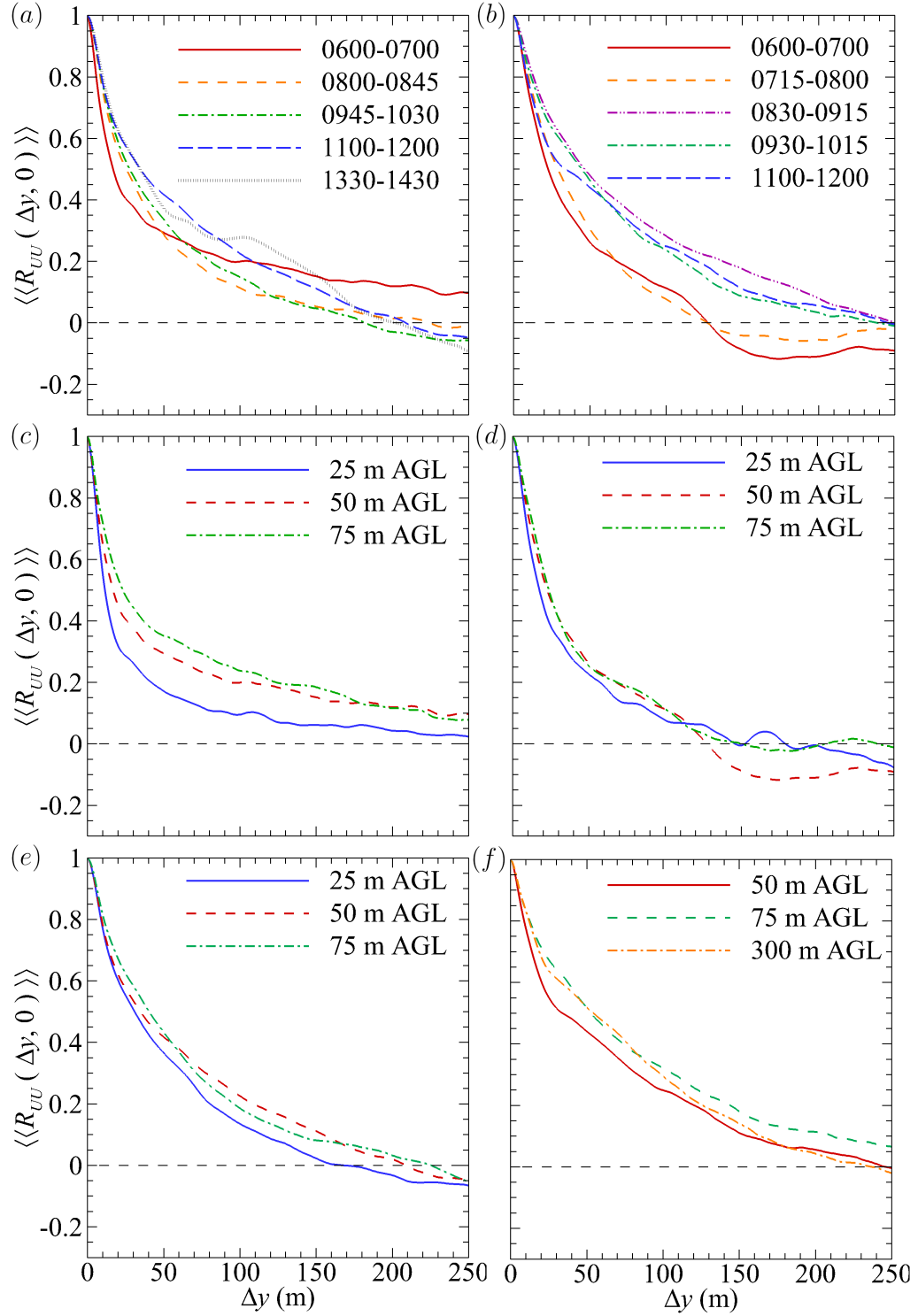


Figure 6.7 Autocorrelations $\langle\langle R_{UU}(\Delta y, 0) \rangle\rangle$ measured at $z = 50$ m for (a) Case 1 and (b) Case 2 at different times. $\langle\langle R_{UU}(\Delta y, 0) \rangle\rangle$ measured between 0600 LT to 0700 LT at different altitudes for shown in (c) for Case 1 and and (d) for Case 2. $\langle\langle R_{UU}(\Delta y, 0) \rangle\rangle$ measured from 1100 LT to 1200 LT at different altitudes shown in (e) for Case 1 and (f) for Case 2. From (Al-Ghussain and Bailey, 2022) and used with permission, license number 5513720396324.

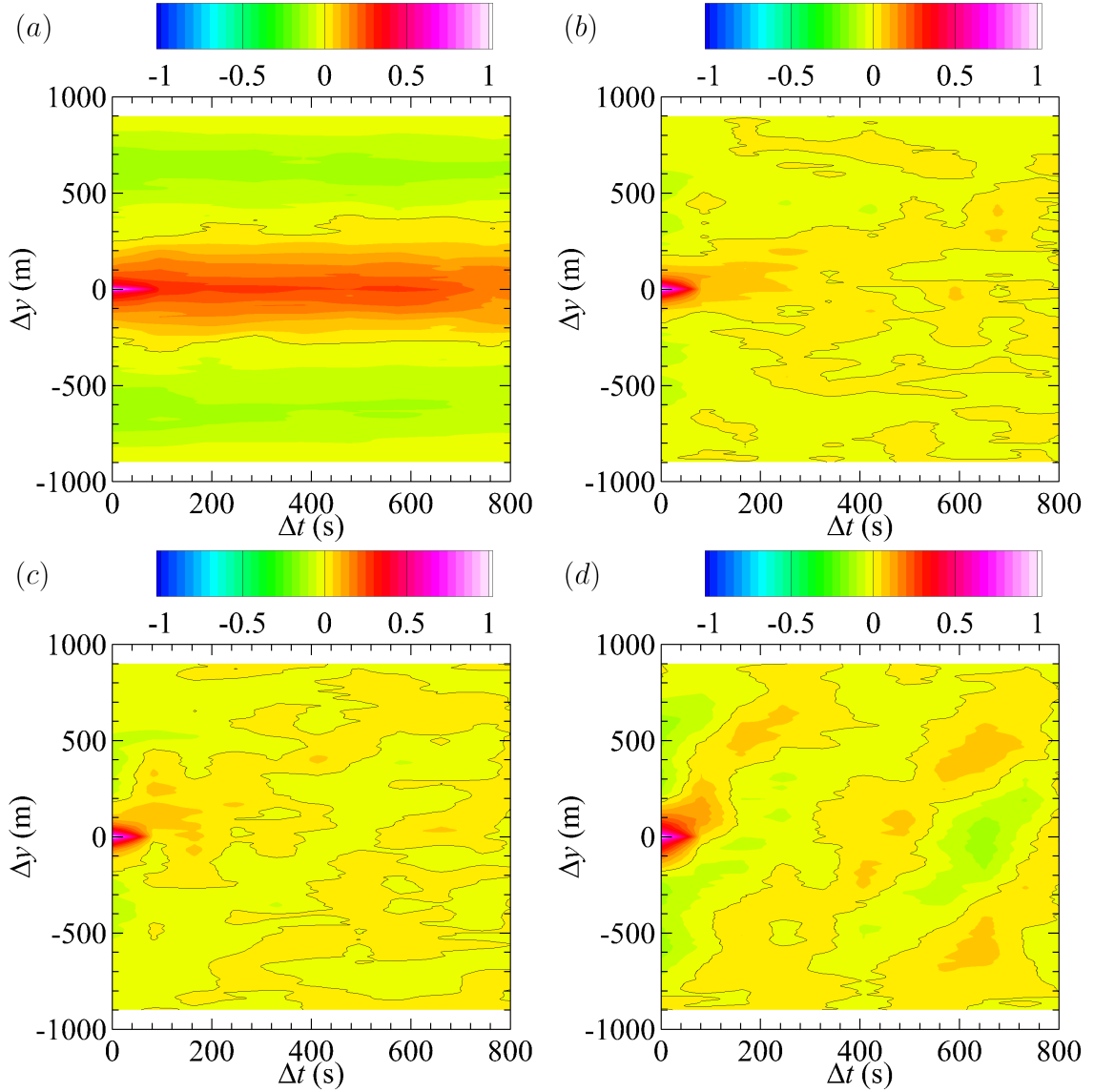


Figure 6.8 Contours indicating magnitude of $\langle\langle R_{UU}(\Delta y, \Delta t) \rangle\rangle$ using observations made during Case 1 at $z = 50$ m from (a) 0600 LT to 0700 LT; (b) 0800 LT to 0845 LT; (c) 0945 LT to 10300 LT; and (d) 1100 LT to 1200 LT. Solid lines indicate where $\langle\langle R_{UU} \rangle\rangle = 0$. From (Al-Ghussain and Bailey, 2022) and used with permission, license number 5513720396324.

Interestingly, from 0800 LT to 0845 LT (Fig. 6.8b) spatial periodicity becomes evident. Moreover, as the morning progresses (Fig. 6.8c, d) these positively correlated regions are flanked by anti-correlated regions, a feature consistent with correlations connected to VLSMs/superstructures (see Hutchins and Marusic, 2007; Monty et al., 2007, for example).

In the correlations from 0800 LT to 0845 LT there is some evidence of time-dependence in the correlated features, appearing as a tilt in the isocontours. This time-dependence represents a relatively slow advection in the y direction with $\Delta y/\Delta t \approx 0.5 \text{ m s}^{-1}$, or about 10% of the the corresponding value of $\langle v \rangle$. The time-dependence increases as the surface layer becomes more unstable as shown in Fig. 6.8c, d. However, this time-dependence still suggests advection speeds of the structures much slower than the mean velocity, approximately 20% and 50% for the 1100 LT to 1200 LT and 1330 LT to 1430 LT measurements, respectively. Similar time-dependence in the correlations was observed for the other measurement altitudes.

Similar structure and scales were observed in the temperature correlations, as illustrated in the corresponding $\langle\langle R_{\theta_v\theta_v}(\Delta y, \Delta t)\rangle\rangle$ fields shown in Fig. 6.9a–d. Specifically, an increase in the time-dependence of the $\langle\langle R_{\theta_v\theta_v}(\Delta y, \Delta t)\rangle\rangle$ field can be observed, which increasingly tilts relative to horizontal ($\Delta y = 0$) axis as the surface layer transitions through neutral to convective conditions. Interestingly, for the 0800 LT to 0845 LT case (Fig. 6.9b) there is less evidence of long-time-scale advection although some small-scale correlated features appear which have $\Delta y/\Delta t$ on the order of 50% of the mean velocity.

There are some interesting implications of this observation of varying advection

velocity with time and surface layer stability. It should be noted that, due to the measurements being conducted as a transect rather than over a spatial plane, we cannot rule out that these measurements reflect the presence of long advected structures, which are being bisected by the aircraft. In such a case, the time-dependence of the advection velocity could represent a change in the angle of the structure with respect to the transect direction (assuming it advects with the mean velocity), rather than a change in advection velocity. Alternatively, this change in advection velocity could reflect changes in the physical process of structure formation, with the more stable conditions producing structures that are evolving more slowly and dependent on surface features which produce them. Regardless, the result confirms for this type of flow that the application of Taylor’s frozen-flow hypothesis to reconstruct the spatial structure of large-scale flow features could confound interpretation, as reviewed by Moin (2009) and many others for canonical wall-bounded flow.

To confirm that these coherent motions play an important role in the turbulent transport of momentum and heat (as previously reported in Gao et al., 1989; Lu and Fitzjarrald, 1994; Drobinski et al., 2004; Feigenwinter and Vogt, 2005; Barthlott et al., 2007, for example) we look at the the cross-correlation fields of $\langle\langle R_{u^*w}(\Delta y, \Delta t)\rangle\rangle$ and $\langle\langle R_{w\theta_v}(\Delta y, \Delta t)\rangle\rangle$. Here, to all we’ve introduced a mean-flow aligned coordinate system (x^*, y^*, z) and (u^*, v^*, w) whereby the coordinate system has been rotated to align x^* with the mean wind vector. Examples of these cross-correlation fields are shown in Fig. 6.10 and reveal the same general structure as observed in the $\langle\langle R_{UU}(\Delta y, \Delta t)\rangle\rangle$ and $\langle\langle R_{\theta_v\theta_v}(\Delta y, \Delta t)\rangle\rangle$ autocorrelation fields. Specifically, the time-dependence of the isocontours, reflecting the same $\Delta y/\Delta t$ dependence observed in

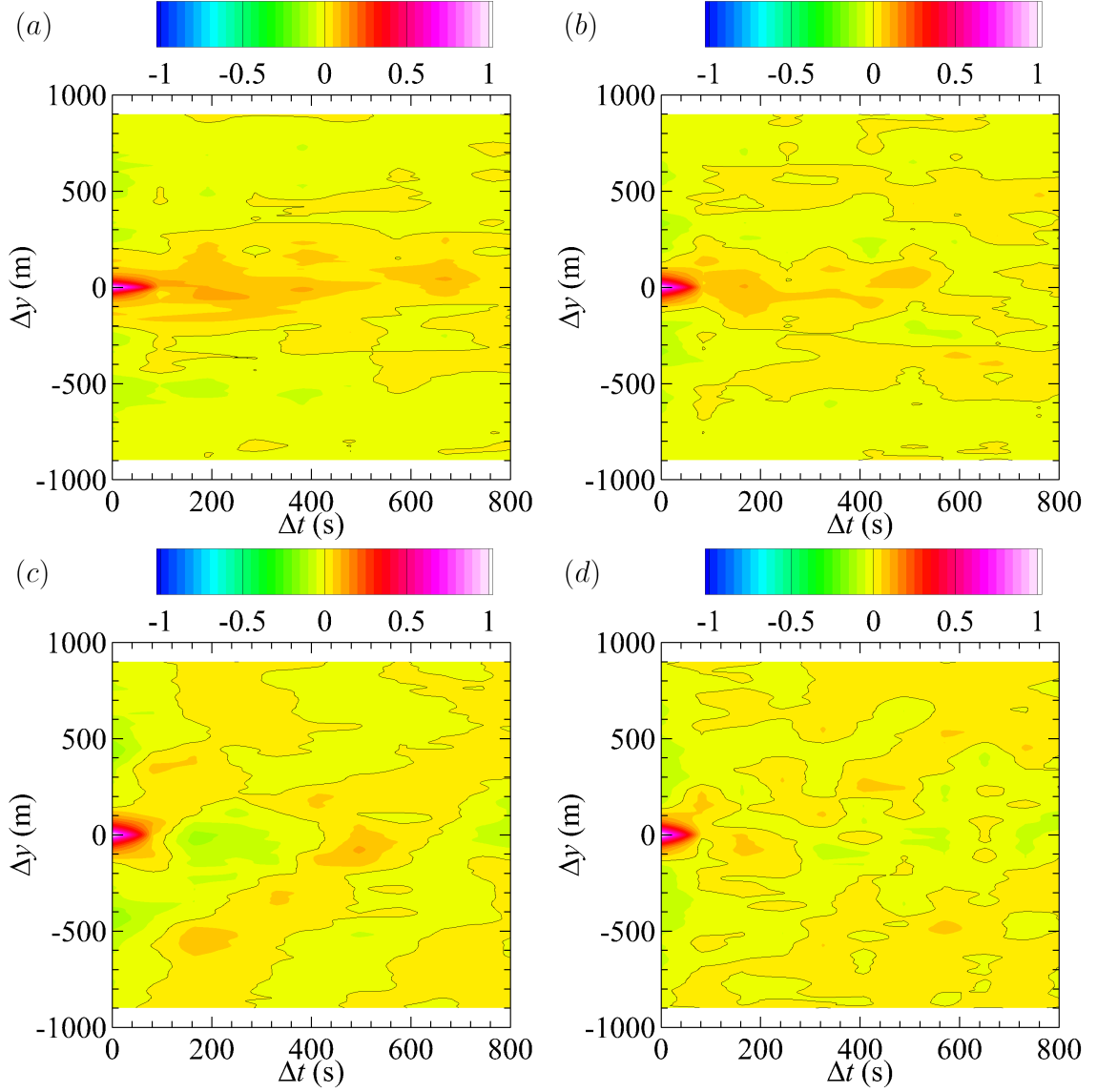


Figure 6.9 Contours indicating magnitude of $\langle\langle R_{\theta_v\theta_v}(\Delta y, \Delta t) \rangle\rangle$ using observations made during Case 1 at $z = 50$ m from (a) 0600 LT to 0700 LT; (b) 0800 LT to 0845 LT; (c) 0945 LT to 1030 LT; and (d) 1100 LT to 1200 LT. Solid lines indicate where $\langle\langle R_{\theta_v\theta_v} \rangle\rangle = 0$. From (Al-Ghussain and Bailey, 2022) and used with permission, license number 5513720396324.

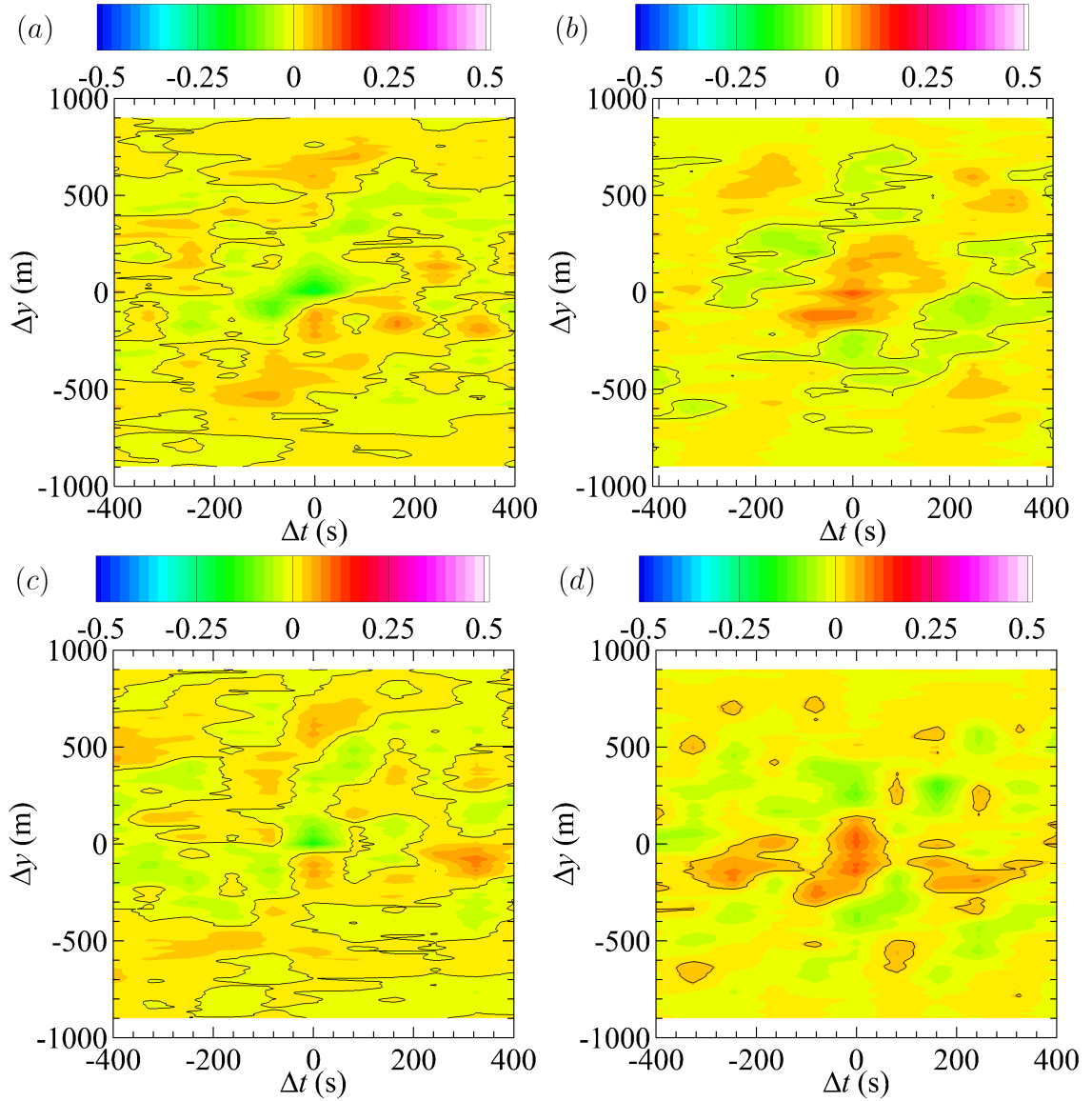


Figure 6.10 Contours indicating magnitude of (a) $\langle\langle R_{u^*w}(\Delta y, \Delta t) \rangle\rangle$ and (b) $\langle\langle R_{w\theta_v}(\Delta y, \Delta t) \rangle\rangle$ measured between 0945 LT and 1030 LT using observations made at $z = 50$ m during Case 1. $\langle\langle R_{u^*w}(\Delta y, \Delta t) \rangle\rangle$ and $\langle\langle R_{w\theta_v}(\Delta y, \Delta t) \rangle\rangle$ measured between 1100 LT and 1200 LT shown in (c) and (d), respectively. From (Al-Ghussain and Bailey, 2022) and used with permission, license number 5513720396324.

the velocity and temperature autocorrelations.

These structures also show the expected turbulent transport behaviour of negative momentum flux (reflected in negative $\langle\langle R_{u^*w} \rangle\rangle$ at $(\Delta y, \Delta t) = (0, 0)$) for Fig. 6.10a, c and positive buoyancy flux (reflected in positive $\langle\langle R_{w\theta_v} \rangle\rangle$ at $(\Delta y, \Delta t) = (0, 0)$) for Fig. 6.10b, d. Notably these regions of negative $\langle\langle R_{u^*w} \rangle\rangle$ and positive $\langle\langle R_{w\theta_v} \rangle\rangle$ are consistent with same length and width scales observed in the autocorrelations.

Finally, we note that similar behaviour was observed for the results from Case 2 (not presented for the sake of brevity). However, the organization of the weakly correlated motions was a little less clear. This reduced clarity is likely due to the increased small-scale activity during Case 2, which required more measurement time than available to achieve sufficient statistical convergence to resolve the underlying coherent motions. One distinct difference noted between Case 1 and Case 2 was that during the 0600 LT to 0700 LT flight for Case 2 the correlations showed evidence of the same large-scale structure observed during the neutral and convective conditions of Case 1.

6.6 Coherent Structure Associated with Sweep and Ejection Events

The previous section demonstrated statistical signatures in correlation fields consistent with the existence of coherent structures at spatial scales on the order of 100 m and temporal scales exceeding 10 minutes. This included correlation between the vertical and horizontal velocity, which is classically organized into ejection and sweep events (see, for example Robinson, 1991) corresponding to negative $\overline{u^*w'}$ events having positive w' (ejection) and negative w' (sweep). Here we utilize the unique nature

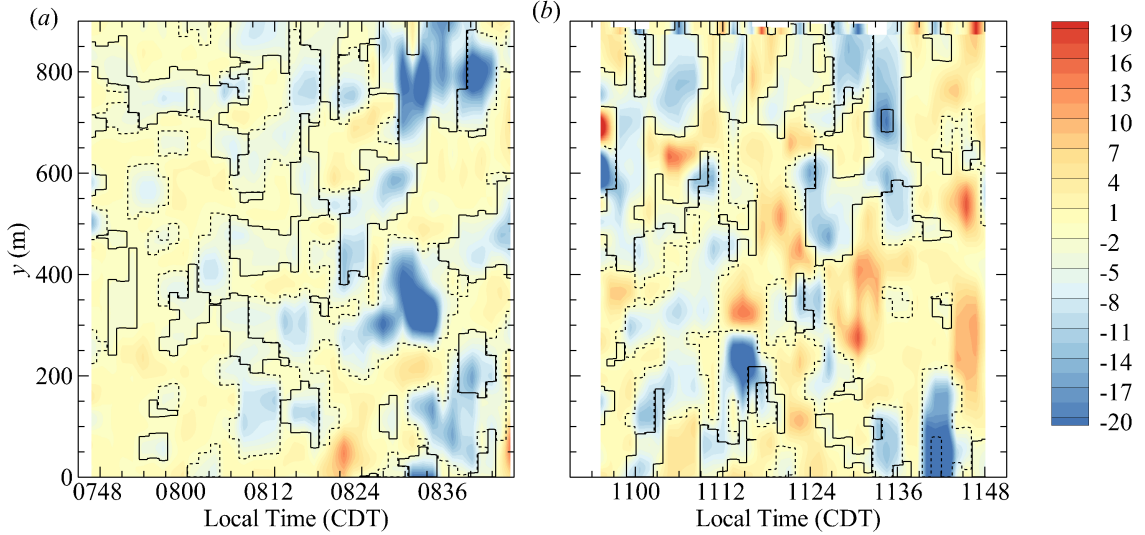


Figure 6.11 Contours of low-pass filtered $u^{*'}w'/u_{\tau}^2$ from observations made at $z = 50$ m (a) measured between 0800 LT and 0845 LT during Case 1 and (b) measured between 1100 LT and 1200 LT during Case 1. Solid lines indicate identified sweep events, dashed lines indicate identified ejection events. From (Al-Ghussain and Bailey, 2022) and used with permission, license number 5513720396324.

of the UAS data to examine the structure of these events in greater detail. Specifically, we note that the use of UAS provides an opportunity to better understand the spatial scale of these structures in the atmospheric surface layer due to their ability to minimize the impact of advection velocity on the measurement of flow structure.

We first look at the spatio-temporal distribution of $u^{*'}w'/u_{\tau}^2$. Examples are shown in Fig. 6.11 from Case 1, specifically the distributions measured between 0800 LT and 0845 LT and between 1100 LT and 1200 LT. Note that, to better isolate the large-scale coherent motions, the $u^{*'}(t)$ and $w'(t)$ fields were first low-pass filtered at 1 Hz (filtering out motions smaller than approximately 20 m). The results shown in Fig. 6.11a reflect the prominence of the negative $u^{*'}w'$ events relative to the positive events in the more mechanically driven, near-neutral stability conditions. Later in the morning (Fig. 6.11b), more large-scale positive $u^{*'}w'$ events were observed, but

there is still a preponderance of negative u^*w' events measured over the same time period.

A procedure was developed to identify sweep and ejection events from these spatio-temporal fields. First, to identify individual ejection events, the low-pass-filtered spatio-temporal regions having magnitude of $u^*w' < -0.05$ and $w' > 0$ were identified. Note that the results were found to be largely insensitive to the threshold selected and -0.05 was selected as it proved a large enough value to reject events too short in duration to be considered ‘coherent’ while also being small enough in magnitude to not filter out larger-scale events. Finally, individual ejection events were isolated by identifying groups of connected measurement points meeting this criterion. To identify individual sweep events, the same procedure was applied, but constrained to $w' < 0$ events.

The results of this identification process are shown in Fig. 6.11 using solid lines to indicate identified sweep events and dashed lines to indicate identified ejection events. The results show a roughly equal distribution of sweep and ejection events. In addition, it appears that several of the larger events are composed of numerous smaller-scale events, which could signal the formation of a larger-scale structure through alignment of smaller structures, similar to the mechanisms proposed for the formation of very-large-scale motions or superstructures in canonical wall-bounded flow (Monty et al., 2007; Hutchins and Marusic, 2007). Alternatively, recognizing Fig. 6.11 represents a spatio-temporal field, these multiple instances could be the same event bisected by the aircraft at different times and may represent temporal evolution of the structure as it advects through the measurement region.

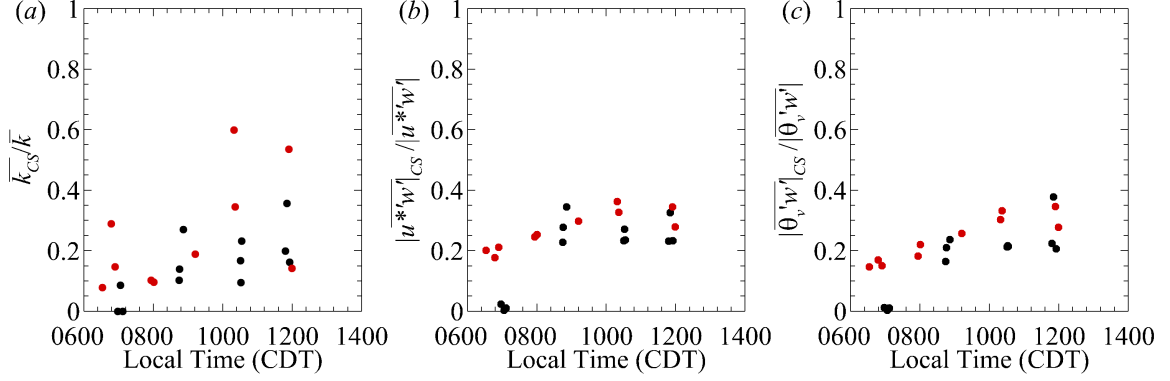


Figure 6.12 Contribution towards total (a) turbulence kinetic energy; (b) momentum flux; and (c) sensible heat flux by ejection and sweep events. Black dots indicate Case 1 and red dots indicate Case 2. From (Al-Ghussain and Bailey, 2022) and used with permission, license number 5513720396324.

To highlight the importance of these structures to the overall turbulence intensity and transport, we evaluated the contributions of the regions encapsulated by these events to the k , $\langle u^*w' \rangle$, and $\langle \theta'_v w' \rangle$ measured over the entire flight. This was done by setting the portions of the filtered u' , v' , w' and θ'_v time series that fell outside the identified sweep/ejection regions to zero, and calculating \bar{k}_{CS} , $|\overline{u^*w'}|_{CS}$ and $|\overline{\theta'_v w'}|_{CS}$ from the time series measured during the flight. Here, the subscripted CS is used to indicate values determined using only measurements from within an identified sweep or ejection event. These values were then compared to the corresponding values of \bar{k} , $|\overline{u^*w'}|$ and $|\overline{\theta'_v w'}|$ determined from the unfiltered data and without nullifying the portions of the time series falling outside the sweep and ejection.

The resulting ratios of \bar{k}_{CS}/\bar{k} , $|\overline{u^*w'}|_{CS}/|\overline{u^*w'}|$ and $|\overline{\theta'_v w'}|_{CS}/|\overline{\theta'_v w'}|$ are presented in Fig. 6.12a, b, c, respectively. In general, the results show that the contribution from the coherent motions increases over the course of the morning, with good agreement between the cases. Although there is significant scatter in the \bar{k}_{CS}/\bar{k} results, this estimate suggests that the sweep and ejection motions account for as much as 10% to

20% of the turbulence kinetic energy and 20% to 30% of the momentum and sensible heat flux. This is comparable to what has previously been reported by Feigenwinter and Vogt (2005) and Barthlott et al. (2007), but much lower than reported by Gao et al. (1989), for example.

The contribution of individual coherent structures to the momentum flux was expanded upon by examining the minimum value of u^*w' measured within each individual sweep and ejection event. Furthermore, we also compare these minimum values to the y -direction (nominally streamwise) scale of each corresponding sweep and ejection event, δy . The results of this comparison are shown in Fig. 6.13a, b for sweep and ejection events respectively. Despite significant scatter, several observations can be made from these figures. The first is that there is a clear correlation between the scale of the structure and the magnitude of $(u^*w')/u_\tau^2$ produced within it. A second observation is that sweep and ejection have similar scales, although there is more variability in the size of the ejection events. There does seem to be qualitative evidence in Fig. 6.13a, b that, given the smaller u_τ occurring earlier in the transition process, the reduced convective activity allows larger structures to form but with a corresponding weaker momentum flux. As the buoyant forcing increases the structures become smaller in scale, but with a corresponding increase in momentum flux.

Finally, to examine the changes in structure of the sweep and ejection events over the course of the morning transition, conditional averaging was conducted. This procedure utilized the same sweep/ejection identification procedure described above but, to minimize the influence of alignment of multiple structures influencing the averaging

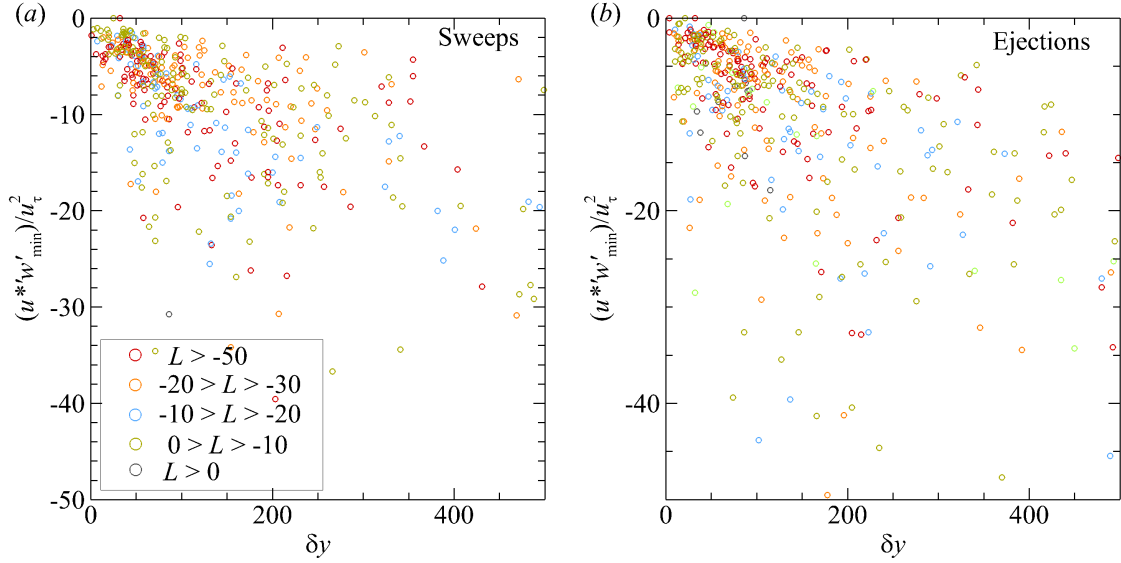


Figure 6.13 Comparison of approximate scale of observed sweep and ejection events to estimated magnitude of momentum flux contribution. From (Al-Ghussain and Bailey, 2022) and used with permission, license number 5513720396324.

process, a more restrictive u^*w' threshold of 80% the minimum measured during each transect was employed. For each individual structure, its spatial, δy , and temporal, δt , extents were determined. Each structure was then re-scaled by $y/\delta y$, $t/\delta t$ and $(u', v', w')/(|u^*w'_{min}|)^{0.5}$ before averaging all identified structures. Here, $|u^*w'_{min}|$ is the minimum value of the shear stress within each structure. The result being an average structure scaled by its peak momentum flux and spatial and temporal extents.

Conditionally averaged velocity vectors corresponding to ejection events are shown in Fig. 6.14 from Case 1, with the events measured from 0800 LT to 0845 LT shown in (a) and from 1100 LT to 1200 LT shown in (b). Although not many events were averaged, some interesting observations can be made. Focusing first on the averaged structure from the earlier morning measurements (Fig. 6.14a), we see evidence of the ejection event flanked by counter-rotating vortex structure at $z = 75$ m. To better

illustrate this we also present the corresponding isocontours of the pseudo-vorticity

$$\tilde{\omega} = \left(\frac{\partial v}{\partial t} \delta t - \frac{\partial u}{\partial y} \delta y \right) \frac{1}{(|u^* w'|_{min})^{0.5}} \quad (6.7)$$

in Fig. 6.14c. Although only an approximate estimate of the z -aligned component of vorticity, these results do suggest the presence of a counter rotational structure extended throughout the measurement plane. This counter-rotating structure is consistent with the observations from zero-pressure-gradient isothermal boundary layers (e.g., Adrian, 2007) of ejection events corresponding to hairpin vortex formation and streamwise vorticity near the surface. Further corroborating the similarity of this structure with the canonical turbulent boundary layer structure is that these ejection events appear to be preceded by upstream sweep events at higher elevations as described by Robinson (1991).

The conditionally-averaged structures from the later morning/convective boundary layer conditions (Fig. 6.14b) are less well-defined. However, some similarities between this structure and that of the earlier morning are evident. Most notably, in the appearance of precedent sweeping events at $z = 75$ m and the indication of counter-rotating vorticity in the corresponding pseudo-vorticity contours of Fig. 6.14d.

For the sweep events, conditionally averaged velocity vectors corresponding are shown in Fig. 6.15a, b from Case 1, with the events measured from 0800 LT to 0845 LT shown in (a) and from 1100 LT to 1200 LT shown in (b). The corresponding $\tilde{\omega}$ corresponding to the results are shown in Fig. 6.15c,d. In general, conditionally-averaged sweep structures display much less organization than the corresponding ejection structure. One notable pattern, however, is that as the surface is approached,

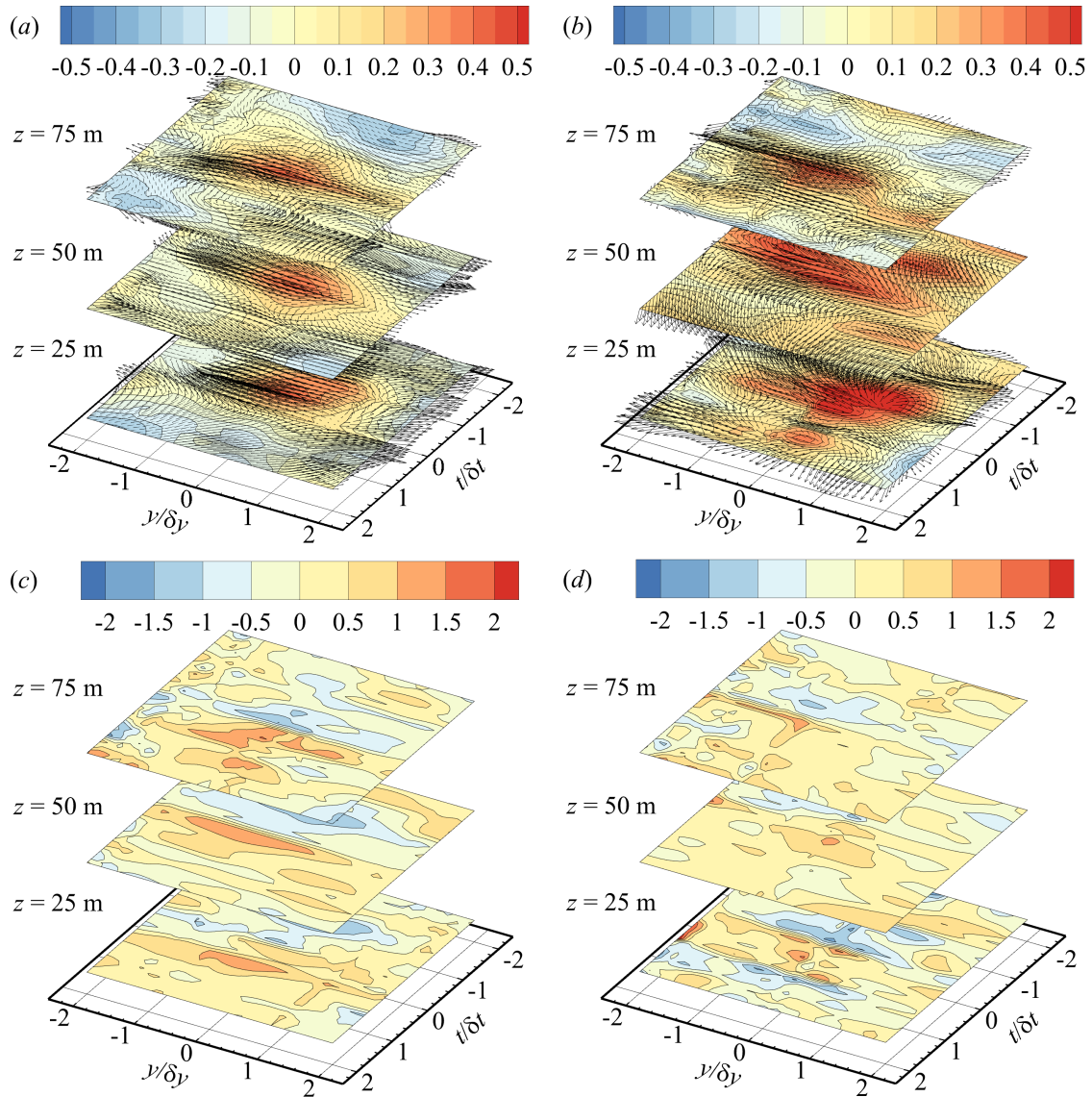


Figure 6.14 Conditionally averaged velocity vectors of ejection events from observations (a) measured between 0800 LT and 0845 LT during Case 1 and (b) measured between 1100 LT and 1200 LT during Case 1. Contours in (a) and (b) are of $w'/(|u^*w'_{min}|)^{0.5}$. Contours of $\tilde{\omega}$ corresponding to the results shown in (a) and (b) are shown in (c) and (d) respectively. From (Al-Ghussain and Bailey, 2022) and used with permission, license number 5513720396324.

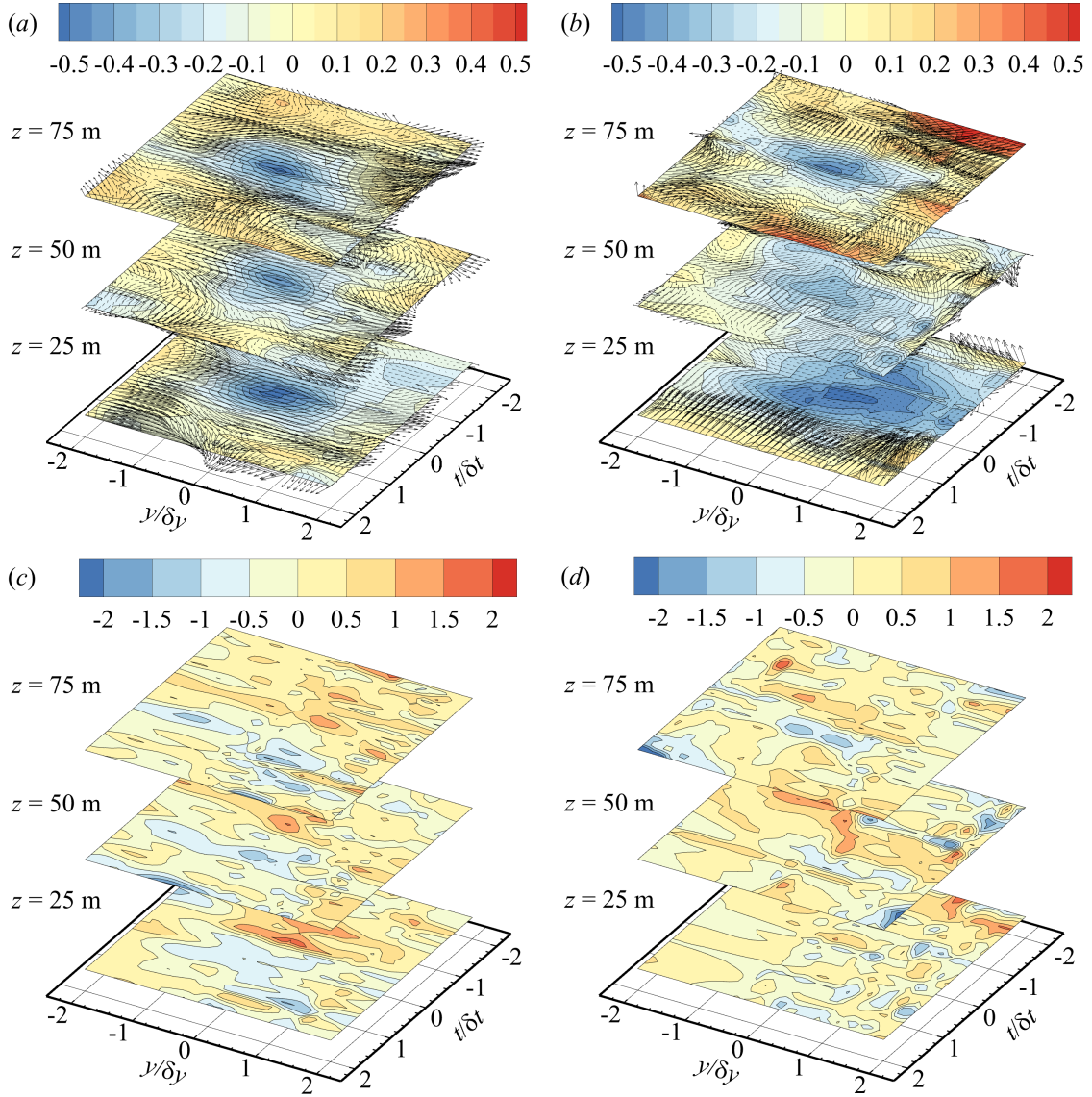


Figure 6.15 Conditionally averaged velocity vectors of sweep events from observations (a) measured between 0800 LT and 0845 LT during Case 1 and (b) measured between 1100 LT and 1200 LT during Case 1. Contours in (a) and (b) are of $w'/(|u*'w'|_{min})^{0.5}$. Contours of \tilde{w} corresponding to the results shown in (a) and (b) are shown in (c) and (d) respectively. From (Al-Ghussain and Bailey, 2022) and used with permission, license number 5513720396324.

the portion of δt and δy encompassed by the negative vertical velocity appears to increase, even though a comparison δt , δy and $(|u^*w'|_{min})^{0.5}$ across the three heights indicates that these scaling factors are approximately the same. This then suggests a spreading of the event as it approaches the surface, reminiscent of a ‘splatting’ event. Evidence of counter-rotation structure flanking the sweep events is also present in the contours of $\tilde{\omega}$, most notably in the 0800 LT to 0845 LT results shown in Fig. 6.15c.

6.7 Summary

Here we demonstrated the UAS capability of investigating the surface layer structure during the morning transition acquired as a part of the 2017 CLOUDMAP measurement campaign. Visualizations of the velocity and temperature fields reflected the formation of turbulent thermals on the scale of hundreds of meters which became stronger as the morning evolved. Moreover, the results of the spatio-temporal correlations applied to quasi-streamwise transects show that the detected structures have spatial extent of approximately 200-m in the streamwise direction. Additionally, spatio-temporal correlations were employed to estimate the advection velocity, which varies significantly as the morning progresses and is different than the mean flow velocity. Such results confirm that the use of frozen Taylor hypothesis to resolve the spatial distribution of the flow field using the mean flow velocity would fail in resolving the actual spatial extent of the flow field. Moreover, an approach was presented to identify sweep and ejection events and highlight their contribution to the overall turbulent kinetic energy, momentum, and sensible heat flux. The results from this analysis agree with some of the findings reported in the literature that con-

firm that coherent structures significantly contribute the aforementioned quantities (up to 30%). Finally, conditional averaging of the spatio-temporal fields of coherent structure indicates that the structure of ejection events observed in the atmospheric surface layer, and structures observed in canonical turbulent boundary layers share some characteristics.

Chapter 7 Coherent Structure Characterization using an Uncrewed Aircraft System Equipped with a Vorticity Probe

Here, we present the development and use of a novel a five-hole-probe-based vorticity probe equipped on a fixed-wing UAS to resolve both velocity and instantaneous localized velocity gradients of the flow field, allowing estimation of the dissipation rate and the vorticity along the aircraft's flight path. These tools are applied to further investigate the ABL structure utilizing the conditional averaging technique.

7.1 Overview of Vorticity Probe

The vorticity probe, developed here, consists of four identical custom-made five-hole probes, each capable of measuring 3D wind components. This five-hole-probe-based vorticity probe is an extension of the 12-wire hot-wire probe concept, which measures three components of velocity at three points on a single probe to determine the velocity gradients at an approximated point in space. Note that a 12-wire probe measures the three velocity components at three locations on a plane transverse to the probe and uses Taylor's hypothesis to get gradients in the direction along the probe axis. To fully-resolve the axial gradients for the vorticity probe used here, an additional fourth measurement point was introduced. This configuration allows measuring the full velocity gradient tensor which can be used for estimating vorticity, Reynolds stress tensor, energy budget measurement, eddy diffusivity quantification, rotation development, and inertial subrange behavior.

There are two distinct disadvantages to using five-hole-probes for this configuration, rather than hot-wire probes. One principle disadvantage is that a five-hole probe, due to tubing constraints, requires larger physical dimensions than a multi-sensor hot-wire probe. This results in a significant loss of spatial resolution. In addition, a five-hole-probe does not possess the same frequency-response characteristics as a hot-wire probe. For the probes used here, a 50 Hz response is estimated compared to a typical hot-wire response of 40 kHz. However, for atmospheric measurements, which have generally larger scales and slower time evolution than laboratory flows, the reduction in spatial and temporal resolution was not as significant.

The probe spacing was selected to ensure that the probes will not interfere with each other assuming 45° as the maximum angle of attack, but at the same time, the spacing is considered small enough to count as measuring a ‘point’ in space. The diameter of the vorticity probe (radial distance between the probe in the center and the other multi-hole probes) was selected to be 1.778 cm as shown in Fig. 7.1. The selected spacing is almost three times the distance suggested by Freestone (1988) and corresponds approximately to 20η in the analyzed atmospheric flow field. This would suggest that we would be measuring local vorticity that corresponds to scales larger than η . It should be noted that a smaller spacing distance is favorable, as suggested by Freestone (1988) however the fabrication process would be challenging. The tip of each multi-hole probe is made from aluminum and has a diameter of 6.17 mm and a length of 5.31 cm. Additionally, the total length of the vorticity probe (from the multi-hole probe tip to the end of the carbon fiber tube) is 55 cm, and an outer radius of 2.5 cm. Each multi-hole probe is connected to three pressure transducers (MS4515

pressure transducers type A) using 71 cm long clear Tygon tubing with inner and outer diameters of 1 mm and 2 mm, respectively. The top and bottom holes of the multi-hole probe are connected to one transducer, left and right holes are connected to a second transducer, whereas the central hole and the static pressure from the pitot tube are connected to a third transducer. The pressure differences across each probe are then used to estimate the calibration coefficients and the three components of relative air velocity using an approach similar to the methodology presented in Chapter 4. As shown in Fig. 7.1, the $P2$ indicates the probe in the center of the vorticity probe, whereas $P1$ and $P3$ indicate the probes on the right and left in the figure, respectively and $P4$ is used when referring to the top probe.

To determine the velocity gradients, the corrected ground-fixed wind velocity measurements (using the V2 version of the correction approach described in Chapter 5) are first determined. As the distance across the probes is small, small differences in the velocity measured by individual probes can cause large biases in the resulting gradients. We therefore assume that all probes should measure the same mean velocity over the entire flight and use the probe in the center ($P2$) as a reference to find linear regression coefficients that correct the mean velocity components of $P1$, $P3$, and $P4$ to match those measured by $P2$ following

$$u_k = u_{0,k} \times (A_u)_k + (B_u)_k \quad (7.1)$$

$$v_k = v_{0,k} \times (A_v)_k + (B_v)_k \quad (7.2)$$

$$w_k = w_{0,k} \times (A_w)_k + (B_w)_k \quad (7.3)$$

where (u, v, w) are the corrected velocity component of probe k with respect to the

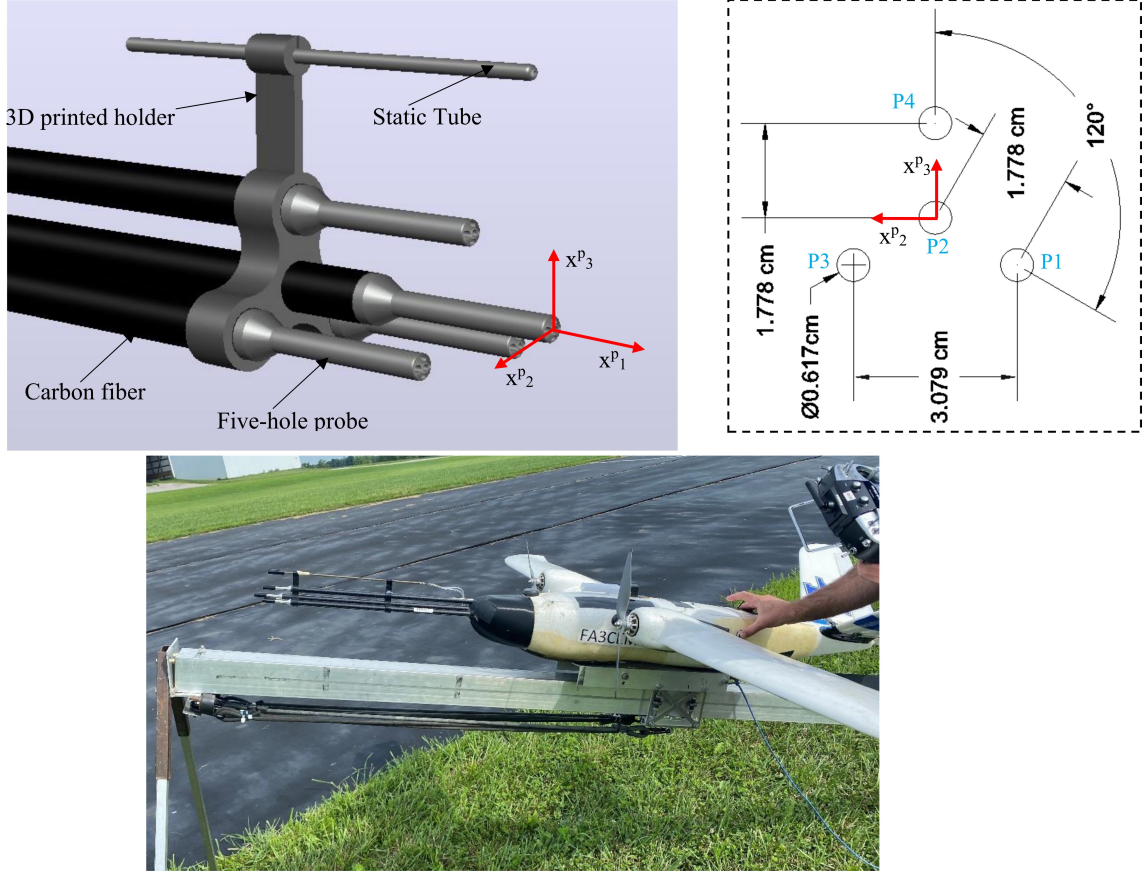


Figure 7.1 Overview of the developed vorticity probe. The superscripted p indicates that these coordinates are in the probe frame of reference.

ground frame of reference, which are aligned with (x, y, z) coordinate system with the x -axis directed towards the east, the y -axis directed towards the north, and the z -axis directed up. (u_0, v_0, w_0) are the original ground-fixed wind velocity measured by probe k , (A_u, A_v, A_w) and (B_u, B_v, B_w) is the linear regression coefficients of (u, v, w) for probe k . To obtain (A_u, A_v, A_w) and (B_u, B_v, B_w) , a linear fit is applied to the moving average of $(u, v, w)_k$ and $(u, v, w)_2$ over the entire flight.

The coordinate system is then rotated to align with the mean wind velocity direction where (x_1, x_2, x_3) and (u_1, u_2, u_3) are the mean-flow-aligned coordinate system.

Afterward, we find the instantaneous velocity gradients using,

$$\left(\frac{\partial u_i}{\partial x_f}\right)_{jk} = \left(\frac{\partial u_i}{\partial H}\right)_{jk} \left(\frac{\partial H}{\partial x_f}\right)_{jk}, \quad (7.4)$$

where $i, f = 1$ corresponds to the streamwise direction, $i, f = 2$ corresponds to the spanwise direction, and $i, f = 3$ corresponds to the vertical direction as shown in Fig. 7.1 all with respect to the mean wind flow direction, j and k are the probe numbers as described in Section 7.1. with,

$$\left(\frac{\partial H}{\partial x_f}\right)_{jk} = \left(\frac{\Delta x_f}{H}\right)_{jk} \quad (7.5)$$

$$\left(\frac{\partial u_i}{\partial H}\right)_{jk} \approx \frac{\overline{(u_i)_j} - \overline{(u_i)_k}}{H_{jk}} \quad (7.6)$$

where,

$$H_{jk} = \sqrt{(\Delta x_f)_{jk}^2} \quad (7.7)$$

Here, the overline indicates a moving time average over an optimized period (p_{mov}) which is found by solving the optimization problem using the Nelder-Mead minimization approach in MATLAB. The optimization's objective was to minimize the mean error over the entire flight between the mean dissipation rate estimated from the power spectrum using Eq. 6.5 following the methodology presented in (Bailey et al., 2019) and the mean vorticity estimated using the gradients of the velocity fluctuations, $\langle \varepsilon(t) \rangle$, where $\langle \rangle$ brackets indicate spatial averaging over each transect and with $\varepsilon(t) = \nu \frac{\partial u(t)'_i}{\partial x_f} \left(\frac{\partial u(t)'_i}{\partial x_f} + \frac{\partial u(t)'_f}{\partial x_i} \right)$.

The configuration of the vorticity probe allows the estimation of $\frac{\partial u_i}{\partial x_1}$ from three-probe combinations (i.e. the three combinations of $P2$ with $P1$, $P3$ and $P4$) whereas

$\frac{\partial u_i}{\partial x_2}$ and $\frac{\partial u_i}{\partial x_3}$ can be estimated from five probe combinations (i.e., all possible pairs that can be formed between the individual probes excluding the horizontal gradients between $P1$ and $P3$ and vertical gradients between $P2$ and $P4$). The repeated quantities are averaged, and this averaged value is used in the analysis. It should be noted that the gradients of the velocity fluctuations are estimated using the same procedure presented for the velocity gradients.

7.2 Overview Calibration Setup

As aforementioned, the estimation of the all three velocity components relative to the probe's axis requires determination of $C_{P_{yaw}}$, $C_{P_{pitch}}$ and $C_{P_{total}}$ as a function of α and β . Each probe is expected to have a slightly different response since they are individually fabricated. Furthermore, the configuration of the vorticity probe is such that there may be interference effects between the probes, therefore calibration maps were constructed by pre-calibrating the vorticity probe in a known velocity field in a controlled environment (i.e. an open-jet wind tunnel with a flow conditioning section consisting of a series of meshes and honeycombs to laminarize the jet exit). These calibrations consisted of varying the angular position of the probe and recording the pressure difference measured ($p_3 - p_2$, $p_5 - p_4$ and $p_0 - p_s$), using these pressure difference to calculate the calibration coefficients following the methodology presented in Chapter 4 with the adjustments made for the reduced transducer count required for the vorticity probe of $\bar{p} = -0.5(|(p_5 - p_4)| + |(p_3 - p_2)|)$.

To conduct these calibrations, a custom-built automatic calibration setup, shown in Fig. 7.2, was developed for both multi-hole and vorticity probe use. The calibration

setup consists of the following:

- L-shaped rack with a sleeve to hold the probe and two supports: one with wheels to support the L-shape rack and reduce the load on the rotary table and the second one is used to reduce the vibration of the probe during the calibration.
- Two-stepper motors (Vexta PK245, Velmex Inc., Bloomfield, NY, U.S.A.) each attached to a rotary table (B5990TS, Velmex Inc., Bloomfield, NY, U.S.A.) and a controller (VXM-2, Velmex Inc., Bloomfield, NY, U.S.A.) to control the angular position (yaw and roll angles) of the probe.
- Differential transducers board (MS4515 pressure transducers type A) connected to a 16-bit data acquisition system (USB-6212, NI Inc, Austin, TX, U.S.A.) to record the observations.
- A personal computer with custom-built LabVIEW code used to:
 - set the wind tunnel speed using the feedback from the wind tunnel Pitot-static tube
 - perform sequential angular positioning of the probe
 - record the pressure data as a function of the probe’s angular position at 3000 Hz.

The calibration setup is mounted on a table in front of the open-jet wind tunnel as shown in Fig. 7.2, separated from the inlet by a 5 cm horizontal distance with the probe positioned to be at the center of the wind tunnel flow area where the smallest velocity gradients were measured. The yaw traverse range of the calibration setup was $\pm 40^\circ$ whereas the roll range was $\pm 90^\circ$ with the resolution of both angles 0.05° .

The vorticity probe calibrations were conducted at a wind tunnel speed of 18

m/s to match the cruise velocity of the UAS. Note that investigations for which calibrations were carried out at different wind tunnel speeds demonstrated that the calibration coefficients were unaffected by the calibration velocity (over the expected range of UAS airspeeds).

As the desired calibration maps are a function of α and β , it was necessary to transform the calibrator’s known yaw (γ) and roll (ϕ) angles to α and β . This was done using

$$\alpha = \tan^{-1} \left(\frac{\sin(\phi) \sin(\gamma)}{\cos(\gamma)} \right) \quad (7.8)$$

$$\beta = \tan^{-1} \left(\frac{\cos(\phi) \sin(\gamma)}{\cos(\gamma)} \right). \quad (7.9)$$

7.3 UKNRF Flight Campaign

To evaluate the ability of the vorticity probe to measure properties of coherent structures, a measurement campaign was performed. This campaign was conducted at the University of Kentucky North Research Farm (UKNRF) surrounded by agricultural lands planted with different crops. The farm is located at 38.119274° latitude, -84.496803° longitude, and 241.54 m above sea level. Here, again we will use local time (LT) when referencing the time of day, which was Eastern Standard Time (EST) or UTC-5. The campaign occurred on August 17, 2022, starting just after sunrise during the morning transition period at 8:30 am LT and ending at 1:15 pm LT with a total of three flights referred to as Flight 1, Flight 2, and Flight 3. The primary measurement systems used for the experiment consisted of three UASs aircraft, two fixed-wing UASs for horizontal profiling, and one rotorcraft for vertical profiling.

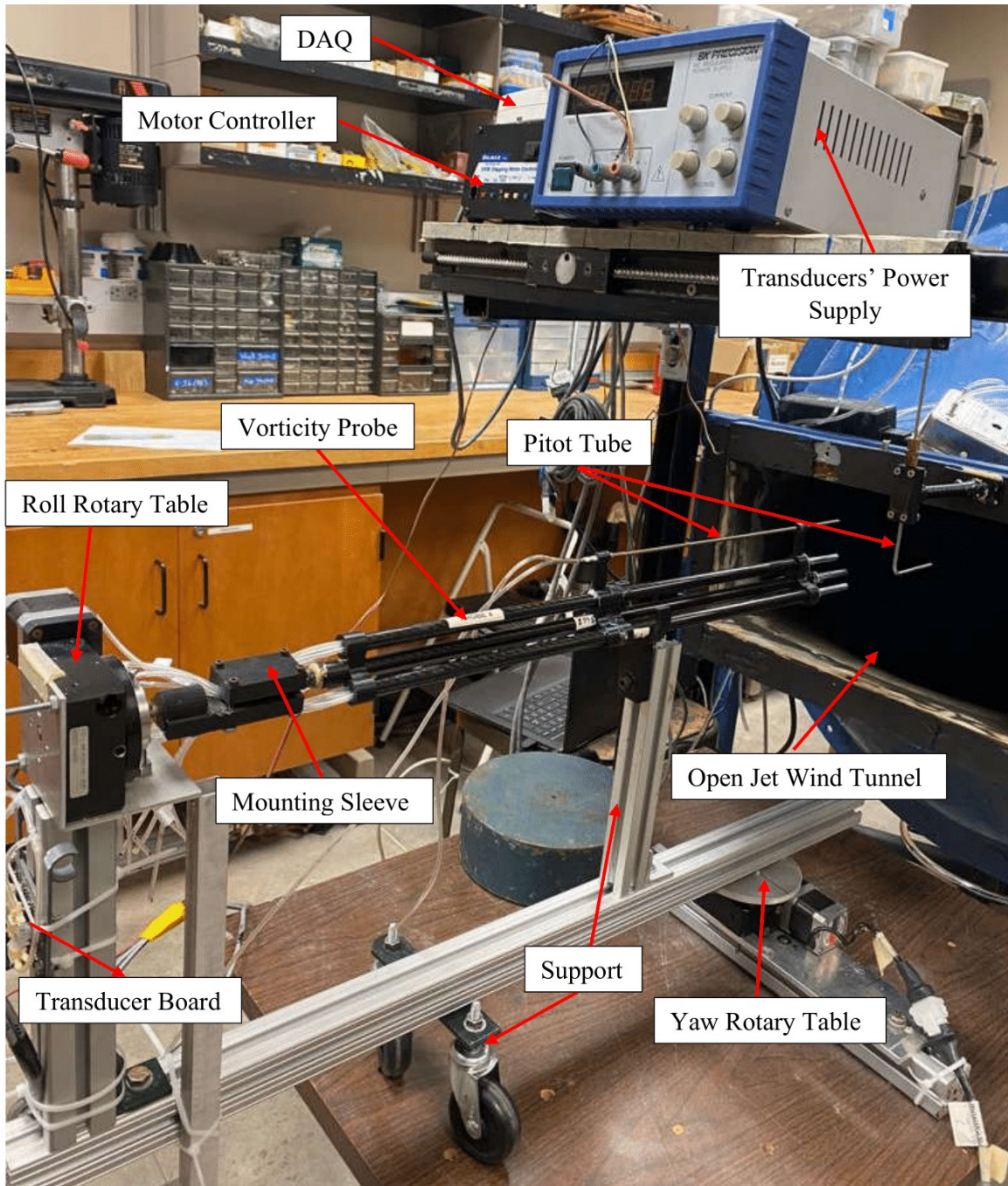


Figure 7.2 Multi-hole probe automated calibration setup.

The fixed-wing UAS (BC6B and BC6E) were BLUECAT6 aircraft flown at 50 m a.g.l, as illustrated in Fig. 7.3. The BC6 aircraft are modified Believer airframes (MakeFlyEasy, SiChuan, China) and have a wingspan of 1.95 m, length of 1.22 m, gross weight of 6.58 kg and payload capacity of 2.27 kg. BC6 aircraft are launched using a custom-built bungee-powered catapult launcher (shown in Fig. 7.3c) and have the capability to loiter at a speed of 19 m/s and a maximum flying speed of 24.7 m/s with an average flight endurance of 1.5 hours, depending on the battery type used. The aircraft is a twin-motor aircraft with each wing equipped with a single brushless motor driving a 0.3048 m propeller. The aircraft is equipped with a commercial autopilot (Pixhawk 2.1, 3DRobotics, U.S.A.) that sends telemetry information to the groundstation using a 900 MHz radio link (RFdesign 900X-US, GA, U.S.A.). This radio link also allows the ground controllers to update mission parameters while the aircraft is in flight. Manual control of the aircraft is provided using a standard 2.4 GHz RC radio link which passes command information through the autopilot prior to being delivered to the servos, allowing the aircraft to be switched between manual control, stabilized manual control, and waypoint-following modes.

Each aircraft was equipped with a custom-made sensor referred to as a SamaMet, described by Ladino et al. (2022). This sensor is capable of measuring pressure (p), temperature (T), and relative humidity (RH) at a rate of 1 Hz. The BC6 aircraft were equipped with a VectorNav inertial measurement system with dual GNSS (VN-300, Dallas, TX, U.S.A.) which was used to acquire the UAS orientation as well as the aircraft velocity in the ground-fixed frame of reference. The BC6B fixed-wing aircraft was equipped with a 3D-printed nose to hold the vorticity probe, as

shown in Fig. 7.1. Data from the pressure transducers is logged at 1000 Hz using a 16-channel, 16-bit data acquisition system (USB-1608G, Measurement Computing Corporation, Norton, MA, U.S.A.). The BC6E measured the three-components of the relative velocity vector using a custom-made five-hole probe at 200 Hz using a 16-bit data acquisition system (USB-1608FS-Plus, Measurement Computing Corporation, Norton, MA, U.S.A.). Data logging and storage for the multi-hole probes, SamaMet and VectorNav was conducted using a mini PC stick computer running custom-made LabView-based software.

Finally, a Foxtech Hover1 quadcopter was utilized to measure the vertical gradients of atmospheric properties. The aircraft performed vertical ascents and descents at 1 m s^{-1} between 10 m and 120 m, as illustrated in Fig. 7.3 while being flown concurrently with the fixed-wing aircraft. The aircraft was put back in the air once the batteries were replaced. This aircraft was equipped with a Trisonica Mini 3D sonic anemometer (Anemoment LLC, Longmont, CO, U.S.A.) mounted on a 0.6 m mast to prevent distortion of the measured wind by the aircraft's rotor wash. Additionally, it was equipped with SamaMet sensor and an iMet-XQ sensor for pressure, temperature, and relative humidity measurements.

Each flight consisted of each aircraft repeatedly traversing the same 1000 m long straight line transect at a true airspeed of 18 m s^{-1} (Fig. 7.3a and b). Typically 80-90 transects were made per flight in alternating directions with each transect taking around 75 s. The vorticity probe was mounted on BC6B which was flown for about 50 min in horizontal transects making an angle of 114° with the mean wind direction to increase the probability of transecting coherent structures as shown

in Fig. 7.3. BC6E was equipped with a single multi-hole probe and was flown simultaneously to BC6B for about 115 min in horizontal transects making an angle of 23° with the mean wind direction, as shown in Fig. 7.3. This aircraft was intended for measuring the advection velocity of coherent structures. The advection velocity was found by finding the spatial and temporal shifts in the peak streamwise velocity cross-correlation, where it was applied on every two consecutive transects.

The measured quantities are presented in an (x, y, z) coordinate system with the x -axis directed towards the east, the y -axis directed towards the north, and the z -axis directed up, and with the origin of the coordinate system located at the aircraft launch point (Fig. 7.3b). The wind velocity components (u, v, w) are aligned with the (x, y, z) axes, respectively.

7.4 Mean Background Properties of the Boundary Layer

Here we estimate the atmospheric properties of the boundary layer during the vorticity probe measurements campaign to investigate the stability of the ABL. To do so, we use the data acquired by the fixed-wing UAS (BC6E) along with some information from the Hover1. Similar to the procedures outlined in Chapter 6, spatially average quantities were calculated from each horizontal transect (only when UAS is in the automated flight pattern), assuming steady-state conditions for each transect, and indicated by $\langle \rangle$ brackets. Figure 7.4(a) shows an increase in the horizontal components of wind velocity, with increasing variability after 0800 LT. This increasing variability is further reflected in the time evolution of the turbulent kinetic energy, which is shown in Fig. 7.4(b) and coincides with the evolution in the potential temperature in

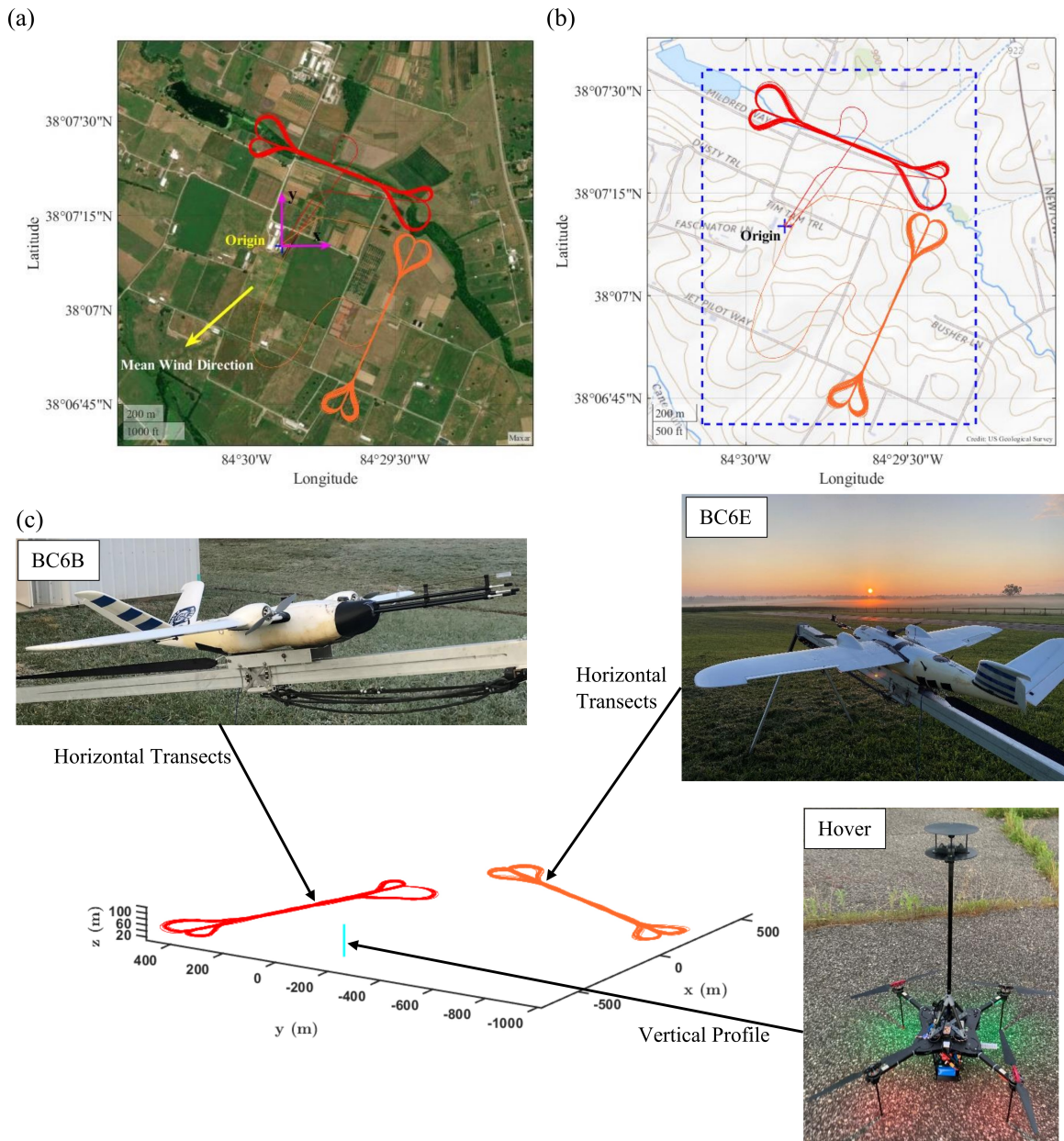


Figure 7.3 (a) Topographic map showing terrain surrounding measurement with (b) detailed satellite photograph of the area highlighted by the blue box in (a). (c) shows the fixed-wing and rotorcraft UAS used, along with an additional illustration of the different flight path altitudes. The red trajectories indicate the flight path of BC6B, which carried the vorticity probe whereas the orange trajectories indicate the flight path of BC6E which carried the standard five-hole probe.

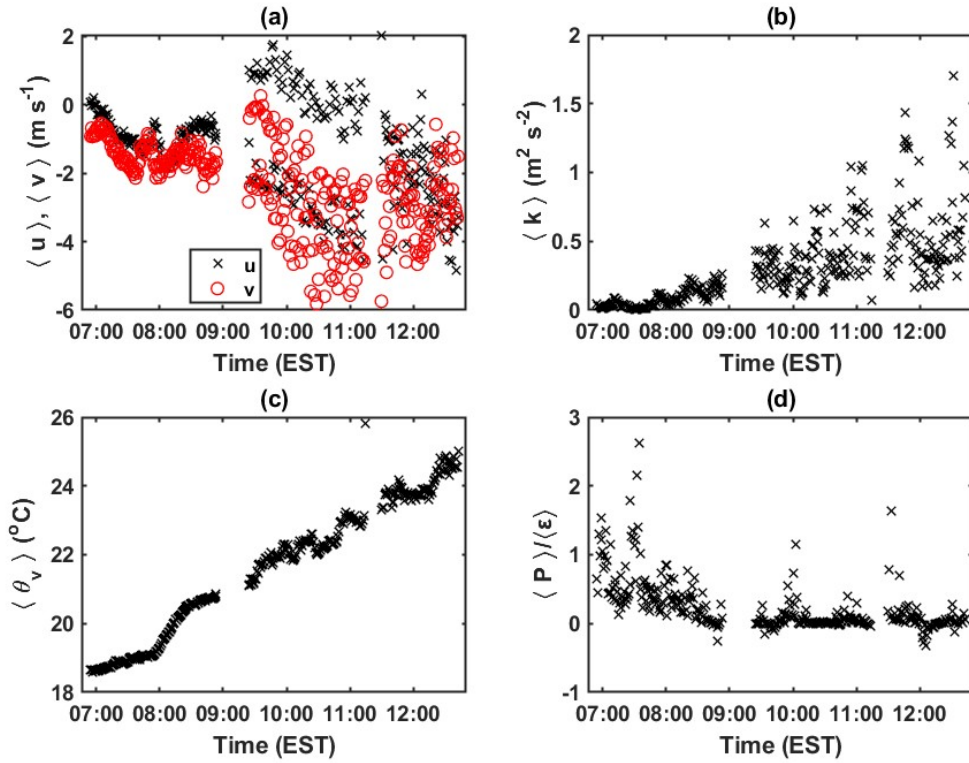


Figure 7.4 Evolution of flow field background statistics with time: (a) $\langle u \rangle$ and $\langle v \rangle$; (b) $\langle k \rangle$; (c) $\langle \theta_v \rangle$ and (d) $\langle P \rangle / \langle \varepsilon \rangle$.

Fig. 7.4(c). This indicates that the ABL is characterized by stable conditions before 0800 LT where after that, convective conditions start to dominate with an increase in the turbulent intensity. Moreover, by adopting the same approach presented in Section 6.3 including the use of the horizontal velocity gradient from the rotorcraft, we present $\langle P \rangle / \langle \varepsilon \rangle$ to evaluate the relative contribution of mechanical production to total production as presented in Fig. 7.4(d). Assuming negligible turbulence advection and negligible pressure fluctuations, it is possible to interpret Fig. 7.4(d) as the relative share of mechanical production in the total turbulent production. It can be seen that the share of mechanical production decreases after 0800 LT, whereas before that, mechanical production is the dominant source of turbulence production.

7.5 Spatial Observations of Flow Structure

As discussed in Section 2.5, the dissipation rate is an important quantity that, in atmospheric measurements, is often used as a measure of turbulence intensity in lieu of k . However, the estimation of the turbulent dissipation rate is usually carried out assuming Kolmogorov’s theories can be applied in all cases, which assumes homogeneous and isotropic turbulence and the corresponding presence of an inertial sub-range scales with the $-5/3$ slope in the energy spectrum. Additionally, frozen Taylor’s hypothesis is often employed to transform the frequency spectrum to a wavenumber spectrum, and the validity of this hypothesis has been questioned (Wacławczyk et al., 2017; Al-Ghussain and Bailey, 2022), particularly as it assumes the advection velocity is constant for all wavenumbers. Hence, the ability to spatially resolve the dissipation rate from the small-scale velocity gradients of the velocity fluctuations is attractive and here we demonstrate the use of the vorticity probe presented in Section 7.1 for measurements of ε over in the spatio-temporal domain.

To do so, we first rotate the flight trajectory on the horizontal plane to align with the mean wind velocity direction where (x_1, x_2, x_3) and (u_1, u_2, u_3) are the mean-flow-aligned coordinate system with u_1 and x_1 in the mean-flow direction. The gradients of the instantaneous velocity vector components and their corresponding fluctuations about the mean were estimated using the approach presented in Section 7.1. The optimal time averaging window size, p_{mov} , was found to be 0.028 s for the first two flights and 0.108 s for the third flight, respectively. When compared to an approximate frequency response of 50 Hz for these five-hole-probes (Witte et al., 2017), these

window sizes are on the order of that expected for the frequency response of the probe temporal resolution. As mentioned in Section 7.1, the configuration of the vorticity probe allows the estimation of the velocity gradients from different probe combinations, allowing a rough uncertainty estimate from the differences in velocity gradient calculated between each probe combination and found to be between ± 3.4 and ± 4.1 m/s² for the UKNRF campaign measurements.

Finally, ε was calculated using both Equation 2.4 and Equation 2.6 for every measured instant in time. These results were then averaged along each transect (each horizontal pass of the aircraft in a single direction) allowing a comparison to ε estimated using Equation 6.5. It should be noted that the presented data were processed by applying a low-pass filter with a cut-off frequency of 1 Hz for data smoothing. The results are shown in Fig. 7.5 which shows that the velocity gradients measured by that vorticity probe produce values that are consistent with the expected values under these conditions. Additionally, these results show that spacing of the individual probes in the vorticity probe design- almost 20η - does not result in significant error when estimating the small-scale velocity gradients.

The results in Fig. 7.5 depict the ability of the vorticity probe using the proposed procedure to measure the mean dissipation rate with reasonable agreement compared to the other approaches. The dissipation rate estimated using the power spectrum approach in Fig. 7.5(b) shows the largest discrepancies between 1050 LT and 1115 LT compared to the other approaches, which could be caused by the misfit of the inertial sub-range to the $-5/3$ slope theory proposed by Kolmogorov (Kolmogorov, 1941; Wang et al., 2021). This misfit could be attributed to the change in the wind direc-

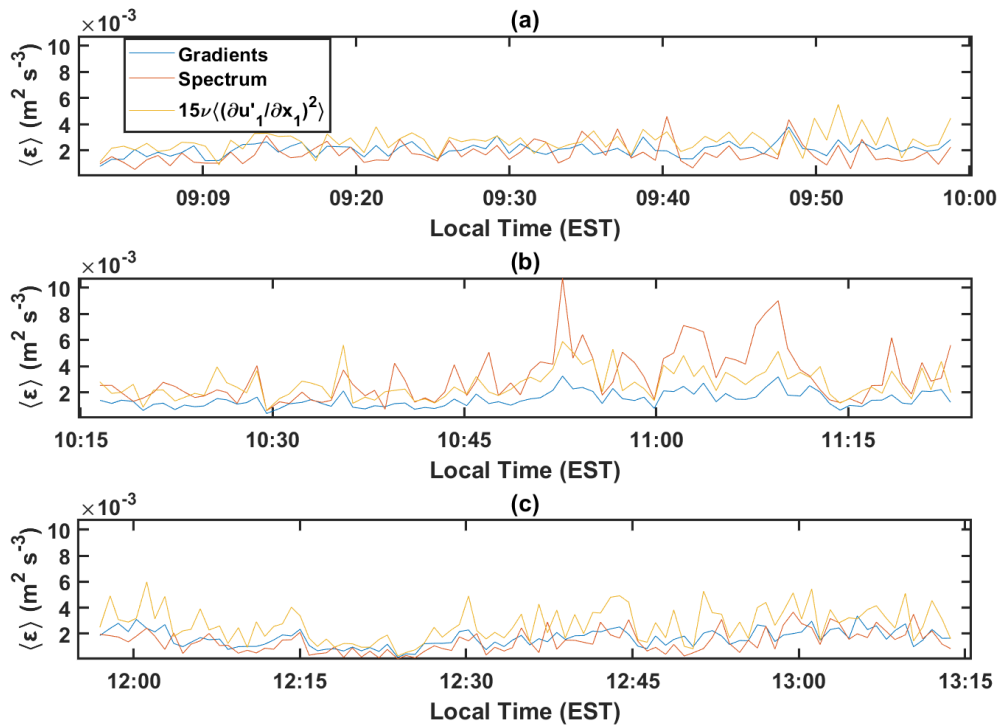


Figure 7.5 Evaluation of the average dissipation rate measured by the vorticity probe throughout the three flights during the UKNRF campaign on August 17, 2022. (a) represents Flight 1 started at 0839 LT; (b) Flight 2 started at 1009 LT and (c) Flight 3 started at 1140 LT.

tion during that period affecting the power spectrum that is supposed to be in the longitudinal direction. Despite that, it is clear that the dissipation rate from the proposed procedure follows the same trends as the dissipation rates estimated using the other approaches implying the ability to use the proposed approach to measure both the spatial and temporal extents of the dissipation rate using the vorticity probe. It should be noted that the temporal extent of the measured dissipation rate can be transformed to a spatial extent using the advection velocity measured by the second UAS (BC6E), which was flying perpendicular the vorticity-probe-carrying UAS. The mean advection velocities for Flight 1, 2, and 3 were 2.4 m/s, 2.15 m/s, and

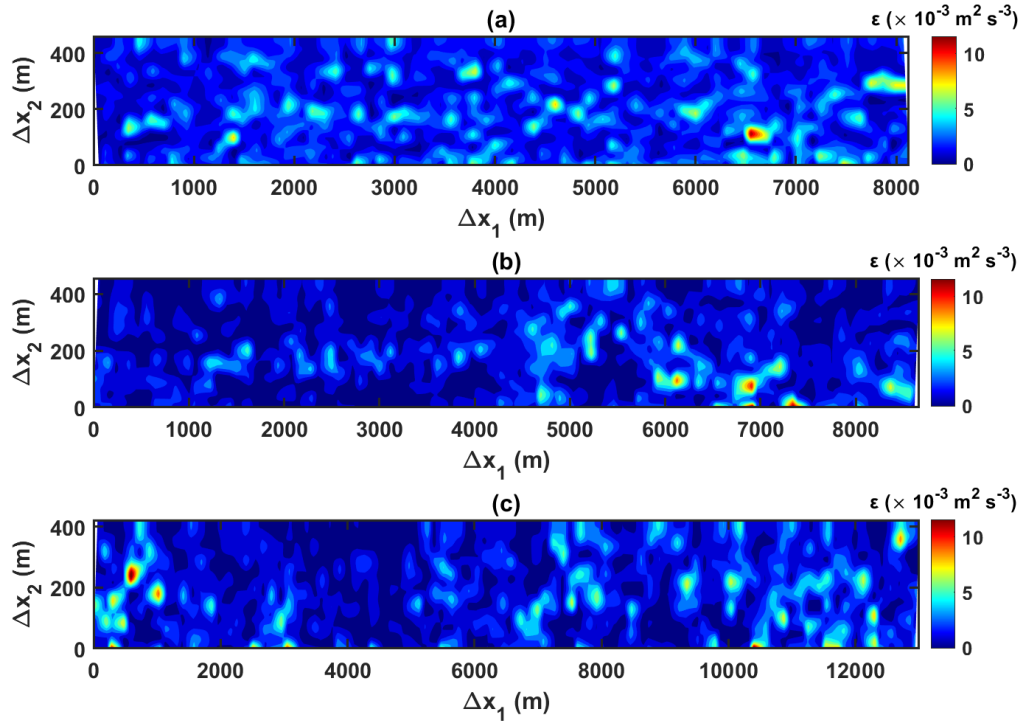


Figure 7.6 Spatial isocontours of dissipation rate measured by the vorticity probe during UKNRF campaign on August 17, 2022. (a) represents Flight 1 started at 0839 LT; (b) Flight 2 started at 1009 LT and (c) Flight 3 started at 1140 LT.

2.8 m/s, respectively. These advection velocities are smaller than the average horizontal wind velocities by 80%, 42%, and 40% for the three flights, respectively. The spatial distribution of the dissipation rate resolved by the vorticity probe during the flight campaign is shown in Fig. 7.6.

These spatial isocontours show intense regions of the dissipation rate with intermittent behavior similar to what has been previously observed in the literature (see, for example Morshed et al., 2013; Li et al., 2021). Additionally, these isocontours show strong signatures on the existence of coherent structures (lump regions) in the streamwise and spanwise directions which is also evident in other atmospheric quantities isocontours such as the fluctuations of the virtual potential temperature

isocontours as shown in Fig. 7.7. It can be seen in Fig. 7.7 negative regions flanked by positive regions and vice versa which indicates that these regions correspond to mixing events that become more intense as the day progresses with the increase in buoyancy production. During the morning, Fig. 7.7(a), these events have horizontal length scales in the streamwise and spanwise directions on the order of 200 m. As the morning progresses, Fig. 7.7(b) and (c), these scales increase especially in the streamwise direction (x_1) as the morning progresses with scales up to 600 m which is consistent with either hairpin vortices legs or low-momentum streaks that evolve and form the legs of hairpin vortices (e.g., Moeng and Sullivan, 1994; Kim and Park, 2003; Newsom et al., 2008; Iwai et al., 2008; Alcayaga et al., 2020). Similar length scales and similar mixing events are observed in the vorticity components; see for example, the spatial isocontours of spanwise vorticity in Fig. 7.8. Additionally, it can be seen in Figs. 7.6 and 7.8 that the intense dissipation regions coincide with intense vorticity regions similar to what was previously observed by others (see, for example Worth and Nickels, 2011).

7.6 Average Flow Structure Visualization

Conditional averaging is a technique used to identify and analyze coherent structures. One specific application of this technique is to get a better understanding of coherent structures' formation and behavior (e.g. Samie et al., 2022). To do so, conditional averaging requires the selection of events where certain criteria is met, which here will be those associated with the occurrence of a sweep or ejection event, and then average either the spatial, or temporal properties which surround these events to reveal the

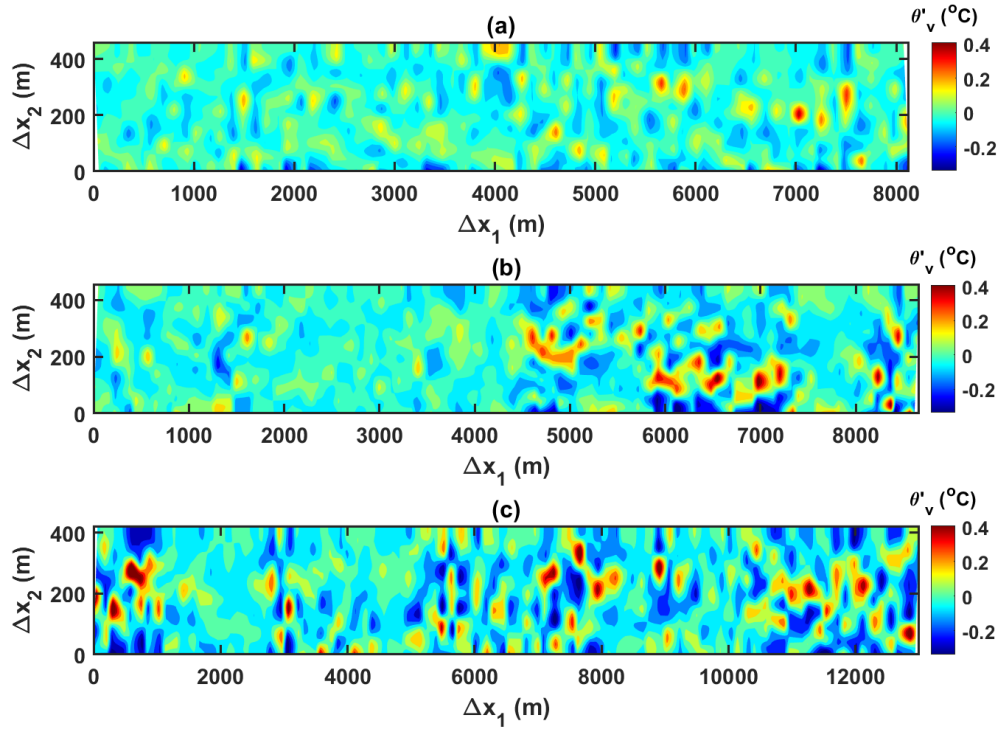


Figure 7.7 Spatial isocontours of virtual potential temperature fluctuations measured during UKNRF campaign on August 17, 2022. (a) represents Flight 1, which started at 0839 LT; (b) Flight 2 which started at 1009 LT; and (c) Flight 3 which started at 1140 LT.

average behavior corresponding to such events, that may not be apparent in the full dataset.

Hence, the first step in the conditional averaging analysis is to define the criteria that will be used to select the regions of the data that will be averaged. Here, the criteria will be based on the momentum flux ($u'_1 u'_3$) and we define a threshold of 80% of the minimum $u'_1 u'_3$ measured during each transect and assume instances where the measured value is below this threshold is an instance where the UAS has flown through a sweep or ejection. Such a local minimum is a well-recognized signature of hairpin vortices, as discussed in Carper and Porte-Agel (2004). Specifically, the local minima that meets the criteria is the condition which will be averaged on. Then, we identify

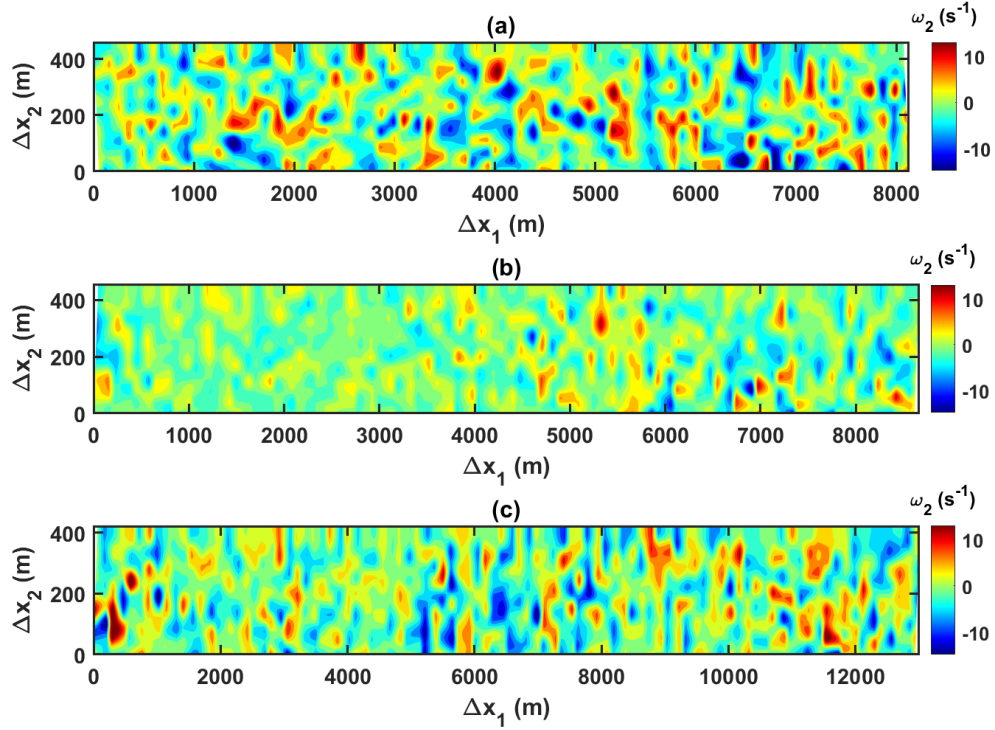


Figure 7.8 Spatial isocontours of spanwise vorticity component measured by the vorticity probe during UKNRF campaign on August 17, 2022. (a) represents Flight 1 started at 0839 LT; (b) Flight 2 started at 1009 LT and (c) Flight 3 started at 1140 LT.

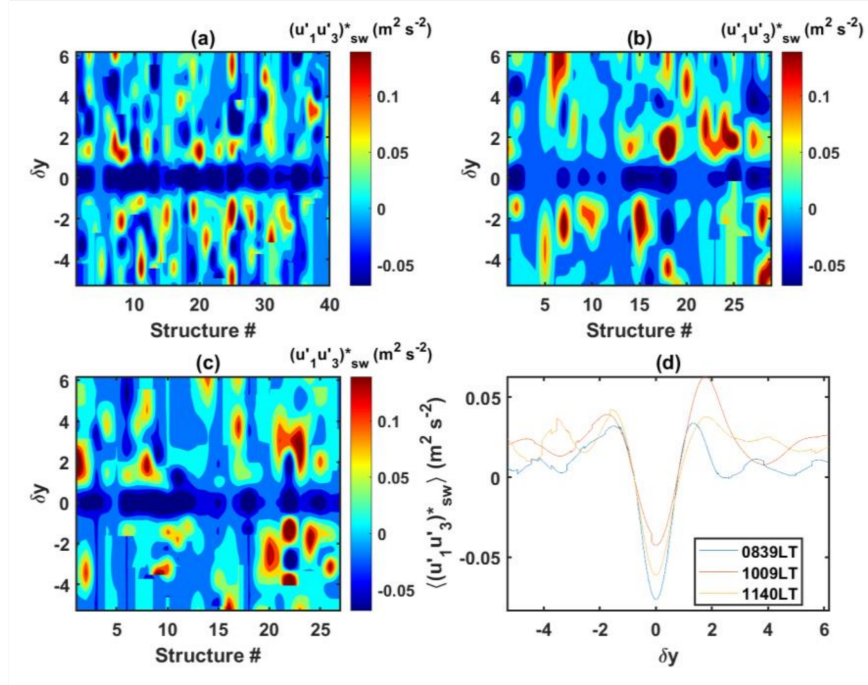
the location of each event (loc_{str}) along each transect and use it to create a matrix of the spanwise extent of the flow field parameters surrounding loc_{str} for each structure. We then re-scale the shifted spanwise spatial extent ($x_2 - loc_{str}$) by the spanwise width of the coherent structure (wd), where the re-scaled spatial extent is represented by δy . In contrast, atmospheric quantities are re-scaled by $norm = \frac{|u'_1 u'_3|_{max}}{\langle |u'_1 u'_3| \rangle}$ before averaging all identified structures where the re-scaled quantities are denoted by *. Finally, we sort the identified structures using sweep and ejection events to better understand and characterize the coherent structures.

First, we look at the sorted momentum flux isocontours that correspond to sweep and ejection events to ensure the ability of the conditional averaging to identify

and sort these structures and to evaluate any associated patterns associated with these structures. Figure 7.9 shows the isocontours and the average flow structure of the momentum flux during the UKNRF flight campaign. It can be seen that the conditioning was able to isolate the events that correspond to the minimum momentum flux and, later, in obtaining the average flow structure. Figure 7.9 shows that each detected structure corresponds to an increase in the local momentum flux during both sweep and ejection events. This is further confirmed by the same trends in the velocity fluctuation fields as well as the heat flux. Additionally, the conditionally-averaged streamwise and vertical velocity fluctuations follow the expected trends for sweep and ejection events as shown in Fig. 7.10. As ejection events play an important role in transporting low-momentum fluid away from the surface by positive vertical velocity, whereas sweeps transport high-momentum fluid toward the surface by negative vertical velocity, concentrated regions of high and low velocities and are implicit to such events (for example, Hussain, 1983, 1986).

As the heat flux is closely coupled to the momentum flux, it should present strong signatures on the presence of coherent structures in these results, where such signatures usually involve a localized ramp in the temperature and hence in the heat flux profiles. Looking at the sorted heat flux isocontours in Fig. 7.11, we notice a peak/valley in the heat flux surrounded by valley/peak in both sweep and ejection events during the three flights, which are consistent with mixing events and similar to what was observed by others (for example, Krusche and De Oliveira, 2004; Barthlott et al., 2007) and have been related to coherent structures. Additionally, the flow structure of the heat flux during the first flight has a counter profile compared with

(I) Sweep Events



(II) Ejection Events

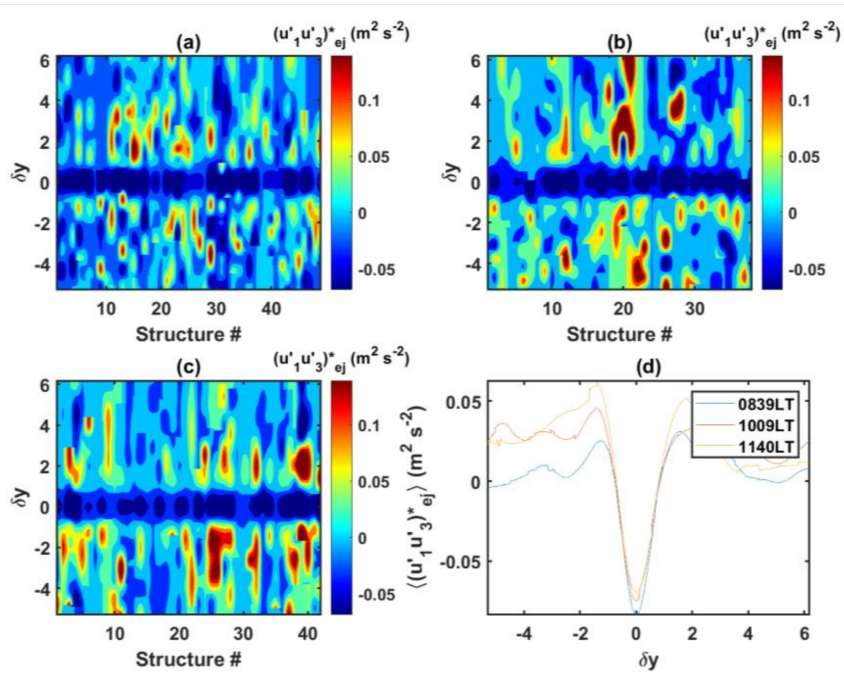


Figure 7.9 Momentum flux sorted by sweep and ejection events during UKNRF campaign on August 17, 2022. (a) Isocontours of Flight 1 which started at 0839 LT; (b) Isocontours of Flight 2 which started at 1009 LT; (c) Isocontours of Flight 3 which started at 1140 LT and (d) mean profile of the conditionally averaged momentum flux during the three flights.

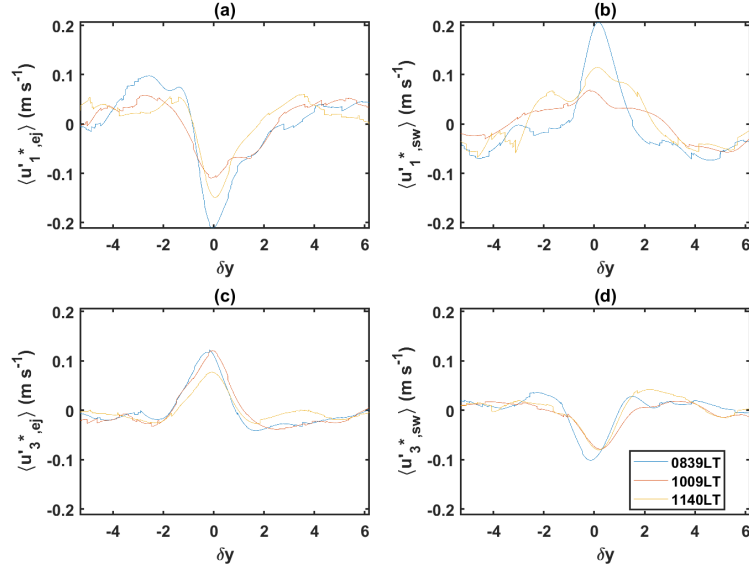
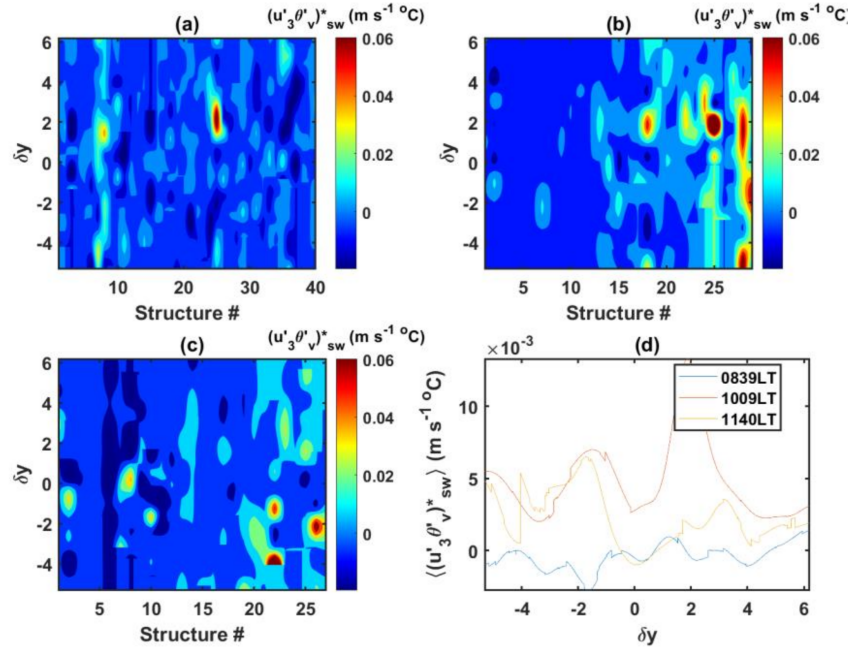


Figure 7.10 Average structure of the streamwise (in *a&b*) and vertical velocity fluctuations (in *c&d*) sorted by sweep (denoted by *sw*) and ejection (denoted by *ej*) events during UKNRF campaign on August 17, 2022.

the two later flights. During the first flight, the earth's surface is cold, and hence during ejection events, colder air is ejected toward the atmosphere, which is replaced by warmer air during sweep events. Whereas, as the morning progresses the earth's surface heats up and the ejected air during ejection events becomes warmer than the air far from the surface which would be then replaced by cold air by sweep events.

The mixing events observed in the heat flux are also evident in the vorticity fluctuation fields, see for example, the streamwise vorticity in Fig. 7.12, with intense vorticity regions at the location of the coherent structure flanked by counter-rotating vorticity fluctuation regions. This could be a signature on the legs of the hairpin vortices similar to what was observed by (Carper and Porte-Agel, 2004). Moreover, notice that the vorticity fluctuation flips sign after the first flight, this could be related to the increase in the buoyancy production as the morning progresses which is

(I) Sweep Events



(II) Ejection Events

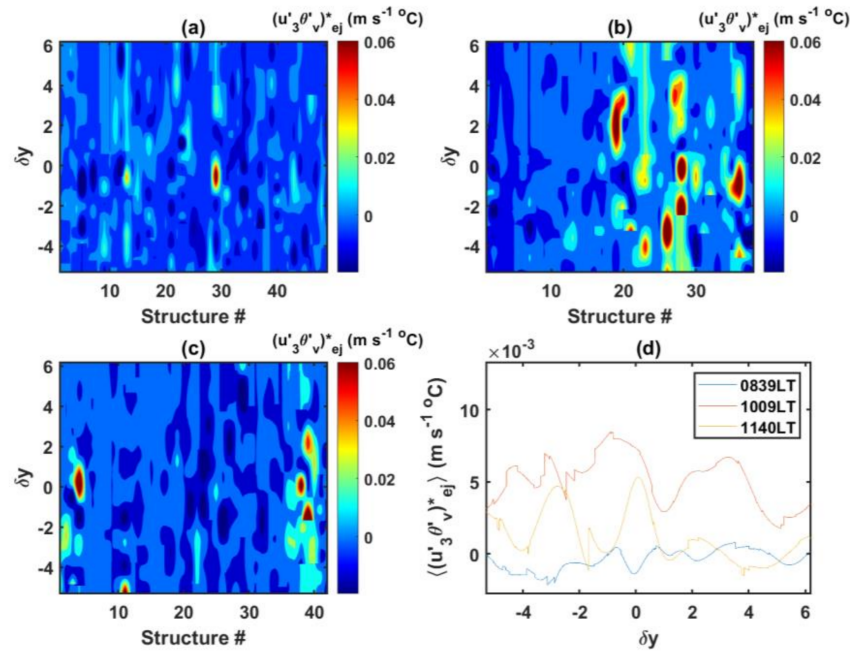
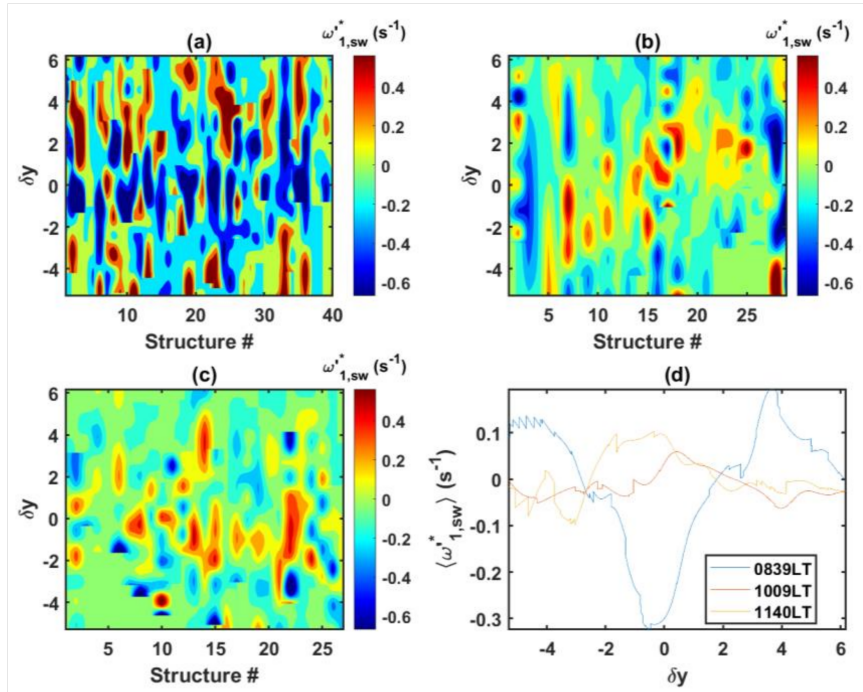


Figure 7.11 Heat flux sorted by sweep and ejection events during UKNRF campaign on August 17, 2022. (a) Isocontours of Flight 1, which started at 0839 LT; (b) Isocontours of Flight 2, which started at 1009 LT; (c) Isocontours of Flight 3, which started at 1140 LT and (d) mean profile of the conditionally averaged heat flux during the three flights.

also evident in the other vorticity fluctuation components, especially during ejection events. This is similar to what was observed in the heat flux, Fig. 7.9. Finally, the characterization of the average flow structure using conditional averaging tends to perform better (clearer trends can be extracted) under neutral conditions in the absence of buoyancy production.

(I) Sweep Events



(II) Ejection Events

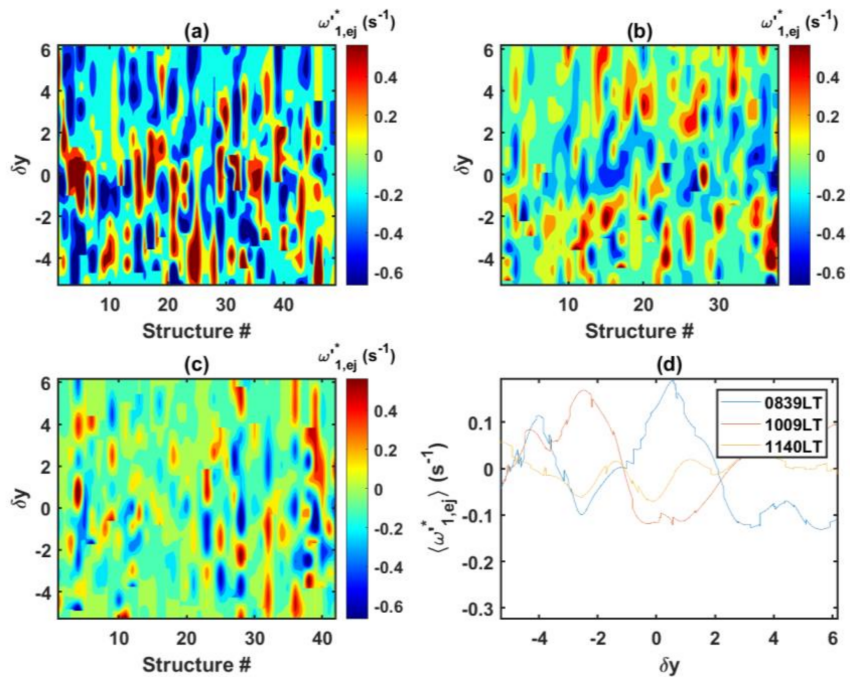


Figure 7.12 Streamwise vorticity fluctuations sorted by sweep and ejection events during UKNRF campaign on August 17, 2022. (a) Isocontours of Flight 1, which started at 0839 LT; (b) Isocontours of Flight 2, which started at 1009 LT; (c) Isocontours of Flight 3, which started at 1140 LT and (d) mean profile of the conditionally averaged streamwise vorticity fluctuations during the three flights.

Chapter 8 Conclusions and Future Work

Stationary (in-situ) measuring devices are commonly used to infer turbulence structure. However, this usually necessitates inferring the wind's spatial distribution using Taylor's frozen-flow hypothesis, which is poorly realized at large scales, particularly in non-stationary flows subject to the diurnal stability cycle. Multiple synchronous measuring systems at different sites are usually required to solve this limitation. On the other hand, uncrewed aircraft systems (UASs) are becoming more common in atmospheric research. UASs can travel through the flow on time scales quicker than coherent structures, resulting in improved spatial resolution of the turbulence structure along the flight path. Furthermore, UASs can obtain measurements with high spatial resolution while simultaneously sampling temporally because of their lower cruising speed compared to crewed aircraft. This study presents two approaches to studying the ABL structure during the morning transition.

The first approach employed three fixed-wing UASs each equipped with a single multi-hole probe for horizontal profiling with a fourth rotorcraft for vertical profiling to investigate the structure of the surface layer during the morning transition acquired as a part of the 2017 CLOUDMAP measurement campaign near Stillwater, Oklahoma, U.S.A. The second approach demonstrates the ability of a multi-hole-probe-based vorticity probe on fixed-wing UAS to characterize the ABL structure where we present an approach to estimate the local velocity gradients and employ them in the estimation of the dissipation rate and vorticity fields. Additionally, a

second fixed-wing UAS flying across the first UAS was used to estimate the advection velocity. Measurements were conducted with these aircraft during the morning transition during a limited field deployment campaign at the University of Kentucky North Research farm (UKNRF).

In the first approach, the analysis of single- and multi-point statistics conducted using fixed-wing and rotorcraft UASs flying simultaneously at different altitudes and flight paths demonstrated the potential for UAS to resolve coherent structures within the atmospheric surface layer. Generally, similar evolution was observed in the single-point statistics over the two cases measured, although decreased stability was present during Case 2, which resulted in significantly more influence of mechanical production for that case. The increased mechanical production corresponded to a reduction in temperature gradients and increased turbulence kinetic energy. Visualizations of the velocity and temperature fields connected these changes to a clear increase in the variability in both the vertical and horizontal fields. These visualizations also reflected the formation of turbulent thermals on the scale of hundreds of metres which became stronger as the morning evolved. Visualizations of the horizontal plane also appeared to indicate the presence of larger-scale motion. Application of spatio-temporal correlations to quasi-streamwise transects through the surface layer indicated that the structures have streamwise extent of approximately 200-m long, which grew with distance from the surface but reduced in streamwise scale over the course of the morning. Importantly, these spatio-temporal correlations provided a mean to measure the average advection velocity of the coherent structures. The results indicated the advection velocity was significantly lower than the mean velocity and only 20% to 50% of the

mean velocity. This ratio was time-dependent and increased with the increase in convective activity. One explanation for the presence of such low advection velocity is that the shear-driven structures may form locally (i.e., are ‘attached’ to the surface) potentially formed by local topography. This process is decoupled from the surface as the buoyant forcing increases.

By taking kinetic energy from the mean flow and transferring it to smaller scales in the form of more isotropic movements, coherent structures can operate as an intermediary in the inertial cascade process. Here, by isolating ejection and sweep events, we found that these structures contribute approximately 20% to 30% of overall turbulence kinetic energy, momentum, and sensible heat flux, with an increase observed during the course of the boundary-layer transition. This result is at the lower end of published estimates which have a broad range of suggested values ranging between 30% to 70%. It should be noted that these UAS measurements are only capable of resolving motions smaller than the transect length (approximately 1 km) and time-dependent fluctuations in the measured turbulence kinetic energy from each transect suggests that larger-scale motions (with time scales on the order of 30 minutes) were present. Thus, this low estimate of contributions could be due to the comparatively short transect length preventing filtering out the contribution of scales of motion larger than half the transect length.

Additionally, the spatio-temporal organization of the coherent motions was elucidated by employing a conditional-averaging process. Although the limited number of events captured resulted in weak statistical convergence, there was evidence of similarities between the structure of ejection events observed in the atmospheric surface layer, and

structures observed in canonical zero-pressure-gradient isothermal turbulent boundary layers. This organization weakened with increased buoyant forcing, but similarities did persist. Less organization was observed in the sweeping events, although there was evidence of splatting as the event reached the surface.

On the other hand, the results from the second approach highlight the ability of the vorticity probe to resolve the dissipation rate field during the UKNRF campaign despite the relatively large spatial separation in the probe design. The mean dissipation rate over the three flights estimated using the gradients of velocity fluctuations extracted from the vorticity probe measurements showed good agreement with the dissipation rates approximated using a combination of Kolmogorov theory and Taylor's frozen hypothesis. Moreover, the dissipation rate fields revealed the existence of intermittent and intense regions that are consistent with other observations in the literature and were related to coherent structures. Moreover, the flow fields of the potential temperature fluctuations have signatures on coherent structures with length scales in streamwise and spanwise directions on the order of 200 m for the early morning flight (Flight 1). As the morning progresses, the streamwise length scales increase up to 600 m where such scales could correspond either to low-momentum streaks or hairpin vortex legs. These streaks are known to evolve and form the legs of hairpin vortices which also could be what the UAS are detecting since the average flow fields of the heat flux and the vorticity fluctuation components show some common characteristics of hairpin vortices' legs. In the heat flux flow field, this is evident by negative/positive regions surrounded by positive/negative regions as a result of mixing events. Whereas, in the vorticity field, this is evident by intense vorticity

regions surrounded by two intense regions with counter vorticity direction. To conclude, we have demonstrated the ability of UASs to investigate the structure of the ABL through either a single multi-hole or by employing the vorticity probe.

8.1 Future Work

The current vorticity probe measurement system relies on a board of 12 pressure transducers that measure differential pressure. We believe that increasing the number of transducers to 20 and measuring the pressure of each whole instead of differential pressure will improve accuracy. It will also be highly beneficial to increase the resolved frequencies of the five-hole-probes to capture more of the inertial subrange. It was noted that when comparing the power spectrum obtained from a probe connected to 3 pressure transducers and another probe connected to 5 pressure transducers the frequency response improved, but it is unclear why. One possible explanation is that the current tubing of the vorticity probe is long, which increases the damping effects and reduces the ability of the probe to resolve higher frequencies hence reducing the length of these tubes would increase the ability of the probe to resolve higher frequencies. This could be accomplished by placing the transducers near the probes and connecting them to the conditional circuit, i.e., instead of long tubes, use long wires. Additionally, the use of several UASs, each equipped with a single multi-hole probe, simultaneously flying in a controlled formation along with another UAS equipped with a vorticity probe, could be carried out for measurements of large-scale velocity gradients. Finally, this vorticity probe could be used for Lagrangian coherent structure identification, a method shown to be effective in identifying coherent structures

in turbulent flows, particularly in the identification of transport barriers. Preliminary attempts at identifying these structures were unsuccessful, but we believe by refining the probe and its analysis, it should be possible to identify these structures from the UAS measurements.

Bibliography

- Abraham, A. and Hong, J. (2022). Characterization of atmospheric coherent structures and their impact on a utility-scale wind turbine. *Flow*, 2:E5.
- Adkins, K., Wambolt, P., Sescu, A., Swinford, C., and Macchiarella, N. D. (2020). Observational practices for urban microclimates using meteorologically instrumented unmanned aircraft systems. *Atmosphere*, 11(9).
- Adkins, K. A. and Sescu, A. (2017). Observations of relative humidity in the near-wake of a wind turbine using an instrumented unmanned aerial system. *International Journal of Green Energy*, 14(10):845–860.
- Adkins, K. A. and Sescu, A. (2018). Analysis of near-surface relative humidity in a wind turbine array boundary layer using an instrumented unmanned aerial system and large-eddy simulation. *Wind Energy*, 21(11):1155–1168.
- Adrian, R. C., Meinhart, C. D., and Tomkins, C. D. (2000). Vortex organization in the outer region of the turbulent boundary layer. *J Fluid Mech*, 422:1–54.
- Adrian, R. J. (2007). Hairpin vortex organization in wall turbulence. *Phys Fluids*, 19(4):041301.
- Al-Ghussain, L. and Bailey, S. C. C. (2021). An approach to minimize aircraft motion bias in multi-hole probe wind measurements made by small unmanned aerial systems. *Atmos Meas Tech*, 14(1):173–184.
- Al-Ghussain, L. and Bailey, S. C. C. (2022). Uncrewed aircraft system measurements of atmospheric surface-layer structure during morning transition. *Boundary-Layer Meteorology*, 185(2):229–258.
- Alcayaga, L., Larsen, G. C., Kelly, M., and Mann, J. (2020). Large-scale coherent structures in the atmosphere over a flat terrain. *Journal of Physics: Conference Series*, 1618(6).
- Alcayaga, L., Larsen, G. C., Kelly, M., and Mann, J. (2022). Large-scale coherent turbulence structures in the atmospheric boundary layer over flat terrain. *Journal of the Atmospheric Sciences*, 79(12):3219–3243.
- Andreopoulos, Y. and Honkan, A. (1996). Experimental techniques for highly resolved measurements of rotation, strain and dissipation-rate tensors in turbulent flows. *Measurement Science and Technology*, 7(10):1462–1476.
- Angevine, W. M. (2008). Transitional, entraining, cloudy, and coastal boundary layers. *Acta Geophysica*, 56(1):2–20.

- Angevine, W. M., Baltink, H. K., and Bosveld, F. C. (2001). Observations of the morning transition of the convective boundary layer. *Boundary-Layer Meteorol*, 101(2):209–227.
- Antonia Yonggang; Shafi, H. S., R. A. Z. (1996). Lateral vorticity measurements in a turbulent wake. *Journal of Fluid Mechanics*, 323(-1):173–200.
- Axford, D. N. (1968). On the accuracy of wind measurements using an inertial platform in an aircraft, and an example of a measurement of the vertical mesostructure of the atmosphere. *Journal of Applied Meteorology*, 7(4):645–666.
- Bailey, S. C. C., Canter, C. A., Sama, M. P., Houston, A. L., and Smith, S. W. (2019). Unmanned aerial vehicles reveal the impact of a total solar eclipse on the atmospheric surface layer. *Proceedings of the Royal Society A: Mathematical, Physical and Engineering Sciences*, 475(2229).
- Bailey, S. C. C., Hultmark, M., Smits, A. J., and Schultz, M. P. (2008). Azimuthal structure of turbulence in high Reynolds number pipe flow. *J Fluid Mech*, 615:121–138.
- Bailey, S. C. C., Sama, M. P., Canter, C. A., Pampolini, L. F., Lippay, Z. S., Schuyler, T. J., Hamilton, J. D., MacPhee, S. B., Rowe, I. S., Sanders, C. D., Smith, V. G., Vezzi, C. N., Wight, H. M., Hoagg, J. B., Guzman, M. I., and Smith, S. W. (2020). University of Kentucky measurements of wind, temperature, pressure and humidity in support of LAPSE-RATE using multisite fixed-wing and rotorcraft unmanned aerial systems. *Earth System Science Data*, 12(3):1759–1773.
- Bailey, S. C. C. and Smits, A. J. (2010). Experimental investigation of the structure of large- and very-large-scale motions in turbulent pipe flow. *J Fluid Mech*, 651:339–356.
- Balakumar, B. J. and Adrian, R. J. (2007). Large- and very-large-scale motions in channel and boundary-layer flows. *Phil. Trans. R. Soc. A*, 365:665–681.
- Balint James M.; Vukoslavcevic, Petar, J.-L. W. (1991). The velocity and vorticity vector fields of a turbulent boundary layer. Part 2. Statistical properties. *Journal of Fluid Mechanics Digital Archive*, 228(NA):53–86.
- Balsley, B. B., Lawrence, D. A., Woodman, R. F., and Fritts, D. C. (2013). Fine-scale characteristics of temperature, wind, and turbulence in the lower atmosphere (0–1, 300 m) over the South Peruvian coast. *Boundary-Layer Meteorol*, 147(1):165–178.
- Baltzer, J. R., Adrian, R. J., and Wu, X. (2013). Structural organization of large and very large scales in turbulent pipe flow simulation. *Journal of Fluid Mechanics*, 720(NA):236–279.
- Banakh, V. A., Smalikho, I. N., Köpp, F., and Werner, C. (1999). Measurements of turbulent energy dissipation rate with a CW Doppler lidar in the atmospheric boundary layer. *Journal of Atmospheric and Oceanic Technology*, 16(8):1044–1061.

- Bange, J., Spieß, T., and van den Kroonenberg, A. (2007). Characteristics of the early-morning shallow convective boundary layer from Helipod flights during STINHO-2. *Theor Appl Climatol*, 90(1-2):113–126.
- Banta, R. M., Pichugina, Y. L., and Brewer, W. A. (2006). Turbulent velocity-variance profiles in the stable boundary layer generated by a nocturnal low-level jet. *Journal of the Atmospheric Sciences*, 63(11):2700–2719.
- Barbieri, L., Kral, S. T., Bailey, S. C. C., Frazier, A. E., Jacob, J. D., Reuder, J., Brus, D., Chilson, P. B., Crick, C., Detweiler, C., Doddi, A., Elston, J., Foroutan, H., González-Rocha, J., Greene, B. R., Guzman, M. I., Houston, A. L., Islam, A., Kemppinen, O., Lawrence, D., Pillar-Little, E. A., Ross, S. D., Sama, M. P., Schmale, D. G., Schuyler, T. J., Shankar, A., Smith, S. W., Waugh, S., Dixon, C., Borenstein, S., and Boer, G. D. (2019). Intercomparison of small unmanned aircraft system (sUAS) measurements for atmospheric science during the LAPSE-RATE campaign. *Sensors (Switzerland)*, 19(9).
- Bärfuss, K., Pätzold, F., Altstädter, B., Kathe, E., Nowak, S., Bretschneider, L., Bestmann, U., and Lampert, A. (2018). New setup of the UAS ALADINA for measuring boundary layer properties, atmospheric particles and solar radiation. *Atmosphere*, 9(1):28.
- Barthlott, C., Drobinski, P., Fesquet, C., Dubos, T., and Pietras, C. (2007). Long-term study of coherent structures in the atmospheric surface layer. *Boundary-Layer Meteorology*, 125(1):1–24.
- Båserud, L., Reuder, J., Jonassen, M. O., Kral, S. T., Paskyabi, M. B., and Lothon, M. (2016). Proof of concept for turbulence measurements with the RPAS SUMO during the BLLAST campaign. *Atmospheric Measurement Techniques*, 9(10):4901–4913.
- Beare, R. J. (2008). The role of shear in the morning transition boundary layer. *Boundary-Layer Meteorol*, 129(3):395–410.
- Bennett, L. J., Weckwerth, T. M., Blyth, A. M., Geerts, B., Miao, Q., and Richardson, Y. P. (2010). Observations of the evolution of the nocturnal and convective boundary layers and the structure of open-celled convection on 14 june 2002. *Mon Weather Rev*, 138(7):2589–2607.
- Blackwelder, R. and Kaplan, R. (1976). On the wall structure of the turbulent boundary layer 76:89–112. *J Fluid Mech*, 76:89–112.
- Bodini, N., Lundquist, J. K., Krishnamurthy, R., Pekour, M., Berg, L. K., and Choukulkar, A. (2019). Spatial and temporal variability of turbulence dissipation rate in complex terrain. *Atmospheric Chemistry and Physics*, 19(7):4367–4382.

- Bodini, N., Lundquist, J. K., and Newsom, R. K. (2018). Estimation of turbulence dissipation rate and its variability from sonic anemometer and wind Doppler lidar during the XPIA field campaign. *Atmospheric Measurement Techniques*, 11(7):4291–4308.
- Boer, G. D., Waugh, S., Erwin, A., Borenstein, S., and Dixon, C. (2020). Measurements from mobile surface vehicles during LAPSE- RATE 5. *Earth System Science Data*, 3814765(August):1–28.
- Bonin, T., Chilson, P., Zielke, B., and Fedorovich, E. (2013). Observations of the early evening boundary-layer transition using a small unmanned aerial system. *Boundary-Layer Meteorol*, 146(1):119–132.
- Bonin, T. a., Chilson, P. B., Zielke, B. S., Klein, P. M., and Leeman, J. R. (2012). Development and comparisons of wind retrieval algorithms for small unmanned aerial systems. *Geoscientific Instrumentation, Methods and Data Systems Discussions*, 2:953–979.
- Boppe, R. S., Neu, W. L., and Shuai, H. (1999). Large-scale motions in the marine atmospheric surface layer. *Boundary-Layer Meteorol.*, 92:165–183.
- Brosy, C., Krampf, K., Zeeman, M., Wolf, B., Junkermann, W., Schäfer, K., Emeis, S., and Kunstmann, H. (2017). Simultaneous multicopter-based air sampling and sensing of meteorological variables. *Atmospheric Measurement Techniques*, 10(8):2773–2784.
- Brown, G. L. and Roshko, A. (1974). On density effects and large structure in turbulent mixing layers. *J Fluid Mech*, 64(4):775–816.
- Bruschi, P., Dei, M., and Piotto, M. (2009). A low-power 2-D wind sensor based on integrated flow meters. *IEEE Sensors Journal*, 9(12):1688–1696.
- Bruschi, P., Piotto, M., Dell’Agnello, F., Ware, J., and Roy, N. (2016). Wind speed and direction detection by means of solid-state anemometers embedded on small quadcopters. *Procedia Engineering*, 168:802–805.
- Calmer, R., Roberts, G. C., Preissler, J., Sanchez, K. J., Derrien, S., and O’Dowd, C. (2018). Vertical wind velocity measurements using a five-hole probe with remotely piloted aircraft to study aerosol-cloud interactions. *Atmospheric Measurement Techniques*, 11(5):2583–2599.
- Canter, C. A. (2019). Hot-wire anemometer measurements of atmospheric surface layer turbulence via unmanned aerial vehicle. Master’s thesis, University of Kentucky.
- Carper, M. and Porte-Agel, F. (2004). The role of coherent structures in subfilter-scale dissipation of turbulence measured in the atmospheric surface layer. *Journal of Turbulence*, 5.

- Cassano, J. J. (2014). Observations of atmospheric boundary layer temperature profiles with a small unmanned aerial vehicle. *Antarctic Science*, 26(2):205–213.
- Cassano, J. J., Maslanik, J. A., Zappa, C. J., Gordon, A. L., Cullather, R. I., and Knuth, S. L. (2010). Observations of Antarctic polynya with unmanned aircraft systems. *Eos, Transactions American Geophysical Union*, 91(28):245–246.
- Cassano, J. J., Seefeldt, M. W., Palo, S., Knuth, S. L., Bradley, A. C., Herrman, P. D., Kernebone, P. A., and Logan, N. J. (2016). Observations of the atmosphere and surface state over Terra Nova Bay, Antarctica, using unmanned aerial systems. *Earth System Science Data*, 8(1):115–126.
- Champagne, F. H. (1978). Fine-scale structure of turbulent velocity-field. *J Fluid Mech*, 86:67–108.
- Chauhan, K., Hutchins, N., Monty, J., and Marusic, I. (2013). Structure inclination angles in the convective atmospheric surface layer. *Boundary-Layer Meteorol*, 147(1):41–50.
- Chen Michael D.; Black, T. Andrew; Lee, Xuhui, W. N. (1997). Coherent eddies and temperature structure functions for three contrasting surfaces. Part I: Ramp model with finite microfront time. *Boundary-Layer Meteorology*, 84(1):99–124.
- Chiba, T., Haga, Y., Inoue, M., Kiguchi, O., Nagayoshi, T., Madokoro, H., and Morino, I. (2019). Measuring regional atmospheric CO_2 concentrations in the lower troposphere with a non-dispersive infrared analyzer mounted on a UAV, Ogata Village, Akita, Japan. *Atmosphere*, 10(9).
- Chilson, P. B., Bell, T. M., Brewster, K. A., Britto Hupsel de Azevedo, G., Carr, F. H., Carson, K., Doyle, W., Fiebrich, C. A., Greene, B. R., Grimsley, J. L., Kanneganti, S. T., Martin, J., Moore, A., Palmer, R. D., Pillar-Little, E. A., Salazar-Cerreno, J. L., Segales, A. R., Weber, M. E., Yeary, M., and Droegemeier, K. K. (2019). Moving towards a network of autonomous uas atmospheric profiling stations for observations in the earth’s lower atmosphere: The 3D mesonet concept. *Sensors*, 19(12).
- Chow, F., Schär, C., Ban, N., Lundquist, K., Schlemmer, L., and Shi, X. (2019). Crossing multiple gray zones in the transition from mesoscale to microscale simulation over complex terrain. *Atmosphere*, 10(5):274.
- Chu, Y., Li, J., Li, C., Tan, W., Su, T., and Li, J. (2019). Seasonal and diurnal variability of planetary boundary layer height in Beijing: Intercomparison between MPL and WRF results. *Atmospheric Research*, 227(July 2018):1–13.
- Cione, J., Kalina, E., Uhlhorn, E., Farber, A., and Damiano, B. (2016). Coyote unmanned aircraft system observations in hurricane Edouard (2014). *Earth and Space Science*, 3(9):370–380.

- Cione, J. J., Bryan, G. H., Dobosy, R., Zhang, J. A., de Boer, G., Aksoy, A., Wadler, J. B., Kalina, E. A., Dahl, B. A., Ryan, K., Neuhaus, J., Dumas, E., Marks, F. D., Farber, A. M., Hock, T., and Chen, X. (2020). Eye of the storm: Observing hurricanes with a small unmanned aircraft system. *Bulletin of the American Meteorological Society*, 101(2):E186–E205.
- Cook, D. E., Strong, P. A., Garrett, S. A., and Marshall, R. E. (2013). A small unmanned aerial system (UAS) for coastal atmospheric research: preliminary results from New Zealand. *Journal of the Royal Society of New Zealand*, 43(2):108–115.
- Corrigan, C., Roberts, G., Ramana, M., Kim, D., and Ramanathan, V. (2008). Capturing vertical profiles of aerosols and black carbon over the indian ocean using autonomous unmanned aerial vehicles. *Atmospheric Chem Phys*, 8(3):737–747.
- Curry, J. A., Maslanik, J., Holland, G., and Pinto, J. (2004). Applications of Aerosondes in the Arctic. *Bulletin of the American Meteorological Society*, 85(12):1855–1862.
- Cuxart, J., Wrenger, B., Matjacic, B., and Mahrt, L. (2019). Spatial variability of the lower atmospheric boundary layer over hilly terrain as observed with an RPAS. *Atmosphere*, 10(11):715.
- Daida, J., Russell, P., Crawford, T., and Vesecky, J. (1994). An unmanned aircraft vehicle system for boundary-layer flux measurements over forest canopies. In *Proceedings of IGARSS '94 - 1994 IEEE International Geoscience and Remote Sensing Symposium*, volume 2, pages 1248–1250. IEEE.
- de Boer, G., Calmer, R., Jozef, G., Cassano, J. J., Hamilton, J., Lawrence, D., Borenstein, S., Doddi, A., Cox, C., Schmale, J., Preußner, A., and Argrow, B. (2022). Observing the Central Arctic atmosphere and surface with University of Colorado uncrewed aircraft systems. *Scientific Data*, 9(1):439.
- de Boer, G., Ivey, M., Schmid, B., Lawrence, D., Dexheimer, D., Mei, F., Hubbe, J., Bendure, A., Hardesty, J., Shupe, M. D., McComiskey, A., Telg, H., Schmitt, C., Matrosov, S. Y., Brooks, I., Creamean, J., Solomon, A., Turner, D. D., Williams, C., Maahn, M., Argrow, B., Palo, S., Long, C. N., Gao, R.-S., and Mather, J. (2018). A bird’s-eye view: Development of an operational arm unmanned aerial capability for atmospheric research in arctic Alaska. *Bulletin of the American Meteorological Society*, 99(6):1197–1212.
- de Boisblanc, I., Dodbele, N., Kussmann, L., Mukherji, R., Chestnut, D., Phelps, S., Lewin, G. C., and de Wekker, S. (2014). Designing a hexacopter for the collection of atmospheric flow data. In *2014 Systems and Information Engineering Design Symposium (SIEDS)*, pages 147–152.
- Deardorff, J. W. (1980). Stratocumulus-capped mixed layers derived from a three-dimensional model. *Boundary-Layer Meteorol*, 18(4):495–527.

- Dennis, D. J. C. and Nickels, T. B. (2011). Experimental measurement of large-scale three-dimensional structures in a turbulent boundary layer. Part 2. Long structures. *Journal of Fluid Mechanics*, 673(NA):218–244.
- Dias Júnior, C., Sá, L., Pachêco, V., and de Souza, C. (2013). Coherent structures detected in the unstable atmospheric surface layer above the Amazon forest. *J Wind Eng Ind Aerodyn*, 115:1–8.
- Drobinski, P., Brown, R. a., Flamant, P. H., and Pelon, J. (1998). Evidence of organized large eddies by ground-based doppler lidar, sonic anemometer and sodar. *Boundary-Layer Meteorol*, 88(3):343–361.
- Drobinski, P., Carlotti, P., Newsom, R. K., Banta, R. M., Foster, R. C., and Redelsperger, J.-L. (2004). The structure of the near-neutral atmospheric surface layer. *J. Atmos. Sci.*, 61(6):699–714.
- Drüe, C. and Heinemann, G. (2013). A review and practical guide to in-flight calibration for aircraft turbulence sensors. *Journal of Atmospheric and Oceanic Technology*, 30(12):2820–2837.
- Eckelmann Stavros G.; Brodkey, Robert S.; Wallace, James M., H. N. (1977). Vorticity and turbulence production in pattern recognized turbulent flow structures. *Physics of Fluids*, 20(10):S225–NA.
- Eder, F., Serafimovich, A., and Foken, T. (2013). Coherent structures at a forest edge: Properties, coupling and impact of secondary circulations. *Boundary-Layer Meteorol*, 148(2):285–308.
- Egger, J., Bajrachaya, S., Heinrich, R., Kolb, P., Lämmlein, S., Mech, M., Reuder, J., Schäper, W., Shakya, P., Schween, J., and Wendt, H. (2002). Diurnal winds in the Himalayan Kali Gandaki valley. part iii: Remotely piloted aircraft soundings. *Mon Weather Rev*, 130(8):2042–2058.
- Elston, J., Argrow, B., Frew, E., Houston, A., and Straka, J. (2011). Evaluation of unmanned aircraft systems for severe storm sampling using hardware-in-the-loop simulations. *Journal of Aerospace Computing, Information, and Communication*, 8(9):269–294.
- Elston, J., Argrow, B., Stachura, M., Weibel, D., Lawrence, D., and Pope, D. (2015). Overview of small fixed-wing unmanned aircraft for meteorological sampling. *Journal of Atmospheric and Oceanic Technology*, 32(1):97–115.
- Engelbart, D. A. M., Kallistratova, M., and Kouznetsov, R. (2007). Determination of the turbulent fluxes of heat and momentum in the ABL by ground-based remote-sensing techniques (a Review). *Meteorologische Zeitschrift*, 16(4):325–335.
- Etling, D. and Brown, R. A. (1993). Roll vortices in the planetary boundary layer: A review. *Boundary-Layer Meteorol*, 65(3):215–248.

- Fairall, C. W., Markson, R., Schacher, G. E., and Davidson, K. L. (1980). An aircraft study of turbulence dissipation rate and temperature structure function in the unstable marine atmospheric boundary layer. *Boundary-Layer Meteorology*, 19(4):453–469.
- Feigenwinter, C. and Vogt, R. (2005). Detection and analysis of coherent structures in urban turbulence. *Theor. Appl. Climatol.*, 81:219–230.
- Foken, T. (2006). 50 years of the Monin-Obukhov similarity theory. *Boundary-Layer Meteorol.*, 119(3):431–447.
- Folz, A. and Wallace, J. M. (2010). Near-surface turbulence in the atmospheric boundary layer. *Physica D: Nonlinear Phenomena*, 239(14):1305–1317.
- Freestone, M. M. (1988). Vorticity measurement by a pressure probe. *Aeronautical Journal*, 92(911):29–35.
- Frehlich, R., Meillier, Y., Jensen, M. L., Balsley, B., and Sharman, R. (2006). Measurements of boundary layer profiles in an urban environment. *Journal of Applied Meteorology and Climatology*, 45(6):821–837.
- Freytag, C. (1978). Statistical properties of energy dissipation. *Boundary-Layer Meteorology*, 14(2):183–198.
- Froidevaux, M., Higgins, C. W., Simeonov, V., Ristori, P., Pardyjak, E., Serikov, I., Calhoun, R., van den Bergh, H., and Parlange, M. (2012). A Raman lidar to measure water vapor in the atmospheric boundary layer. *Adv Water Resour.*, 51:345–356.
- Galperin, B., Sukoriansky, S., and Anderson, P. S. (2007). On the critical Richardson number in stably stratified turbulence. *Atmospheric Science Letters*, 8(3):65–69.
- Ganapathisubramani, B., Longmire, E. K., and Marusic, I. (2003). Characteristics of vortex packets in turbulent boundary layers. *J Fluid Mech.*, 478:35–46.
- Gao, W., H., S. R., and Paw U, K. W. (1992). Conditional analysis of temperature and humidity microfronts and ejection/sweep motions within and above a deciduous forest. *Boundary-Layer Meteorol.*, 59:35–57.
- Gao, W., Shaw, R. H., and Paw U, K. T. (1989). Observation of organized structure in turbulent flow within and above a forest canopy. *Boundary-Layer Meteorol.*, 47(1-4):349–377.
- Garratt, J. R. (1994). Review: the atmospheric boundary layer. *Earth-Sci Rev.*, 37(1-2):89–134.
- Glasheen, K., Pinto, J., Steiner, M., and Frew, E. W. (2019). Experimental assessment of local weather forecasts for small unmanned aircraft flight. In *AIAA Scitech 2019 Forum*, Reston, Virginia. American Institute of Aeronautics and Astronautics.

- González-Rocha, J., De Wekker, S. F. J., Ross, S. D., and Woolsey, C. A. (2020). Wind profiling in the lower atmosphere from wind-induced perturbations to multicopter UAS. *Sensors*, 20(5):1341.
- Grachev, A. A., Andreas, E. L., Fairall, C. W., Guest, P. S., and Persson, P. O. G. (2013). The critical Richardson number and limits of applicability of local similarity theory in the stable boundary layer. *Boundary-Layer Meteorol*, 147(1):51–82.
- Greene, B. R. (2022). *Stable Atmospheric Boundary Layer Turbulence: Insights*. PhD thesis, UNIVERSITY OF OKLAHOMA.
- Gu, H. H., Wang, G. H., Zhu, W., and Zheng, X. J. (2019). Gusty wind disturbances and large-scale turbulent structures in the neutral atmospheric surface layer. *Sci China: Phys Mech Astron*, 62(11):1–7.
- Guala, M., Hommema, S. E., and Adrian, R. J. (2006). Large-scale and very-large-scale motions in turbulent pipe flow. *J Fluid Mech*, 554:521–542.
- Guimarães, P., Ye, J., Batista, C., Barbosa, R., Ribeiro, I., Medeiros, A., Zhao, T., Hwang, W.-C., Hung, H.-M., Souza, R., and T. Martin, S. (2020). Vertical profiles of atmospheric species concentrations and nighttime boundary layer structure in the dry season over an urban environment in Central Amazon collected by an unmanned aerial vehicle. *Atmosphere*, 11(12).
- Harun, Z. and Reda Lotfy, E. (2019). Generation, evolution, and characterization of turbulence coherent structures. *Turbulence and Related Phenomena*, 395(1):116–124.
- He, B., He, B., Diao, Y., Chen, C., and Xu, J. (2002). Vorticity measurements in complex 3-D flow in tangentially-fired furnaces. *Flow Measurement and Instrumentation*, 13(4):173–181.
- Head, M. R. and Bandyopadhyay, P. (1981). New aspects of turbulent boundary-layer structure. *J Fluid Mech*, 107:297–337.
- Heisel, M., Dasari, T., Liu, Y., Hong, J., Coletti, F., and Guala, M. (2018). The spatial structure of the logarithmic region in very-high-Reynolds-number rough wall turbulent boundary layers. *Journal of Fluid Mechanics*, 857(NA):704–747.
- Hemingway, B. L., Frazier, A. E., Elbing, B. R., and Jacob, J. D. (2020). High-resolution estimation and spatial interpolation of temperature structure in the atmospheric boundary layer using a small unmanned aircraft system. *Boundary-Layer Meteorology*, 175(3):397–416.
- Hernandez-Deckers, D. and Sherwood, S. C. (2016). A numerical investigation of cumulus thermals. *J Atmos Sci*, 73(10):4117–4136.

- Higgins, C. W., Wing, M. G., Kelley, J., Sayde, C., Burnett, J., and Holmes, H. A. (2018). A high resolution measurement of the morning ABL transition using distributed temperature sensing and an unmanned aircraft system. *Environ Fluid Mech*, 18(3):683–693.
- Hobbs, S., Dyer, D., Courault, D., Oliosio, A., Lagouarde, J.-P., Kerr, Y., Mcaneney, J., and Bonnefond, J. (2002). Surface layer profiles of air temperature and humidity measured from unmanned aircraft. *Agronomie*, 22(6):635–640.
- Hogan, R. J., Grant, A. L. M., Illingworth, A. J., Pearson, G. N., and O’Connor, E. J. (2009). Vertical velocity variance and skewness in clear and cloud-topped boundary layers as revealed by Doppler lidar. *Quarterly Journal of the Royal Meteorological Society*, 135(640):635–643.
- Hommema, S. E. and Adrian, R. J. (2003). Packet structure of surface eddies in the atmospheric boundary layer. *Boundary-Layer Meteorology*, 106(1):147–170.
- Honnert, R., Masson, V., Lac, C., and Nagel, T. (2021). A theoretical analysis of mixing length for atmospheric models from micro to large scales. *Front Earth Sci*, 8(January):1–15.
- Horiguchi, M., Hayashi, T., Adachi, A., and Onogi, S. (2012). Large-scale turbulence structures and their contributions to the momentum flux and turbulence in the near-neutral atmospheric boundary layer observed from a 213-m tall meteorological tower. *Boundary-Layer Meteorol*, 144(2):179–198.
- Houston, A. L., Argrow, B., Elston, J., Lahowetz, J., Frew, E. W., and Kennedy, P. C. (2012). The collaborative Colorado–Nebraska unmanned aircraft system experiment. *Bulletin of the American Meteorological Society*, 93(1):39–54.
- Huang, J., Cassiani, M., and Albertson, J. D. (2009). Analysis of coherent structures within the atmospheric boundary layer. *Boundary-Layer Meteorol*, 131(2):147–171.
- Hunt, J. C. and Morrison, J. F. (2000). Eddy structure in turbulent boundary layers. *European Journal of Mechanics, B/Fluids*, 19(5):673–694.
- Hussain, A. K. M. F. (1983). Coherent structures—reality and myth. *Physics of Fluids*, 26(10):2816.
- Hussain, A. K. M. F. (1986). Coherent structures and turbulence. *Journal of Fluid Mechanics*, 173:303–356.
- Hutchins, N., Hambleton, W. T., and Marusic, I. (2005). Inclined cross-stream stereo particle image velocimetry measurements in turbulent boundary layers. *J Fluid Mech*, 541:21–54.
- Hutchins, N. and Marusic, I. (2007). Evidence of very long meandering features in the logarithmic region of turbulent boundary layers. *J Fluid Mech*, 579:1–28.

- Hutchins, N., Nickels, T. B., Marusic, I., and Chong, M. S. (2009). Hot-wire spatial resolution issues in wall-bounded turbulence. *J Fluid Mech*, 635(-1):103–136.
- Inagaki, A., Castillo, M. C. L., Yamashita, Y., Kanda, M., and Takimoto, H. (2012). Large-eddy simulation of coherent flow structures within a cubical canopy. *Boundary-Layer Meteorol*, 142(2):207–222.
- Inagaki, A. and Kanda, M. (2010). Organized structure of active turbulence over an array of cubes within the logarithmic layer of atmospheric flow. *Boundary-Layer Meteorol.*, 135:209–228.
- Ingenhorst, C., Jacobs, G., Stöbel, L., Schelenz, R., and Juretzki, B. (2021). Method for airborne measurement of the spatial wind speed distribution above complex terrain. *Wind Energy Sci*, 6(2):427–440.
- Inoue, J. and Sato, K. (2022). Toward sustainable meteorological profiling in polar regions: Case studies using an inexpensive UAS on measuring lower boundary layers with quality of radiosondes. *Environmental Research*, 205(December 2021):112468.
- Iwai, H., Ishii, S., Tsunematsu, N., Mizutani, K., Murayama, Y., Itabe, T., Yamada, I., Matayoshi, N., Matsushima, D., Weiming, S., Yamazaki, T., and Iwasaki, T. (2008). Dual-Doppler lidar observation of horizontal convective rolls and near-surface streaks. *Geophys Res Lett*, 35(14):L14808.
- Jacob, J. D., Chilson, P. B., Houston, A. L., and Smith, S. W. (2018). Considerations for atmospheric measurements with small unmanned aircraft systems. *Atmosphere*, 9(7):1–16.
- Jayaraman, B. and Brasseur, J. G. (2021). Transition in atmospheric boundary layer turbulence structure from neutral to convective, and large-scale rolls. *Journal of Fluid Mechanics*, 913:1–31.
- Jiang, P., Yuan, J., Wu, K., Wang, L., and Xia, H. (2022). Turbulence detection in the atmospheric boundary layer using coherent doppler wind lidar and microwave radiometer. *Remote Sensing*, 14(12).
- Jiménez, J. (2011). Cascades in wall bounded turbulence. *Annu. Rev. Fluid Mech.*, 44:27–45.
- Jonassen, M. O., Ólafsson, H., Ágústsson, H., Rögnvaldsson, Ó., and Reuder, J. (2012). Improving high-resolution numerical weather simulations by assimilating data from an unmanned aerial system. *Monthly Weather Review*, 140(11):3734–3756.
- Jonassen, M. O., Tisler, P., Altstädter, B., Scholtz, A., Vihma, T., Lampert, A., König-Langlo, G., and Lüpkes, C. (2015). Application of remotely piloted aircraft systems in observing the atmospheric boundary layer over Antarctic sea ice in winter. *Polar Research*, 34(1):25651.

- Kalogiros, J. A. and Wang, Q. (2002). Calibration of a radome-differential GPS system on a twin otter research aircraft for turbulence measurements. *Journal of Atmospheric and Oceanic Technology*, 19(2):159–171.
- Kanda, M. (2006). Large-eddy simulations on the effects of surface geometry of building arrays on turbulent organized structures. *Boundary-Layer Meteorol.*, 118:151–168.
- Kantha, L. and Hocking, W. (2011). Dissipation rates of turbulence kinetic energy in the free atmosphere: MST radar and radiosondes. *Journal of Atmospheric and Solar-Terrestrial Physics*, 73(9):1043–1051.
- Kastrinakis Helmut; Willmarth, William W., E. G. E. (1979). Influence of the flow velocity on a Kovasznay type vorticity probe. *The Review of scientific instruments*, 50(6):759–767.
- Kelly, R. D. (1982). A single doppler radar study of horizontal-roll convection in a lake-effect snow storm. *J Atmos Sci*, 39(7):1521–1531.
- Kim, J. H. and Fiedler, H. E. (1989). Vorticity measurements in a turbulent mixing layer. In *Advances in Turbulence 2*, volume NA, pages 267–271. Springer Berlin Heidelberg, Berlin, Heidelberg.
- Kim, K. C. and Adrian, R. J. (1999). Very large-scale motion in the outer layer. *Phys. Fluids*, 11(2):417–422.
- Kim, S.-W. and Park, S.-U. (2003). Coherent structures near the surface in a strongly sheared convective boundary layer generated by large-eddy simulation. *Boundary-Layer Meteorol*, 106(1):35–60.
- Kistler, A. L. (1952). *The vorticity meter*. PhD thesis, The Johns Hopkins Univ.
- Klewicki, J. C., Metzger, M. M., Kelner, E., and Thurlow, E. M. (1995). Viscous sublayer flow visualizations at $R_\theta \approx 1500\ 000$. *Physics of Fluids*, 7(4):857–863.
- Kline, S. J., Reynolds, W. C., Schraub, F. A., and Runstadler, P. W. (1967). The structure of turbulent boundary layers. *J Fluid Mech*, 30(4):741–773.
- Knuth, S. L. and Cassano, J. J. (2014). Estimating sensible and latent heat fluxes using the integral method from in situ aircraft measurements. *Journal of Atmospheric and Oceanic Technology*, 31(9):1964–1981.
- Knuth, S. L., Cassano, J. J., Maslanik, J. A., Herrmann, P. D., Kernebone, P. A., Crocker, R. I., and Logan, N. J. (2013). Unmanned aircraft system measurements of the atmospheric boundary layer over Terra Nova Bay, Antarctica. *Earth System Science Data*, 5(1):57–69.
- Kolmogorov, A. N. (1941). The local structure of turbulence in incompressible viscous fluid for very large Reynolds numbers. *Dokl. Akad. Nauk SSSR*, 30:301–305.

- Kovaszny, L. G. (1954). Turbulence measurements. In Ladenburg, R. W., editor, *Physical Measurements in Gas Dynamics and Combustion*. Princeton Univ, Princeton.
- Kral, S., Reuder, J., Vihma, T., Suomi, I., O'Connor, E., Kouznetsov, R., Wrenger, B., Rautenberg, A., Urbancic, G., Jonassen, M., Båserud, L., Maronga, B., Mayer, S., Lorenz, T., Holtslag, A., Steeneveld, G.-J., Seidl, A., Müller, M., Lindenberg, C., Langohr, C., Voss, H., Bange, J., Hundhausen, M., Hilsheimer, P., and Schygulla, M. (2018). Innovative strategies for observations in the Arctic atmospheric boundary layer (ISOBAR)—the Hailuoto 2017 campaign. *Atmosphere*, 9(7):268.
- Krusche, N. and De Oliveira, A. P. (2004). Characterization of coherent structures in the atmospheric surface layer. *Boundary-Layer Meteorol*, 110(2):191–211.
- Kumar, A., Sarin, M. M., and Sudheer, A. K. (2008). Mineral and anthropogenic aerosols in Arabian Sea–atmospheric boundary layer: Sources and spatial variability. *Atmospheric Environment*, 42(21):5169–5181.
- Ladino, K. S., Sama, M. P., and Stanton, V. L. (2022). Development and calibration of pressure-temperature-humidity (PTH) probes for distributed atmospheric monitoring using unmanned aircraft systems. *Sensors*, 22(9).
- Lapworth, A. (2006). The morning transition of the nocturnal boundary layer. *Boundary-Layer Meteorol*, 119(3):501–526.
- Larouche, P. and Boyer-Villemaire, U. (2010). Suspended particulate matter in the St. Lawrence estuary and Gulf surface layer and development of a remote sensing algorithm. *Estuarine, Coastal and Shelf Science*, 90(4):241–249.
- Laurence, R. J. and Argrow, B. M. (2018). Development and flight test results of a small UAS distributed flush airdata system. *Journal of Atmospheric and Oceanic Technology*, 35(5):1127–1140.
- Lawrence, D. A. and Balsley, B. B. (2013). High-resolution atmospheric sensing of multiple atmospheric variables using the DataHawk small airborne measurement system. *Journal of Atmospheric and Oceanic Technology*, 30(10):2352–2366.
- Lee, J., Sung, H. J., and Krogstad, P. (2011). Direct numerical simulation of the turbulent boundary layer over a cube-roughened wall. *J Fluid Mech*, 669:397–431.
- Lee, J. H. (2017). Large-scale motions in turbulent boundary layers subjected to adverse pressure gradients. *J Fluid Mech*, 810:323–361.
- Leelőssy, Á., Molnár, F., Izsák, F., Havasi, Á., Lagzi, I., and Mészáros, R. (2014). Dispersion modeling of air pollutants in the atmosphere: a review. *Central Eur J Geosci*, 6(3):257–278.
- LeMone, M. A. (1973). The structure and dynamics of horizontal roll vortices in the planetary boundary layer. *Journal of the Atmospheric Sciences*, 30(6):1077–1091.

- Lenschow, D. (1972). *The measurement of air velocity and temperature using the NCAR Buffalo aircraft measuring system*. National Center for Atmospheric Research.
- Lenschow, D. and Johnson, W. (1968). Concurrent airplane and balloon measurements of atmospheric boundary layer structure over a forest. *J. Appl. Meteor.*, 7:79–89.
- Lenschow, D. H. (1970). Airplane measurements of planetary boundary layer structure. *Journal of Applied Meteorology*, 9(6):874–884.
- Leuenberger, D., Haefele, A., Omanovic, N., Fengler, M., Martucci, G., Calpini, B., Fuhrer, O., and Rossa, A. (2020). Improving high-impact numerical weather prediction with lidar and drone observations. *Bulletin of the American Meteorological Society*, 101(7):E1036–E1051.
- Li, D. and Bou-Zeid, E. (2011). Coherent structures and the dissimilarity of turbulent transport of momentum and scalars in the unstable atmospheric surface layer. *Boundary-Layer Meteorol*, 140(2):243–262.
- Li, Q., Zhi, L., and Hu, F. (2010). Boundary layer wind structure from observations on a 325m tower. *Journal of Wind Engineering and Industrial Aerodynamics*, 98(12):818–832.
- Li, X., Wang, G., and Zheng, X. (2021). Study of coherent structures and heat flux transportation under different stratification stability conditions in the atmospheric surface layer. *Phys Fluids*, 33(6):065113.
- Liu, F., Qian, H., Zheng, X., Zhang, L., and Liang, W. (2017). Numerical study on the urban ventilation in regulating microclimate and pollutant dispersion in urban street canyon: A case study of Nanjing New Region, China. *Atmosphere*, 8(9).
- Liu, H., Wang, G., and Zheng, X. (2019). Three-dimensional representation of large-scale structures based on observations in atmospheric surface layers. *Journal of Geophysical Research: Atmospheres*, 124(20):10753–10771.
- Liu, S. and Liang, X. Z. (2010). Observed diurnal cycle climatology of planetary boundary layer height. *J Clim*, 23(21):5790–5809.
- Lonardi, M., Pilz, C., Akansu, E. F., Dahlke, S., Egerer, U., Ehrlich, A., Griesche, H., Heymsfield, A. J., Kirbus, B., Schmitt, C. G., Shupe, M. D., Siebert, H., Wehner, B., and Wendisch, M. (2022). Tethered balloon-borne profile measurements of atmospheric properties in the cloudy atmospheric boundary layer over the Arctic sea ice during MOSAiC: Overview and first results. *Elementa: Science of the Anthropocene*, 10(1):1–19.
- Lotfy, E. R., Abbas, A. A., Zaki, S. A., and Harun, Z. (2019). Characteristics of turbulent coherent structures in atmospheric flow under different shear–buoyancy conditions. *Boundary-Layer Meteorol*, 173(1):115–141.

- Lotfy, E. R. and Harun, Z. (2018). Effect of atmospheric boundary layer stability on the inclination angle of turbulence coherent structures. *Environ Fluid Mech*, 18(3):637–659.
- Lothon, M., Lohou, F., Pino, D., Couvreux, F., Pardyjak, E., Reuder, J., Vilà-Guerau De Arellano, J., Durand, P., Hartogensis, O., Legain, D., et al. (2014). The BLLAST field experiment: boundary-layer late afternoon and sunset turbulence. *Atmospheric Chem Phys*, 14(20):10931–10960.
- Loxton, B., Abdulrahim, M., and Watkins, S. (2008). *An Investigation of Fixed and Rotary Wing MAV Flight in Replicated Atmospheric Turbulence*. American Institute of Aeronautics and Astronautics, Reston, Virginia.
- Lu, C.-H. and Fitzjarrald, D. R. (1994). Seasonal and diurnal variations of coherent structures over a deciduous forest. *Boundary-Layer Meteorol*, 69(1-2):43–69.
- Luce, H., Kantha, L., Hashiguchi, H., and Lawrence, D. (2019). Estimation of turbulence parameters in the lower troposphere from ShUREX (2016-2017) UAV data. *Atmosphere*, 10(7).
- Lundquist, J. K. and Bariteau, L. (2015). Dissipation of turbulence in the wake of a wind turbine. *Boundary-Layer Meteorology*, 154(2):229–241.
- Manninen, A. J., Marke, T., Tuononen, M., and O’Connor, E. J. (2018). Atmospheric boundary layer classification with Doppler lidar. *Journal of Geophysical Research: Atmospheres*, 123(15):8172–8189.
- Mansour, M., Kocer, G., Lenherr, C., Chokani, N., and Abhari, R. S. (2011). Seven-sensor fast-response probe for full-scale wind turbine flowfield measurements. *Journal of Engineering for Gas Turbines and Power*, 133(8).
- Marasli P.; Wallace, James M., B. N. (1993). A calibration technique for multiple-sensor hot-wire probes and its application to vorticity measurements in the wake of a circular cylinder. *Experiments in Fluids*, 15(3):209–218.
- Marusic, I., Mathis, R., and Hutchins, N. (2010). Predictive model for wall-bounded turbulent flow. *Science*, 329:193–196.
- Mayer, S., Jonassen, M., Sandvik, A., and Reuder, J. (2012). Atmospheric profiling with the UAS SUMO: a new perspective for the evaluation of fine-scale atmospheric models. *Meteorology and Atmospheric Physics*, 116(1–2):15–26.
- McCaffrey, K., Bianco, L., and Wilczak, J. M. (2017). Improved observations of turbulence dissipation rates from wind profiling radars. *Atmospheric Measurement Techniques*, 10(7):2595–2611.
- McFarquhar, G. M., Smith, E., Pillar-Little, E. A., Brewster, K., Chilson, P. B., Lee, T. R., Waugh, S., Yussouf, N., Wang, X., Xue, M., de Boer, G., Gibbs, J. A., Fiebrich, C., Baker, B., Brotzge, J., Carr, F., Christophersen, H., Fengler, M.,

- Hall, P., Hock, T., Houston, A., Huck, R., Jacob, J., Palmer, R., Quinn, P. K., Wagner, M., Zhang, Y. R., and Hawk, D. (2020). Current and future uses of UAS for improved forecasts/warnings and scientific studies. *Bulletin of the American Meteorological Society*, 101(8):E1322–E1328.
- Metzger, M. and Holmes, H. (2008). Time scales in the unstable atmospheric surface layer. *Boundary-Layer Meteorol*, 126(1):29–50.
- Moeng, C.-H. and Sullivan, P. P. (1994). A comparison of shear- and buoyancy-driven planetary boundary layer flows. *J Atmos Sci*, 51(7):999–1022.
- Mohan, M. and Siddiqui, T. A. (1998). Analysis of various schemes for the estimation of atmospheric stability classification. *Atmospheric Environment*, 32(21):3775–3781.
- Moin, P. (2009). Revisiting Taylor’s hypothesis. *J Fluid Mech*, 640:1–4.
- Molter, C. and Cheng, P. W. (2020). ANDroMeDA - A novel flying wind measurement system. *Journal of Physics: Conference Series*, 1618(3):032049.
- Monin, A. S. and Obukhov, A. M. (1959). Basic laws of turbulent mixing in the surface layer of the atmosphere. *Tr. Akad. Nauk SSSR Geophys. Inst.*, 24(151):163–187.
- Monty, J., Hutchins, N., Ng, H., Marusic, I., and Chong, M. (2009). A comparison of turbulent pipe, channel and boundary layer flows. *J Fluid Mech*, 632:431–442.
- Monty, J. P., Stewart, J. A., Williams, R. C., and Chong, M. (2007). Large-scale features in turbulent pipe and channel flows. *J Fluid Mech*, 589:147–156.
- Morshed, N., Venayagamoorthy, S., and Dasi, L. (2013). Intermittency and local dissipation scales under strong mean shear. *Phys. Fluids*, 25:011701.
- Muñoz-Esparza, D., Sharman, R. D., and Lundquist, J. K. (2018). Turbulence dissipation rate in the atmospheric boundary layer: Observations and WRF mesoscale modeling during the XPIA field campaign. *Monthly Weather Review*, 146(1):351–371.
- Nathan, B. J., Golston, L. M., O’Brien, A. S., Ross, K., Harrison, W. A., Tao, L., Lary, D. J., Johnson, D. R., Covington, A. N., Clark, N. N., and Zondlo, M. A. (2015). Near-field characterization of methane emission variability from a compressor station using a model aircraft. *Environmental Science & Technology*, 49(13):7896–7903.
- National Academies of Sciences; Engineering and Medicine (2018). *Thriving on Our Changing Planet: A Decadal Strategy for Earth Observation from Space*. The National Academies Press, Washington, DC.
- National Research Council (2007). *Earth Science and Applications from Space: National Imperatives for the Next Decade and Beyond*. The National Academies Press, Washington, DC.

- National Research Council (2009). *Observing Weather and Climate from the Ground Up: A Nationwide Network of Networks*. The National Academies Press, Washington, DC.
- Newsom, R., Calhoun, R., Ligon, D., and Allwine, J. (2008). Linearly organized turbulence structures observed over a suburban area by dual-Doppler lidar. *Boundary-Layer Meteorol*, 127(1):111–130.
- Nilsson, E., Lohou, F., Lothon, M., Pardyjak, E., Mahrt, L., and Darbieu, C. (2016). Turbulence kinetic energy budget during the afternoon transition – Part 1: Observed surface TKE budget and boundary layer description for 10 intensive observation period days. *Atmospheric Chem Phys*, 16(14):8849–8872.
- Nolan, P. J., Pinto, J., González-Rocha, J., Jensen, A., Vezzi, C. N., Bailey, S. C., de Boer, G., Diehl, C., Laurence, R., Powers, C. W., Foroutan, H., Ross, S. D., and Schmale, D. G. (2018). Coordinated unmanned aircraft system (UAS) and ground-based weather measurements to predict Lagrangian coherent structures (LCSs). *Sensors (Switzerland)*, 18(12).
- O’Connor, E. J., Illingworth, A. J., Brooks, I. M., Westbrook, C. D., Hogan, R. J., Davies, F., and Brooks, B. J. (2010). A method for estimating the turbulent kinetic energy dissipation rate from a vertically pointing Doppler lidar, and independent evaluation from balloon-borne in situ measurements. *Journal of Atmospheric and Oceanic Technology*, 27(10):1652–1664.
- Oke, T. R. (2002). *Boundary Layer Climates*. Routledge.
- Onley, S. P., Hartogensis, O., and Tong, C. (2016). Whirlwinds and hairpins in the atmospheric surface layer. *Journal of the Atmospheric Sciences*, 73(12):4927–4943.
- Palomaki, R. T., Rose, N. T., van den Bossche, M., Sherman, T. J., and De Wekker, S. F. J. (2017). Wind estimation in the lower atmosphere using multirotor aircraft. *Journal of Atmospheric and Oceanic Technology*, 34(5):1183–1191.
- Park, S. B., Gentine, P., Schneider, K., and Farge, M. (2016). Coherent structures in the boundary and cloud layers: Role of updrafts, subsiding shells, and environmental subsidence. *J Atmos Sci*, 73(4):1789–1814.
- Park, S.-R. and Wallace, J. M. (1993). The influence of instantaneous velocity gradients on turbulence properties measured with multi-sensor hot-wire probes. *Experiments in Fluids*, 16(1):17–26.
- Paw, U, K. T., Brunet, Y., Collineau, S., Shaw, R. H., Maitani, T., Qui, J., , and Hippi, L. (1992). On coherent structures in turbulence above and within agricultural plant canopies. *Agric. For. Meteorol.*, 61:55–68.
- Perret, L. and Patton, E. G. (2021). Stability influences on interscale transport of turbulent kinetic energy and Reynolds shear stress in atmospheric boundary layers interacting with a tall vegetation canopy. *J Fluid Mech*, 921:1–49.

- Petenko, I. V. and Bezverkhni, V. A. (1999). Temporal scales of convective coherent structures derived from sodar data. *Meteorology and Atmospheric Physics*, 71(1-2):105–116.
- Petzold, A., Hasselbach, J., Lauer, P., Baumann, R., Franke, K., Gurk, C., Schlager, H., and Weingartner, E. (2008). Experimental studies on particle emissions from cruising ship, their characteristic properties, transformation and atmospheric lifetime in the marine boundary layer. *Atmospheric Chemistry and Physics*, 8(9):2387–2403.
- Pieri, D., Diaz, J., Bland, G., Fladeland, M., Makel, D., Schwandner, F., Buongiorno, M., and Elston, J. (2017). Unmanned aerial technologies for observations at active volcanoes: Advances and prospects. In *AGU Fall Meeting Abstracts*, volume 2017, pages NH31A–0204.
- Pinto, J. O., O’Sullivan, D., Taylor, S., Elston, J., Baker, C. B., Hotz, D., Marshall, C., Jacob, J., Barfuss, K., Piguet, B., Roberts, G., Omanovic, N., Fengler, M., Jensen, A. A., Steiner, M., and Houston, A. L. (2021). The status and future of small uncrewed aircraft systems (UAS) in operational meteorology. *Bulletin of the American Meteorological Society*, 102(11):E2121 – E2136.
- Prior, E. M., Brumbelow, K., and Miller, G. R. (2020). Measurement of above-canopy meteorological profiles using unmanned aerial systems. *Hydrological Processes*, 34(3):865–867.
- Prudden, S., Fisher, A., Marino, M., Mohamed, A., Watkins, S., and Wild, G. (2018). Measuring wind with small unmanned aircraft systems. *Journal of Wind Engineering and Industrial Aerodynamics*, 176:197–210.
- Ramanathan, V., Ramana, M. V., Roberts, G., Kim, D., Corrigan, C., Chung, C., and Winker, D. (2007). Warming trends in Asia amplified by brown cloud solar absorption. *Nature*, 448(7153):575.
- Rautenberg, A., Graf, M. S., Wildmann, N., Platis, A., and Bange, J. (2018). Reviewing wind measurement approaches for fixed-wing unmanned aircraft. *Atmosphere*, 9(11):422.
- Reineman, B. D., Lenain, L., and Melville, W. K. (2016). The use of ship-launched fixed-wing UAVs for measuring the marine atmospheric boundary layer and ocean surface processes. *Journal of Atmospheric and Oceanic Technology*, 33(9):2029–2052.
- Reuder, J., Båserud, L., Jonassen, M. O., Kral, S. T., and Müller, M. (2016). Exploring the potential of the RPA system SUMO for multipurpose boundary-layer missions during the BLLAST campaign. *Atmospheric Measurement Techniques*, 9(6):2675–2688.

- Reuter, M., Bovensmann, H., Buchwitz, M., Borchardt, J., Krautwurst, S., Gerilowski, K., Lindauer, M., Kubistin, D., and Burrows, J. P. (2021). Development of a small unmanned aircraft system to derive CO_2 emissions of anthropogenic point sources. *Atmospheric Measurement Techniques*, 14(1):153–172.
- Roberts, G. C., Ramana, M. V., Corrigan, C., Kim, D., and Ramanathan, V. (2008). Simultaneous observations of aerosol-cloud-albedo interactions with three stacked unmanned aerial vehicles. *Proceedings of the National Academy of Sciences*, 105(21):7370–7375.
- Robinson, S. (1991). Coherent motions in the turbulent boundary layer. *Annu Rev Fluid Mech*, 23(1):601–639.
- Romps, D. M. and Charn, A. B. (2015). Sticky thermals: Evidence for a dominant balance between buoyancy and drag in cloud updrafts. *J Atmos Sci*, 72(8):2890–2901.
- Sadani, L. K. and Kulkarni, J. R. (2001). A study of coherent structures in the atmospheric surface layer over short and tall grass. *Boundary-Layer Meteorol*, 99(2):317–334.
- Salesky, S. T. and Anderson, W. (2018). Buoyancy effects on large-scale motions in convective atmospheric boundary layers: Implications for modulation of near-wall processes. *J Fluid Mech*, 856:135–168.
- Salesky, S. T., Chamecki, M., and Bou-Zeid, E. (2017). On the nature of the transition between roll and cellular organization in the convective boundary layer. *Boundary-Layer Meteorol*, 163(1):41–68.
- Samie, M., Aparece-Scutariu, V., Lavoie, P., Shin, D. H., and Pollard, A. (2022). Three-dimensional large-scale and very-large-scale coherent structures in a turbulent axisymmetric jet. *Journal of Fluid Mechanics*, 948:1–27.
- Schuyler, T. J., Bailey, S. C. C., and Guzman, M. I. (2019). Monitoring tropospheric gases with small unmanned aerial systems (sUAS) during the second CLOUDMAP flight campaign. *Atmosphere*, 10(8).
- Schuyler, T. J. and Guzman, M. I. (2017). Unmanned aerial systems for monitoring trace tropospheric gases. *Atmosphere*, 8(10):206.
- Segalini, A. and Alfredsson, P. (2012). Techniques for the eduction of coherent structures from flow measurements in the atmospheric boundary layer. *Boundary-Layer Meteorol.*, 143:433–450.
- Senocak, I., Ackerman, A. S., Kirkpatrick, M. P., and Stevens, D.E. Mansour, N. (2007). Study of near-surface models for large-eddy simulations of a neutrally stratified atmospheric boundary layer. *Boundary-Layer Meteorol.*, 124:405–424.

- Shevchenko, A. M., Berezin, D. R., Puzirev, L. N., Tarasov, A. Z., Kharitonov, A. M., and Shmakov, A. S. (2016). Multi-hole pressure probes to air data system for subsonic small-scale air vehicles. *AIP Conference Proceedings*, 1770.
- Shimura, T., Inoue, M., Tsujimoto, H., Sasaki, K., and Iguchi, M. (2018). Estimation of wind vector profile using a hexarotor unmanned aerial vehicle and its application to meteorological observation up to 1000 m above surface. *Journal of Atmospheric and Oceanic Technology*, 35(8):1621–1631.
- Shupe, M. D., Daniel, J. S., de Boer, G., Eloranta, E. W., Kollias, P., Long, C. N., Luke, E. P., Turner, D. D., and Verlinde, J. (2008). A focus on mixed-phase clouds. *Bulletin of the American Meteorological Society*, 89(10):1549–1562.
- Sikma, M., Ouwersloot, H., Pedruzo-Bagazgoitia, X., van Heerwaarden, C., and Vilà-Guerau de Arellano, J. (2018). Interactions between vegetation, atmospheric turbulence and clouds under a wide range of background wind conditions. *Agric For Meteorol*, 255:31–43.
- Simon, N., Piqué, A., Snyder, D., Ikuma, K., Majumdar, A., and Hultmark, M. (2022). Fast-response hot-wire flow sensors for wind and gust estimation on UAVs. *Measurement Science and Technology*.
- Spieß, T., Bange, J., Buschmann, M., and Vörsmann, P. (2007). First application of the meteorological Mini-UAV 'M2AV'. *Meteorologische Zeitschrift*, 16(2):159–169.
- Su, T., Li, Z., and Kahn, R. (2020). A new method to retrieve the diurnal variability of planetary boundary layer height from lidar under different thermodynamic stability conditions. *Remote Sens Environ*, 237(November 2019):111519.
- Suomi, I. and Vihma, T. (2018). Wind gust measurement techniques—From traditional anemometry to new possibilities. *Sensors (Switzerland)*, 18(4):1–27.
- Takimoto, H., Sato, A., Barlow, J. F., Moriwaki, R., Inagaki, A., Onomura, S., and Kanda, M. (2011). Particle image velocimetry measurements of turbulent flow within outdoor and indoor urban scale models and flushing motions in urban canopy layers. *Boundary-Layer Meteorol*, 140(2):295–314.
- Thielicke, W., Hübert, W., Müller, U., Eggert, M., and Wilhelm, P. (2021). Towards accurate and practical drone-based wind measurements with an ultrasonic anemometer. *Atmospheric Measurement Techniques*, 14(2):1303–1318.
- Thomas, C. and Foken, T. (2007). Organised motion in a tall spruce canopy: Temporal scales, structure spacing and terrain effects. *Boundary-Layer Meteorol*, 122(1):123–147.
- Thomas, R. M., Lehmann, K., Nguyen, H., Jackson, D. L., Wolfe, D., and Ramanathan, V. (2012). Measurement of turbulent water vapor fluxes using a lightweight unmanned aerial vehicle system. *Atmos. Meas. Tech*, 5:5529–5568.

- Tian, L., Song, Y., Zhao, N., Shen, W., Wang, T., and Zhu, C. (2020). Numerical investigations into the idealized diurnal cycle of atmospheric boundary layer and its impact on wind turbine’s power performance. *Renewable Energy*, 145:419–427.
- Tomkins, C. D. and Adrian, R. J. (2003). Spanwise structure and scale growth in turbulent boundary layers. *J Fluid Mech*, 490:37–74.
- Tomkins, C. D. and Adrian, R. J. (2005). Energetic spanwise modes in the logarithmic layer of a turbulent boundary layer. *J Fluid Mech*, 545:141–162.
- Townsend, A. A. (1976). *The Structure of Turbulent Shear Flow*. Cambridge University Press, Cambridge, UK.
- Träumner, K., Damian, T., Stawiarski, C., and Wieser, A. (2015). Turbulent structures and coherence in the atmospheric surface layer. *Boundary-Layer Meteorol*, 154(1):1–25.
- Treaster, A. L. and Yocum, A. M. (1978). The calibration and application of five-hole probes. Technical report, DTIC Document.
- Tsinober Eliezer; Dracos, T., A. K. (1992). Experimental investigation of the field of velocity gradients in turbulent flows. *Journal of Fluid Mechanics*, 242(-1):169–192.
- Tuononen, M., O’Connor, E. J., Sinclair, V. A., and Vakkari, V. (2017). Low-level jets over Utö, Finland, based on Doppler lidar observations. *Journal of Applied Meteorology and Climatology*, 56(9):2577–2594.
- Valdecabres, L., Friedrichs, W., Von Bremen, L., and Kühn, M. (2016). Spatial-temporal analysis of coherent offshore wind field structures measured by scanning Doppler-lidar. *Journal of Physics: Conference Series*, 753(7).
- van den Kroonenberg, A., Martin, T., Buschmann, M., Bange, J., and Vörsmann, P. (2008). Measuring the wind vector using the autonomous mini aerial vehicle M²AV. *J. Atmos. Oceanic Technol.*, 25:1969–1982.
- van den Kroonenberg, A., Spieß, T., Buschmann, M., Martin, T., Anderson, P., Beyrich, F., and Bange, J. (2007). Boundary layer measurements with the autonomous mini-UAV M²AV. In *Proceedings of DACH2007*, Hamburg, Germany.
- Vasiljević, N., Harris, M., Tegtmeier Pedersen, A., Rolighed Thorsen, G., Pitter, M., Harris, J., Bajpai, K., and Courtney, M. (2020). Wind sensing with drone-mounted wind lidars: proof of concept. *Atmospheric Measurement Techniques*, 13(2):521–536.
- Vinković, K., Andersen, T., de Vries, M., Kers, B., van Heuven, S., Peters, W., Hensen, A., van den Bulk, P., and Chen, H. (2022). Evaluating the use of an Unmanned Aerial Vehicle (UAV)-based active AirCore system to quantify methane emissions from dairy cows. *Science of the Total Environment*, 831(November 2021).

- Vukoslavčević, P., Wallace, J. M., and Balint, J. L. (1991). The velocity and vorticity vector fields of a turbulent boundary layer. Part 1. Simultaneous measurement by hot-wire anemometry. *Journal of Fluid Mechanics*, 228:25–51.
- Vukoslavčević James M., P. W. (1981). Influence of velocity gradients on measurements of velocity and streamwise vorticity with hot-wire X-array probes. *Review of Scientific Instruments*, 52(6):869–879.
- Vukoslavcevic James M., P. W. (1996). A 12-sensor hot-wire probe to measure the velocity and vorticity vectors in turbulent flow. *Measurement Science and Technology*, 7(10):1451–1461.
- Waclawczyk, M., Ma, Y.-F., Kopeć, J. M., and Malinowski, S. P. (2017). Novel approaches to estimating the turbulent kinetic energy dissipation rate from low- and moderate-resolution velocity fluctuation time series. *Atmospheric Measurement Techniques*, 10(12):4573–4585.
- Wainwright, C. E., Bonin, T. A., Chilson, P. B., Gibbs, J. A., Fedorovich, E., and Palmer, R. D. (2015). Methods for evaluating the temperature structure-function parameter using unmanned aerial systems and large-eddy simulation. *Boundary-Layer Meteorology*, 155(2):189–208.
- Wallace John F., J. M. F. (1995). The measurement of vorticity in turbulent flows. *Annual Review of Fluid Mechanics*, 27(1):469–514.
- Wang, G., Yang, F., Wu, K., Ma, Y., Peng, C., Liu, T., and Wang, L. P. (2021). Estimation of the dissipation rate of turbulent kinetic energy: A review. *Chemical Engineering Science*, 229.
- Wang, S., Garcia, M., Bauer-Gottwein, P., Jakobsen, J., Zarco-Tejada, P. J., Bandini, F., Paz, V. S., and Ibrom, A. (2019). High spatial resolution monitoring land surface energy, water and CO_2 fluxes from an unmanned aerial system. *Remote Sensing of Environment*, 229:14–31.
- Watkins, A., Thompson, M., Shortis, M., Segal, R., Abdulrahim, M., and Sheridan, J. (2010). An overview of experiments on the dynamic sensitivity of MAVs to turbulence. *The Aeronautical Journal*, 114(1158):485–492.
- Weckwerth, T. M., Horst, T. W., and Wilson, J. W. (1999). An observational study of the evolution of horizontal convective rolls. *Mon Weather Rev*, 127(9):2160–2179.
- Weckwerth, T. M., Wilson, J. W., Wakimoto, R. M., and Crook, N. A. (1997). Horizontal convective rolls: Determining the environmental conditions supporting their existence and characteristics. *Mon Weather Rev*, 125(4):505–526.
- Wilczak, J. M. (1984). Large-scale eddies in the unstably stratified atmospheric surface layer. Part I: Velocity and temperature structure. *J. Atmos. Sci.*, 41:3537–3550.

- Wilczak, J. M., Gossard, E. E., Neff, W. D., and Eberhard, W. L. (1996). Ground-based remote sensing of the atmospheric boundary layer: 25 years of progress. *Boundary-Layer Meteorology*, 78(3):321–349.
- Wildmann, N., Rau, G. A., and Bange, J. (2015). Observations of the early morning boundary-layer transition with small remotely-piloted aircraft. *Boundary-Layer Meteorol*, 157(3):345–373.
- Wildmann Nicola; Lundquist, Julie K.; Bariteau, Ludovic; Wagner, Johannes, N. B. (2019). Estimation of turbulence dissipation rate from Doppler wind lidars and in situ instrumentation for the Perdigão 2017 campaign. *Atmospheric Measurement Techniques*, 12(12):6401–6423.
- Willmarth, W. and Lu, S. (1972). Structure of the Reynolds stress near the wall. *J Fluid Mech*, 55:65–92.
- Wilson, J. D., Flesch, T. K., and Bourdin, P. (2010). Ground-to-air gas emission rate inferred from measured concentration rise within a disturbed atmospheric surface layer. *Journal of Applied Meteorology and Climatology*, 49(9):1818–1830.
- Witte, B. M., Singler, R. F., and Bailey, S. C. (2017). Development of an unmanned aerial vehicle for the measurement of turbulence in the atmospheric boundary layer. *Atmosphere*, 8(10):195.
- Wolf, C. A., Hardis, R. P., Woodrum, S. D., Galan, R. S., Wichelt, H. S., Metzger, M. C., Bezzo, N., Lewin, G. C., and De Wekker, S. F. (2017). Wind data collection techniques on a multi-rotor platform. *2017 Systems and Information Engineering Design Symposium, SIEDS 2017*, pages 32–37.
- Wolfe, D. E. and Lataitis, R. J. (2018). Boulder atmospheric observatory: 1977–2016: The end of an era and lessons learned. *Bulletin of the American Meteorological Society*, 99(7):1345–1358.
- Wood, R. (2012). Stratocumulus clouds. *Mon Weather Rev*, 140(8):2373–2423.
- Worth, N. A. and Nickels, T. B. (2011). Time-resolved volumetric measurement of fine-scale coherent structures in turbulence. *Phys. Rev. E*, 84:025301.
- Wyngaard, J. C. (1969). Spatial resolution of the vorticity meter and other hot-wire arrays. *Journal of Physics E: Scientific Instruments*, 2(11):983–987.
- Wyngaard, J. C. (2010). *Turbulence in the Atmosphere*. Cambridge University Press, Cambridge.
- Zhou, S., Peng, S., Wang, M., Shen, A., and Liu, Z. (2018). The characteristics and contributing factors of air pollution in Nanjing: A case study based on an unmanned aerial vehicle experiment and multiple datasets. *Atmosphere*, 9(9).

Vita

Loiy Al-Ghussain

Place of Birth:

- Amman, Jordan

Education:

- University of Kentucky, Lexington, KY
Ph.D. in Mechanical Engineering, Apr. 2023 (expected)
- Middle East Technical University Northern Cyprus Campus, Guzelyurt, Northern Cyprus
M.Sc. in Sustainable Environment and Energy Systems, Jun. 2017
- University of Jordan, Amman, Jordan
B.Sc. in Mechanical Engineering, August 2015

Professional Positions:

- Graduate Intern, National Renewable Energy Laboratory September 2022–April 2023
- Graduate Research Assistant, University of Kentucky August 2020–April 2023
- Graduate Teaching Assistant, University of Kentucky August 2019–August 2020
- Graduate Research Assistant, German Jordanian University October 2017–August 2019

- Graduate Teaching Assistant, Middle East Technical University Northern Cyprus
Campus January 2016–June 2017

Publications:

- S. C.C. Bailey, S.W. Smith, M.P. Sama, L. Al-Ghussain and G.de Boer. Shallow katabatic flow in a complex valley: An observational case study leveraging uncrewed aircraft systems. *Boundary-Layer Meteorol*, 186, 399–422 (2023). <https://doi.org/10.1007/s10546-022-00783-w>.
- L. Al-Ghussain et al. Techno-economic assessment of photovoltaic-based charging stations for electric vehicles in developing countries. *Energy Sources, Part A Recover. Util. Environ. Eff.*, vol. 45, no. 1, pp. 523–541, 2023, doi: 10.1080/15567036.2023.2171517.
- L. Al-Ghussain, A. D. Ahmad, A. M. Abubaker, K. Hovi, M. A. Hassan, and A. Annuk. Techno-economic feasibility of hybrid PV/wind/battery/thermal storage trigeneration system: Toward 100% energy independency and green hydrogen production. *Energy Reports*, vol. 9, pp. 752–772, 2023.
- M. A. Hassan et al. Internally shielded receivers for parabolic trough solar concentrators operating with supercritical carbon dioxide: Analytical assessment. *Energy Convers. Manag.*, vol. 280, p. 116789, Mar. 2023, doi: 10.1016/j.enconman.2023.116789.
- L. Al-Ghussain, M. A. Hassan, and A. Hamed. Modeling and techno-economic optimization of overhead panels and reflectors in near-wall mounted PV systems. *Sol. Energy*, vol. 249, pp. 624–641, 2023.
- L. Al-Ghussain, O. Taylan, M. Abujubbeh, and M. A. Hassan. Optimizing the orientation of solar photovoltaic systems considering the effects of irradiation and cell temperature models with dust accumulation. *Sol. Energy*, vol. 249, pp. 67–80, 2023, doi: 10.1016/j.solener.2022.11.029.
- S. Al-Dahidi, J. Adeeb, O. Ayadi, M. Alrbai, and L. Al-Ghussain. A feature transformation and extraction approach-based artificial neural network for an improved production prediction of grid-connected solar photovoltaic systems. *Energy Sources, Part A Recover. Util. Environ. Eff.*, vol. 44, no. 4, pp. 9232–9254, Dec. 2022, doi: 10.1080/15567036.2022.2128475.
- M. Alrbai et al. Effect of hydrogen sulfide content on the combustion characteristics of biogas fuel in homogenous charge compression ignition engines. *Case Stud. Therm. Eng.*, vol. 40, p. 102509, 2022.
- A. Hamed, L. Al-Ghussain, M. A. Hassan, and A. Annuk. Techno-economic analysis for optimal configurations of PV systems with back reflectors. *Energy Reports*, vol. 8, pp. 14979–14996, 2022, doi: 10.1016/j.egyr.2022.11.053.
- L. Al-Ghussain, A. Darwish Ahmad, A. M. Abubaker, M. A. Mohamed, M. A. Hassan, and N. K. Akafuah. Optimal sizing of country-scale renewable energy systems towards green transportation sector in developing countries. *Case Stud. Therm. Eng.*, vol. 39, p. 102442, Nov. 2022, doi: 10.1016/j.csite.2022.102442.

- Z. Li et al. A fast current relaying algorithm for distribution systems based on discrete setting value. *Energy Reports*, vol. 8, pp. 11088–11100, Nov. 2022, doi: 10.1016/j.egy.2022.08.232.
- M. Alrbai et al. Techno-economic analysis of a solar-powered humidification-dehumidification desalination system under fogging effect. *Sustain. Energy Technol. Assessments*, vol. 53, p. 102752, Oct. 2022.
- L. Al-Ghussain and S.C.C Bailey. Uncrewed Aircraft System Measurements of Atmospheric Surface-Layer Structure During Morning Transition. *Boundary-Layer Meteorol*, 185, 229–258 (2022). <https://doi.org/10.1007/s10546-022-00729-2>.
- L. Al-Ghussain, A. Darwish Ahmad, A. M. Abubaker, and M. A. Hassan. Exploring the feasibility of green hydrogen production using excess energy from a country-scale 100% solar-wind renewable energy system. *Int. J. Hydrogen Energy*, vol. 47, no. 51, pp. 21613–21633, Jun. 2022.
- M. Alrbai, A. M. Abubaker, A. Darwish Ahmad, S. Al-Dahidi, O. Ayadi, D. Hjouj, L. Al-Ghussain. Optimization of energy production from biogas fuel in a closed landfill using artificial neural networks: A case study of Al Ghabawi Landfill, Jordan. *Waste Manag.*, vol. 150, no. June, pp. 218–226, Aug. 2022, doi: 10.1016/j.wasman.2022.07.011.
- M. A. Hassan, L. Al-Ghussain, A. Khalil, and S. A. Kaseb. Self-calibrated hybrid weather forecasters for solar thermal and photovoltaic power plants. *Renew. Energy*, vol. 188, pp. 1120–1140.
- L. Al-Ghussain, A. Darwish Ahmad, A. M. Abubaker, and M. A. Hassan. Techno-economic feasibility of thermal storage systems for the transition to 100% renewable grids. *Renew. Energy*, vol. 189, pp. 800–812, Apr. 2022, doi: 10.1016/j.renene.2022.03.054.
- L. Al-Ghussain, M. A. Subaih, and A. Annuk. Evaluation of the Accuracy of Different PV Estimation Models and the Effect of Dust Cleaning: Case Study a 103 MW PV Plant in Jordan. *Sustainability*, 14(2), Jan. 2022. <https://doi.org/10.3390/su14020982>.
- M. A. Hassan, L. Al-Ghussain, A. D. Ahmad, A. M. Abubaker, and A. Khalil. Aggregated independent forecasters of half-hourly global horizontal irradiance. *Renewable Energy*, 181, 365–383, Jan. 2022. doi: 10.1016/j.renene.2021.09.060.
- L. Al-Ghussain and S. C. C. Bailey. An approach to minimize aircraft motion bias in multi-hole probe wind measurements made by small unmanned aerial systems. *Atmos. Meas. Tech.*, 14 (1) 173–184, (2021). doi: 10.5194/amt-14-173-2021.
- L. Al-Ghussain, A. Darwish Ahmad, A. M. Abubaker, and M. A. Mohamed. An integrated photovoltaic/wind/biomass and hybrid energy storage systems towards 100% renewable energy microgrids in university campuses. *Sustain. Energy Technol. Assessments*, vol. 46, p. 101273, Aug. 2021.
- L. Al-Ghussain, A. D. Ahmad, A. M. Abubaker, M. Abujobbeh, A. Almalag, and M. A. Mohamed (2021). A Demand-Supply Matching-Based Approach for Mapping Renewable Resources towards 10% Renewable Grids in 2050. *IEEE Access*, 9, 58634–58651. <https://doi.org/10.1109/ACCESS.2021.3072969>.

- L. Al-Ghussain, A. M. Abubaker, and A. Darwish Ahmad. Superposition of Renewable-Energy Supply from Multiple Sites Maximizes Demand-Matching: Towards 100% Renewable Grids in 2050. *Appl. Energy*, vol. 284, no. September 2020, p. 116402, Feb. 2021, doi: 10.1016/j.apenergy.2020.116402.
- T. Lan, K. Jermsittiparsert, S. T. Alrashood, M. Rezaei, L. Al-Ghussain, M. A. Mohamed. An Advanced Machine Learning Based Energy Management of Renewable Microgrids Considering Hybrid Electric Vehicles' Charging Demand. *Energies*, vol. 14, no. 3, 2021, doi: 10.3390/en14030569.
- A. Al-Halhouli, L. Al-Ghussain, O. Khallouf, A. Rabadi, J. Alawadi, H. Liu, K. Al Oweidat, F. Chen, D. Zheng. Clinical Evaluation of Respiratory Rate Measurements on COPD (Male) Patients Using Wearable Inkjet-Printed Sensor. *Sensors*, vol. 21, no. 2, 2021, doi: 10.3390/s21020468.
- L. Al-Ghussain, O. Al-Oran, F. Lezsovits. Statistical Estimation Of Hourly Diffuse Radiation Intensity Of Budapest City. *Environ. Prog. Sustain. Energy*, Jul. 2020, doi: 10.1002/ep.13464.
- L. Al-Ghussain, R. Samu, O. Taylan, M. Fahrioglu, M. Fahrioghlu, and O. Taylan. Techno-Economic Comparative Analysis of Renewable Energy Systems: Case Study in Zimbabwe. *Inventions*, vol. 5, no. 3, p. 27, Jul. 2020, doi: 10.3390/inventions5030027.
- J. Abu-khalaf, L. Al-Ghussain, A. Nadi, and A. Al-Halhouli. Conductivity and Stretchability of Inkjet-Printed Silver Nanoparticle Patterns: Effect of the Number of Printed Layers. *Int. J. Mech. Eng. Robot. Res.*, vol. 9, no. 4, pp. 528–534, 2020, doi: 10.18178/ijmerr.9.4.528-534.
- L. Al-Ghussain, R. Samu, O. Taylan, and M. Fahrioglu. Sizing Renewable Energy Systems With Energy Storage Systems in Microgrids For Maximum Cost-Efficient Utilization of Renewable Energy Resources. *Sustain. Cities Soc.*, vol. 55, p. 102059, Jan. 2020, doi: 10.1016/j.scs.2020.102059.
- A. Al-Halhouli, L. Al-Ghussain, S. El Bouri, F. Habash, H. Liu, and D. Zheng. Clinical Evaluation of Stretchable and Wearable Inkjet-Printed Strain Gauge Sensor for Respiratory Rate Monitoring at Different Body Postures. *Appl. Sci.*, vol. 10, no. 2, p. 480, Jan. 2020, doi: 10.3390/app10020480.
- A. Al-Halhouli, L. Al-Ghussain, S. El Bouri, H. Liu, and D. Zheng. Clinical evaluation of stretchable and wearable inkjet-printed strain gauge sensor for respiratory rate monitoring at different measurements locations. *J. Clin. Monit. Comput.*, vol. 35, no. 3, pp. 453–462, 2021, doi: 10.1007/s10877-020-00481-3.
- L. Al-Ghussain et al. 100% Renewable Energy Grid for Rural Electrification of Remote Areas: A Case Study in Jordan. *Energies*, vol. 13, p. 4908, 2020.
- A. Al-Halhouli, L. Al-Ghussain, S. El Bouri, H. Liu, and D. Zheng. Fabrication and Evaluation of a Novel Non-Invasive Stretchable and Wearable Respiratory Rate Sensor Based on Silver Nanoparticles Using Inkjet Printing Technology. *Polymers (Basel)*, vol. 11, no. 9, p. 1518, Sep. 2019, doi: 10.3390/polym11091518.
- J. Abu-Khalaf, L. Al-Ghussain, A. Nadi, R. Saraireh, A. Rabayah, S. Altarazi, A. Al-Halhouli. Optimization of Geometry Parameters of Inkjet-Printed Silver Nanoparticle Traces on PDMS Substrates Using Response Surface Methodol-

ogy.” Mater. (Basel, Switzerland), 2019; 12(20); 3329.

- M. Khanfar, N. Abu Eisheh, L. Al-Ghussain, and A. Al-Halhouli. Lab on a Chip for the Colorimetric Determination of Nitrite in Processed Meat Products in the Jordanian Market. *Micromachines*, 2019, doi: 10.3390/mi10010036.
- J. Abu-Khalaf, L. Al-Ghussain, and A. Al-Halhouli. Fabrication of Stretchable Circuits on Polydimethylsiloxane (PDMS) Pre-Stretched Substrates by Inkjet Printing Silver Nanoparticles. *Materials (Basel)*., vol. 11, no. 12, p. 2377, 2018, doi: 10.3390/ma11122377.
- L. Al-Ghussain, H. Ahmed, and F. Haneef. Optimization of hybrid PV-wind system: Case study Al-Tafilah cement factory, Jordan. *Sustain. Energy Technol. Assessments*, vol. 30, pp. 24–36, Dec. 2018, doi: 10.1016/j.seta.2018.08.008.
- L. Al-Ghussain, O. Taylan, D. K. Baker, L. Al-Ghussain, O. Taylan, and D. K. Baker. An investigation of optimum PV and wind energy system capacities for alternate short and long-term energy storage sizing methodologies. *Int. J. Energy Res.*, vol. 43, no. April, pp. 1–15, 2019, doi: 10.1002/er.4251.
- L. Al-Ghussain and O. Taylan. Sizing methodology of a PV/wind hybrid system: Case study in cyprus. *Environ. Prog. Sustain. Energy*, vol. 38, no. 3, p. e13052, May 2019, doi: 10.1002/ep.13052.
- L. Al-Ghussain. Global warming: review on driving forces and mitigation. *Environ. Prog. Sustain. Energy*, vol. 38, no. 1, pp. 13–21, Jan. 2018, doi: 10.1002/ep.13041.
- L. Al-Ghussain, O. Taylan, and M. Fahrioglu. Sizing of a PV-wind-oil shale hybrid system: Case analysis in Jordan. *J. Sol. Energy Eng. Incl. Wind Energy Build. Energy Conserv.*, 2017, doi: 10.1115/1.4038048.